

**PDE-CONSTRAINED OPTIMIZATION ALGORITHMS
FOR INVERSE PROBLEMS
IN BIOMECHANICS AND MECHANOBIOLOGY**

By

Li Dong

A Dissertation Submitted to the Graduate
Faculty of Rensselaer Polytechnic Institute

in Partial Fulfillment of the
Requirements for the Degree of
DOCTOR OF PHILOSOPHY

Major Subject: **MECHANICAL ENGINEERING**

Examining Committee:

Assad A. Oberai, Dissertation Adviser

Onkar Sahni, Member

Jason E. Hicken, Member

Xavier Intes, Member

Rensselaer Polytechnic Institute
Troy, New York

July 2017
(For Graduation August 2017)

© Copyright 2017
by
Li Dong
All Rights Reserved

CONTENTS

LIST OF FIGURES	vi
ACKNOWLEDGMENT	xi
ABSTRACT	xiv
1. Introduction	1
1.1 Biomechanics and mechanobiology	1
1.2 Biomechanical imaging	2
1.2.1 BMI with surface measurement	2
1.2.2 BMI with full interior measurement	3
1.2.2.1 Qualitative BMI - strain imaging	3
1.2.2.2 Quantitative BMI	4
1.3 Cell traction force microscopy	8
1.3.1 Experimental techniques	9
1.3.2 Computational algorithms	10
1.4 Organization of this thesis	11
2. Quantitative Compression Optical Coherence Elastography as an Inverse Elasticity Problem	13
2.1 Introduction	13
2.2 Background	15
2.2.1 Quantitative elasticity imaging	15
2.2.2 Assumed model of tissue mechanical properties	16
2.2.3 First-order solutions to the inverse elasticity problem	16
2.2.4 Direct, general solutions of the inverse elasticity problem	19
2.2.5 Iterative, general solutions of the elasticity inverse problem	19
2.3 Methods	20
2.3.1 Computational method	20
2.3.2 Experimental setup	24
2.4 Results	25
2.5 Discussion	31
2.6 Conclusion	35

3.	Inverse Methods for 3D Quantitative Optical Coherence Elastography	36
3.1	Introduction	36
3.2	Results	37
3.2.1	Mechanical imaging of heterogeneous tissue-mimicking phantoms	37
3.2.1.1	Phantom with multiple inclusions	37
3.2.1.2	Phantoms with single inclusion	39
3.2.2	<i>Ex-vivo</i> mechanical imaging of malignant breast tumor	40
3.2.3	<i>In-vivo</i> mechanical imaging of skin	41
3.3	Discussion	43
3.4	Methods	45
3.4.1	Construction and characterization of phantom	45
3.4.2	Preparation of breast tumor sample	45
3.4.3	Preparation of skin sample	46
3.4.4	OCE system and displacement estimation	47
3.4.5	Inverse problem solution	47
4.	Recovery of Cellular Traction in Three-Dimensional Nonlinear Hyperelastic Matrices	57
4.1	Introduction	57
4.2	The forward elasticity problem	60
4.2.1	Strong form	61
4.2.2	Weak form	62
4.3	Inverse problem for the traction vector field	64
4.3.1	Inverse problem statement	64
4.3.2	Formulation of the gradient	66
4.4	Numerical examples	68
4.4.1	Microglial cell model	69
4.4.2	Neuronal cell model	74
4.4.3	Discussion	80
4.5	Applications to experimental data	83
4.5.1	Demonstration of feasibility with linear elasticity	83
4.5.2	Illustration of challenges in nonlinear elasticity	84
4.6	Summary	87

5. Conclusions and Future Work	88
5.1 Conclusions	88
5.2 Future work	89
REFERENCES	92

LIST OF FIGURES

2.1	Flow diagram of the inverse problem solver (shaded blue) and how it interacts with the experimental system (shaded in orange). Computation concludes when the discrepancy between the predicted and measured displacement fields falls below a prescribed tolerance (denoted tol).	23
2.2	Tissue-simulating silicone phantom. (a) OCT image in dB, (b) local displacement from micro-scale actuation, (c) axial strain, where $m\varepsilon$ is milli-strain, and (d) shear modulus image, reconstructed by solving the elasticity inverse problem. The scale bar represents 500 μm . Red dashed lines represent the layer-tissue boundary.	25
2.3	(a) Displacement matching term with respect to the regularization parameter in the inclusion phantom; red star marker shows the selected optimal regularization parameter used in Fig. 2.2(d). Shear modulus images evaluated with regularization parameters labeled by black plus markers are shown in (b) as under-regularized, and (c) over-regularized. Red dashed lines represent the layer-tissue boundary.	26
2.4	Convergence of the phantom solution with optimal regularization parameter.	27
2.5	Transverse section of an equine bronchus. (a) OCT image in dB. M: mucosa, ASM: airway smooth muscle, and C: cartilage; (b) local displacement from micro-scale actuation; (c) axial strain, where $m\varepsilon$ is milli-strain; and (d) shear modulus image, reconstructed by solving the elasticity inverse problem. The scale bar represents 500 μm . Red dashed lines represent the layer-tissue boundary.	27
2.6	(a) Displacement matching term with respect to the regularization parameter in tissue; red star marker shows the selected optimal regularization parameter used in Fig. 2.5(d). Shear modulus images evaluated with regularization parameters labeled by black plus markers are shown in (b) as under-regularized, and (c) over-regularized. Red dashed lines represent the layer-tissue boundary.	28

3.1	OCE of tissue-mimicking phantom with multiple inclusions. (a) Average shear modulus and its variance for the experimental test, the algebraic method, and the iterative method. <i>En-face</i> (b), B-scan (d), and segmented (c) images from OCT data. <i>En-face</i> (e), and B-scan (h) images of strain data. <i>En-face</i> (f), B-scan (i), and segmented (g) images of shear modulus from algebraic inversion. <i>En-face</i> (j), and B-scan (m) images of the mesh generated during iterative inversion. <i>En-face</i> (k), B-scan (n), and segmented (l) shear modulus images from iterative inversion.	40
3.2	OCE of tissue-mimicking phantom with single inclusion. (a) Average shear modulus and its variance for the experimental test, the algebraic method, and the iterative method. <i>En-face</i> (b), B-scan (d), and segmented (c) images from OCT data. <i>En-face</i> (e), and B-scan (h) images of strain data. <i>En-face</i> (f), B-scan (i), and segmented (g) images of shear modulus from algebraic inversion. <i>En-face</i> (j), and B-scan (m) images of the mesh generated during iterative inversion. <i>En-face</i> (k), B-scan (n), and segmented (l) shear modulus images from iterative inversion.	51
3.3	OCE of tissue-mimicking phantom with star inclusion. (a) Average shear modulus and its variance for the experimental test, the algebraic method, and the iterative method. <i>En-face</i> (b), B-scan (d), and segmented (c) images from OCT data. <i>En-face</i> (e), and B-scan (h) images of strain data. <i>En-face</i> (f), B-scan (i), and segmented (g) images of shear modulus from algebraic inversion. <i>En-face</i> (j), and B-scan (m) images of the mesh generated during iterative inversion. <i>En-face</i> (k), B-scan (n), and segmented (l) shear modulus images from iterative inversion.	52
3.4	<i>Ex vivo</i> OCE of a malignant breast tumor. (a) H&E histology. B-scan (b) and (d), and <i>en-face</i> (c) images from OCT data. B-scan (e) and (h), and <i>en-face</i> (g) images of strain data. B-scan (f) and (j), <i>en-face</i> (i), and segmented (k) images of shear modulus from algebraic inversion. B-scan (l) and (o), and <i>en-face</i> (n) images of the mesh generated during iterative inversion. B-scan (m) and (q), <i>en-face</i> (p), and segmented (r) images of shear modulus from iterative inversion. A = adipose, S = stroma, T = tumor, CL = calibration layer.	53

3.5	<i>In vivo</i> OCE of fingertip tissue. <i>En-face</i> (a), and B-scan (b), (c), (o) and (p) images from OCT data. <i>En-face</i> (d), and B-scan (e) and (f) images of strain data. <i>En-face</i> (g), B-scan (h) and (i), and segmented (j) images of shear modulus from algebraic inversion. <i>En-face</i> (k), B-scan (l) and (m), and segmented (n) images of shear modulus from iterative inversion. SC = stratum corneum, E = epidermis, D = dermis, SG = sweat gland.	54
3.6	Illustration of adaptive mesh refinement. First column (a,c,e,g) displays the adaptive grids in the B-scan view in different adaptive stages. Second column (b,d,f,h) displays the segmented shapes of the inclusion in different stages.	55
3.7	Illustration of domain decomposition. (a) and (b), (c) and (d), (e) and (f) are the three subproblems. (g) and (h) are the composite solution. (a), (c), (e) and (g) are the B-scan planes of (b), (d), (f) and (h) on the black dashed lines, respectively. Orange boxes indicate the regions with refined mesh.	56
4.1	L-curve for the microglial cell model with nonlinear effects and 1% noise. 69	
4.2	Microglial cell: (a) Mesh on the exterior surface and the cell-matrix interface. Results of the simulated forward problem on the deformed surface with $\gamma = 1$. (b) Arrows display the traction field (in kPa), and the deformed surface is colored by the displacement magnitude in μm . (c) The first principal component of the Green-Lagrange strain tensor. (d) Distribution of the strain at the bead locations as a function of distance from the center.	70
4.3	Results of the inverse analysis for the microglial cell on the deformed surface with $\gamma = 1$. Arrows display the recovered traction field (in kPa), and the deformed surface is colored by the recovered displacement magnitude in μm . (a) Solution with nonlinear effects and 0% noise. (b) Solution with nonlinear effects and 1% noise. (c) Solution without nonlinear effects and 0% noise. (d) Solution without nonlinear effects and 1% noise.	73
4.4	Error summary for the microglial cell model.	74
4.5	Results of the simulated forward problem for the microglial cell model on the deformed surface with $\gamma = 5$. (a) Arrows display the traction field (in kPa), and the deformed surface is colored by the displacement magnitude in μm . (b) The first principal component of the Green-Lagrange strain tensor. (c) Distribution of the strain at the bead locations as a function of distance from the center.	75

4.6	Results of the inverse analysis for the microglial cell on the deformed surface with $\gamma = 5$. Arrows display the recovered traction field (in kPa), and the deformed surface is colored by the recovered displacement magnitude in μm . (a) Solution with nonlinear effects and 0% noise. (b) Solution with nonlinear effects and 1% noise. (c) Solution without nonlinear effects and 0% noise. (d) Solution without nonlinear effects and 1% noise.	76
4.7	Neuronal cell: (a) Mesh on the exterior surface and the cell-matrix interface. Results of the simulated forward problem on the deformed surface with $\gamma = 1$. (b) Arrows display the traction field (in kPa), and the deformed surface is colored by the displacement magnitude in μm . (c) The first principal component of the Green-Lagrange strain tensor. (d) Distribution of the strain at the bead locations as a function of distance from the center.	77
4.8	Results of the inverse analysis for the neuronal cell on the deformed surface with $\gamma = 1$. Arrows display the recovered traction field (in kPa), and the deformed surface is colored by the recovered displacement magnitude in μm . (a) Solution with nonlinear effects and 0% noise. (b) Solution with nonlinear effects and 1% noise. (c) Solution without nonlinear effects and 0% noise. (d) Solution without nonlinear effects and 1% noise.	79
4.9	Error summary for the neuron cell model.	80
4.10	Results of the simulated forward problem for the neuronal cell model on the deformed surface with $\gamma = 5$. (a) Arrows display the traction field (in kPa), and the deformed surface is colored by the displacement magnitude in μm . (b) The first principal component of the Green-Lagrange strain tensor. (c) Distribution of the strain at the bead locations as a function of distance from the center.	81
4.11	Results of the inverse analysis for the neuronal cell on the deformed surface with $\gamma = 5$. Arrows display the recovered traction field (in kPa), and the deformed surface is colored by the recovered displacement magnitude in μm . (a) Solution with nonlinear effects and 0% noise. (b) Solution with nonlinear effects and 1% noise. (c) Solution without nonlinear effects and 0% noise. (d) Solution without nonlinear effects and 1% noise.	82

ACKNOWLEDGMENT

First and foremost, my sincere gratitude goes to my doctoral advisor, Professor Assad Oberai. Without his patience and guidance, I would not enjoy my study at RPI that much. I benefit a lot from his thinking process and his “Eureka” moments during discussion always excite me. After 4 years mentorship from him, I believe I have become the researcher I expect to be. I consider it a great fortune to be his doctoral student.

I thank my committee members, Professor Onkar Sahni, Professor Jason Hicken and Professor Xavier Intes, for their time serving in my doctoral committee. My Ph.D. student career is not complete without their advice and support.

I cannot finish this thesis without my advisor Assad Oberai’s valuable suggestions. Moreover, this thesis cannot appear as good as it is without his sentence-by-sentence proofreading. I also would like to thank the Office of Graduate Education, especially Susan Palmer, for their efforts going through my long references list line by line.

There are two professors in the Department of Mathematical Sciences at RPI I would also like to thank, Professor Rongjie Lai and Professor Peter Kramer. It is from these two professors that I learned to appreciate the beauty of mathematics in both applied and pure aspects. I especially want to thank Professor Rongjie Lai for having numerous discussions with me about Split Bregman method as well as for serving as my academic advisor in mathematics.

I thank our collaborators from University of Western Australia, Dr. Brendan Kennedy, Dr. Peter Munro, Dr. Philip Wijesinghe and Professor David Sampson, who provided us with well-calibrated experimental data and insightful suggestions that contribute to Chapter 2 and 3. I also thank Professor Christopher Chen and Dr. Colin Choi from Boston University, who shared excellent cell traction force microscopy data and keen opinions with us that contribute to 4.5.1.

I thank the previous Ph.D. student in our group, Mohit Tyagi, for his help in my research when I just joined the group. Collaborating with him on stochastic

course assignments become one of the most memorable moments of my study life at RPI. I also would like to thank my colleagues and friends, Chao Liu, Zhen Li, Tengxiao Liu, Victor Chan, Dhruv Patel, Nicholas Hugenberg, Yu Zhang, Fan Zhang and Brian Granzow, with whom I have countless discussions related to various topics.

My life at Troy would not be the same without my lovely friends, Zehai Wang, Zeyong Wang, Hao Wang and so on. I thank them for being helpful, supportive and available when I need them.

I thank my parents, Huijuan Liu and Bo Dong, for their unconditional and constant support and steadfast trust and confidence in me. My thanks also go to my grandmother Shuhua Wang, aunt Ling Dong and other family members who have always been there for me during my growing-up. I feel deeply sorry for not being able to be on your sides to share the sadness with you all when my grandfather Xianrong Dong and aunt Zhen Dong passed away in the past year. I thank both of them for making significant and positive impacts on my childhood.

Last but not the least, I thank my beloved wife, Yang Lu, for her unwavering belief in me and her tender and strong support in all aspects of my life.

To my wife and my parents.

ABSTRACT

Sitting at the interface of biology and engineering, biomechanics and mechanobiology are important areas where computational modeling is applied to study how mechanics and biological processes influence and regulate each other. In the continuum regime of biomechanics and mechanobiology, inverse problems often arise in applications such as biomechanical imaging (BMI) and cell traction force microscopy (TFM). In BMI, typically the tissue properties, for instance, the shear modulus or the nonlinear elastic parameter, are reconstructed, given experimentally measured full interior displacement field. BMI is extensively studied in tissue mechanical property quantification. On the other hand, in cell TFM, the traction on a cell's surface is recovered, given experimentally measured displacement field in the extracellular matrix, where dense tracking beads are embedded. Cell traction is crucial in understanding stem cell differentiation, cancer cell metastasis, embryonic morphogenesis, etc. For both BMI and TFM, the displacement field is obtained from various imaging modalities, such as magnetic resonance (MR), ultrasound, optical coherence tomography (OCT), confocal laser scanning microscopy (CLSM) and stimulated emission depletion (STED) microscopy, where the resolution ranges from millimeters to nanometers.

Both problems described above are governed by the same system of elliptic PDEs that enforce mechanical equilibrium for an elastic material. In this thesis, we apply an optimization framework and treat the above two types of inverse problems as PDE-constrained optimization problems and solve them with one general algorithmic framework. In the language of PDE-constrained optimization problems BMI leads to a parameter identification problem, and TFM leads to a source identification problem. For the parameter identification problem, we demonstrate the iterative reconstruction of shear modulus with displacement data from OCT. Moreover, we apply and demonstrate the utility of adaptive mesh refinement and domain decomposition in efficiently solving this problem. We validate these methods with tissue-mimicking phantoms and *ex-vivo* and *in-vivo* biological tissues in 2D and 3D.

For the source identification problem, we pose and implement a novel formulation that accounts for finite deformation and material nonlinearity in 3D. The algorithm is applied to *in-silico* problems and the error incurred in making the linear elastic assumption is quantified. It is also applied to determine the tractions exerted by live cells on their surroundings. All computations were performed using our in-house FORTRAN code, nonlinear adjoint coefficients estimator (NLACE) which is parallelized on shared-memory machines.

CHAPTER 1

Introduction

1.1 Biomechanics and mechanobiology

Biomechanics and mechanobiology are like the two sides of a coin. They delineate the intertwined relation between biological processes and mechanics. In biomechanics, biological processes can generate forces and regulate the mechanical properties of a system; in mechanobiology, applied load and varying system stiffness can in turn influence and regulate biological processes [1].

To be more specific, on the tissue level, the progression of several diseases, such as different types of cancers, fibrosis and sclerosis, is marked by significant changes in tissue micro-structure that lead to changes in mechanical properties. For example, the progression of breast and prostate cancer is accompanied by the evolution of stiff tumors [2]–[5]; fibrosis of liver is accompanied by a diffuse stiffening of tissue [6]–[8]; atherosclerosis is marked by significant stiffening in arterial walls [9]; Alzheimer’s disease is correlated with the softening of the brain parenchyma [10]. Due to these correlations, the ability to non-invasively quantify the spatial variation of mechanical properties is being used in the understanding, detection, diagnosis and therapeutic monitoring of diseases such as breast [3]–[5], [11], [12], prostate [12], [13], pancreatic [14], [15] and skin cancers [16], glioblastoma [17], Alzheimer’s disease [10], liver cirrhosis [6]–[8], atherosclerosis [9], vulnerable plaques [18], cardiac disease [19], muscular disorders [20], damage in trabecular bone [21] and corneal disease [22].

On the cellular level, cell-matrix adhesive interactions are known to regulate cells’ form, function and fate and drive tissue development and homeostasis. For all these cases, forces exerted by cells and mechanical properties of extracellular matrices are two foremost factors [23]–[28]. For example, cell-generated forces are crucial during tissue morphogenesis and embryogenesis [29]–[31]; in breast cancer lesions, activated fibroblasts recruit fibrillar constituents that promote the invasive phenotype and further enhance stiffness [32]–[34]. Thus the ability to control and monitor the spatial and temporal variation of cellular forces and mechanical prop-

erties of extracellular matrices can lead to a better understanding of the pathways that control these processes and pave the way for a tool with which to control them.

Biomechanical imaging (BMI) and cellular traction force microscopy (TFM) are two effective approaches to infer mechanical properties and cellular forces, respectively, from experimental observations and are the two foci of this thesis.

1.2 Biomechanical imaging

Biomechanical imaging (BMI), elasticity imaging or elastography refers to a collection of techniques to non-invasively quantify the mechanical properties of tissue-like soft materials [35]–[39]. It relies on imaging-based experimental techniques as well as robust computational algorithms. For BMI, experimental observation is mainly about measuring the deformation of specimens and sometimes the corresponding forces applied. There are many ways to categorize BMI methods. To name a few, they are categorized based on whether the load is applied externally or internally (cardiac motion, respiratory motion or pulsation), based on whether the load is applied in a transient, time-harmonic or quasi-static way, based on the measurement devices (mechanical, ultrasound, optical or magnetic resonance), and based on whether the results are qualitative or quantitative. Good reviews for this topic are published recently by Barbone and Oberai [39], Doyley [40] and Mariappan [41]. Apart from these perspectives, we can also classify BMI methods based on whether we have surface measurement only or full interior measurement.

1.2.1 BMI with surface measurement

In the case of surface measurement, surface indentation is typically applied and mechanical properties in the whole domain are inferred. Egorov *et al.* [42]–[44] reported promising results in breast cancer based on experimental data, where Young’s modulus were calculated given displacement and force measurement on surface; Mei *et al.* [45] and Olson and Throne [46] demonstrate solutions with multiple simulated surface deformation measurements. The inverse problem given only surface measurement is more ill-posed than the case with full interior measurement and it poses different challenges. Since there is much richer literature for the case with

full interior displacement measurement [35]–[39] and it is also one of the foci of this thesis, more discussion about BMI with surface measurement are beyond the scope of this thesis.

1.2.2 BMI with full interior measurement

In the case of full interior measurement, the deformation of a specimen under dynamic or quasi-static load is captured in a sequence of images with conventional imaging modalities, often ultrasound, optical coherence tomography (OCT) *etc.* Obtaining displacement from these images is not a trivial process, especially for ultrasound. Usually, researchers in ultrasound elastography tend to use minimization-based or cross-correlation-based motion estimation algorithms [47]–[52]; while phase-based methods are more widely adopted for the recently fast emerging field - OCT elastography [53], [54]. OCT imaging generally has higher resolution (micrometers) and poorer penetration depth (millimeters) compared to ultrasound imaging (tens of micrometers in resolution and tens of millimeters in penetration depth).

1.2.2.1 Qualitative BMI - strain imaging

Strain imaging is a dominant technique in elastography. In fact, before robust and efficient algorithms were implemented on powerful computers, strain imaging was the only technique in elastography. Nowadays it is still a dominant approach because it is easy to implement and the results are sufficiently interpretable clinically since strain is simply the derivative of the deformation and it can certainly provide some information related to modulus. There are several applications of strain imaging in ultrasound [12], [37], [48], [52], [55] and in OCT [56], [57]. Implementation-wise, since measured displacement can be noisy, appropriate filtering is mostly used, such as weighted least square [56], different types of regularization [49], PDE-constrained filtering [58] and Kalman filtering [52]. Despite of strain imaging's wide application, its lack of sufficiently quantitative information for mechanical properties is a drawback. Further, since strain depends on the applied deformation, which is itself operator-dependent, strain imaging also suffers from the drawback that it is operator-dependent.

1.2.2.2 Quantitative BMI

In order to obtain quantitative mechanical properties from displacement measurement, the stress-strain relation and the equations of equilibrium need to be considered. These equations are partial differential equations (PDEs), which makes solving the problem of determining the modulus very complex. In order to avoid this, several researchers have made approximations about the stress state. These simplified solutions are often termed as “first-order solutions” [40].

First-order solutions

The assumptions incurred in the first-order solution depend on whether the loading is dynamic or quasi-static.

If the load is applied on the specimen in a way that the inertia of the specimen cannot be ignored, the loading is dynamic. Within this it can be either transient if the specimen is excited by acoustic force, air puff or pulsed laser, or time-harmonic if the specimen is excited constantly at a certain fixed frequency. When considering first-order solutions in both transient (ultrasound[59], OCT[60]–[62], MRI[63]) and time-harmonic (ultrasound[64], OCT[65], MRI[66]) cases, it is assumed that the shear modulus is related to shear wave velocity by $c_s = \sqrt{\frac{\mu}{\rho}}$, where c_s is the shear wave velocity, μ is the shear modulus and ρ is the mass density. This relation assumes that the shear wave travels in a reflection-free medium, which is seldom the case. Once this is assumed, the wave speed is measured through some simple algorithm (wavefront tracking, time arrival, *etc.*) and is related to the shear modulus. Although remedy has been proposed to alleviate the limitation [40], it still appears challenging to use these approaches.

In some instances, the external load is applied very slowly in a quasi-static way where the inertia of the specimen can be safely ignored. First-order solutions to the quasi-static problem have been implemented for ultrasound [35] and MRI [67]. In most cases, this involves assuming a one-dimensional stress state along the axis of compression. Recently Kennedy *et al.* [68] have proposed a approach for OCT. They overlay a compliant layer with known material properties above the specimen during quasi-static compression. This supplies a 2D spatial stress map.

With the stress information and measured displacement, the shear modulus can be immediately retrieved by a simple algebraic inversion once it is assumed that the axial stress is constant along the axis of compression. Unlike strain imaging where the stress is considered homogeneous everywhere within the specimen, here the stress is only assumed uniform along the loading direction. This does not increase computation burden yet it provides more quantitative information. We note that even this assumption can very easily break in the presence of heterogeneities within the specimen [69].

Solutions to the inverse problem

In elasticity, a forward problem is to find the displacement given material properties and boundary conditions; an inverse problem is to find the material properties given measured displacement and some boundary data. This problem is ill-posed in the sense of Hadamard. In particular, while it is possible to show the existence and uniqueness of solutions (at least for the case with no noise in the measurements), it is quite difficult to show that the solution is continuously dependent on input data.

In almost all cases, the solution to the inverse problem is obtained by posing it as a constrained minimization problem. In the problem, the mismatch between the measured and the predicted displacement is minimized, where the predicted displacement field is required to satisfy the equations of equilibrium. The solution is obtained by seeking the spatial distribution of material properties that minimizes the difference between the predicted and the measured displacement field. Such PDE-constrained minimization problems are solved using a gradient-based algorithm, where the gradient is efficiently determined by solving a forward and an appropriately selected adjoint problem.

Solving the inverse problem in the transient case is very challenging since the forward problem needs to be solved forward in time, the adjoint problem needs to be solved backward in time and computing the gradient needs solutions from both problem at all time steps, which creates difficulties in memory management [70] and computational scaling [71]. Although the former difficulty can be alleviated by checkpoint algorithms [72], parallelizing the solver still remains challenging. In

the context of BMI or elastography, solving the transient elasticity problem has not been explored. Recently, there are some trials by Bayat *et al.* in this direction [73]. More broadly speaking, there are some interesting algorithms that tackle the transient elasticity problem in a slightly more general sense [74]–[76] as well as the rich resources in the area of seismic inversion [70], [77] where only surface measurement is available.

Solving the inverse problem in the time-harmonic case is relatively well explored [78]–[86]. In this case, the forward problem reduces to an elliptic PDE (no time dependence) and the adjoint problem also reduces to an elliptic PDE. Thus, the difficulties associated with solving a forward-in-time forward problem and the backward-in-time adjoint problem are circumvented.

Solving the inverse problem in the quasi-static case has been reported with ultrasound [87]–[92], MRI [93] and recently OCT [69] data. The quasi-static inverse elasticity problem can either be solved with direct methods [87], [88], [94], [95] or iterative methods [89], [90], [92], [96]–[98]. Direct methods converge fast yet can easily diverge when data is only mildly noisy, since derivatives are taken with respect to measured displacement field. In contrast, iterative methods are more robust to imperfect data yet converge relatively slowly. Generally, iterative methods are based on optimization formulation and gradient-based algorithms are mostly adopted. As noted earlier, computing the gradient can be very expensive. In this type of problems, the adjoint method is commonly used to decrease the computational cost. In the context of BMI, adjoint method is first proposed by Oberai *et al.* [98] and similar applications of adjoint method can be found in many areas, such as cell traction force microscopy [99], artificial neural networks [100], fluid control in computer graphics [101], error estimation for adaptive mesh refinement [102], recovering rheological parameters of mantle flow in earth science [103], shape or topology optimization [104]–[106], tumor growth modeling ?, *etc.* The adjoint-based method has been explored well in linear and nonlinear inverse elasticity problems [91], [98], [108]–[111] and validated many times with experimental data, such as studies on cell stiffness [112], tissue-mimicking phantoms [69], [91], [113], *ex vivo* tissues (horse airway in Chapter 2 and breast tumor in Chapter 3) and *in vivo* tissues (breast tumor

[11], [92], [114], [115] and fingertip in Chapter 3).

Adaptive resolution and domain decomposition

While the adjoint-based approach to solving the inverse problem is very efficient, it is also can become computationally expensive in three dimensions. For example, in 3D using OCT, it is common to sample displacement on a grid that is $300 \times 500 \times 500$. This leads to 75 million optimization parameters for the inverse problem, which leads to a large computational costs. In this dissertation, we present two distinct approaches to deal with these costs - adaptive mesh refinement and domain decomposition.

The adaptive mesh refinement technique is often used in many computational science engineering fields, such as in modeling cardiovascular system [116], [117], structure formation in universe in cosmology [118], plate tectnoics and mantle flow in earth science [119], atmospheric science [120], magnetically confined fusion plasma simulation [121]. Recently, some researchers have applied the adaptive mesh refinement technique to BMI [122]–[124]. Arnold *et al.* devise the adaptive scheme to decrease the cost function of the variational problem and apply it to some synthetic data [122], [123]; Goksel *et al.* adopt the adaptive scheme that penalizes strain magnitudes and optimal Delaunay triangulation and apply it to some synthetic data and two experimental cases. Both of their model problems are in 2D with a couple of hundreds nodes and little biological relevance is discussed. This thesis proposes the adaptive strategy based on the gradient of shear modulus for BMI and demonstrate it in 3D on several phantom data and *ex-vivo* and *in-vivo* biological tissues data imaged with OCT. Specifically, tetrahedral elements are refined where the gradients of shear modulus are greater than certain threshold and the refinement stops when it reaches the resolution of measured displacement. Solution continuation is also used along the process of mesh refinement.

The domain decomposition technique originates from H. A. Schwartz's seminal work in 1870, where he proved the existence of harmonic functions on irregular domains which are the union of overlapping subdomains. After that, domain decomposition methods based on iterative strategies have been continuously developed

due to its natural parallelism to solve large-scale problems. A good review about iterative domain decomposition is published by Chan and Mathew [125]. In BMI, Van Houten *et al.* demonstrate a similar idea as domain decomposition and term it “subzone technique”, where the global domain is decomposed to overlapping sub-domains. They apply the subzone technique to MR elastography for brain tissue and obtain satisfactory results [126]. This thesis proposes a different idea in domain decomposition for BMI. In this strategy, the entire domain is modeled in each subproblem. However, a very coarse discretization is used everywhere except in a small subdomain, which is the region of interest. Using this approach all the subproblems can be solved simultaneously, and no data needs to be shared among them. This also obviates the need to perform multiple iterations of the subproblems. Further, since no data is communicated, the approach is very easily parallelizable. We demonstrate the method with 3D *in-vivo* fingertip tissue data measured by OCT.

1.3 Cell traction force microscopy

Measuring cell-generated forces is a broad topic that has seen the development of many different types of experimental and computational techniques. Initially, these methods tended to be qualitative, such as the ones based on wrinkling membranes [127] or collagen contraction [128]. As experimental techniques have grown more advanced, cantilever-based methods become popular, where cantilevers with known material properties are micro-fabricated and used to measure the motility of cells, including tissue pillars [129]–[132] and micropillars made of PDMS [133]–[137]. These methods require sophisticated fabrication skills and mainly recover cell-generated forces in 2D.

As computation power has increased significantly in the past few decades, some methods based on advanced computational techniques have emerged, among which the most prominent ones are traction force microscopy (TFM) in 2D [138]–[141], 2.5D [142], [143] and 3D [144]. In both 2D and 2.5D TFM, cells are grown on 2D substrates. They differ from each other in whether the depth of the substrate is accounted for in evaluating the traction forces. In contrast to this, in 3D TFM, cells are embedded in 3D hydrogels. 3D methods become increasingly popular cellular

behaviors in three dimensions is very different from that in two dimensions, and in most cases more representative of the actual *in-vivo* micro-environment that the cell sees. In the following, we review some of the experimental and computational techniques in TFM. Good surveys of about cell-generated forces measurement can be found in the publications by Polacheck and Chen [145], Style *et al.* [146] and Iskratsch *et al.* [23].

1.3.1 Experimental techniques

In TFM, cells are grown in a substrate and thousands of fluorescent beads are embedded around the cells as markers. While the cells are growing, they exert forces on the substrate which is typically made from mechanically well-characterized hydrogels. Then the specimen is lysed with detergent, or some other chemicals, and the link at the interface of cells and the hydrogels is dissolved. The cleavage of this link causes the substrate to relax, especially in regions that are close to the cell. The beads undergo a motion due to this relaxation. The displacement of the beads, and hence the substrate, is determined by comparing the positions of the beads before and after lysing [144]. The displacement field is determined using correlation-based methods, where the displacement is found by computing the cross-correlation of two windows in two consecutive images/volume frames, such as Digital Image Correlation (DIC) in 2D [146], [147] and Digital Volume Correlation (DVC) in 3D [142], [143], [148], [149]. It may also be determined using particle tracking methods where it is found by tracking each bead in consecutive image / volume frames [144], [150]–[153]. We note that though confocal laser scanning microscopy (CLSM) is the most common modality used in TFM, more recently other modalities like OCT and stimulated emission depletion (STED) microscopy have been employed. Out of these, STED microscopy, with its superior resolution (nano-scale) over conventional CLSM (micron-scale), it can provide very high-resolution measurement.

Once the displacements are known, the traction can be inferred using the techniques described in the following sections. Mathematically, this problem is a boundary source inversion problem where one finds tractions on boundaries given the response in the interior.

1.3.2 Computational algorithms

The inverse problem for TFM is governed by the equations of equilibrium. it shares this feature in common with the inverse problem in BMI. However, in TFM the traction on the cell surface is to be found, given measured displacement and the mechanical properties of the surrounding hydrogel. The algorithms to solve this inverse problem can be classified as direct and iterative methods in general.

Direct methods

The direct methods in TFM can be readily implemented and applied to both 2D [142], [143], [148] and 3D [153], [154]. Recently, direct methods have also been applied to large substrate deformations [155]. In most direct methods, strains are obtained by differentiating measured displacement fields. Then, traction can be evaluated via $\tau = \sigma(\epsilon) \cdot n$, where Cauchy stress σ is a function of strain ϵ through known constitutive equation and n is the surface normal. Though this method is easy to implement, it relies heavily upon the quality of measured displacement. The solution can deteriorate if the measured displacement is not sufficiently close to the surface of the cell or the noise in the displacement field rises above a certain level. Basically, this approach involves differentiating displacement data to determine strain and stress, and then extrapolating the stress from within the substrate to the interface between the cell and the substrate. Both of the steps have the potential of introducing noise and errors. On the other hand, the iterative methods address these drawbacks at the expense of a higher yet manageable computational cost.

Iterative methods

Much like the iterative methods in BMI, iterative methods in TFM also employ the optimization framework, where the cost functional consists of a data matching term that measures the difference between measured displacement and the displacement predicted from the elasticity PDE. In each iteration, the elasticity PDE is evaluated and an optimization algorithm, such as L-BFGS [156], is used to update the optimization variables, i.e. the unknown traction field. In the area of TFM, this has been done in several publications [144], [150], [152], [157]. These researchers tend

to use Green's function technique, or sometimes Boussinesq solution [158], to solve the forward elasticity PDE in the iterative scheme. The Boussinesq-solution-based method can be further simplified in 2D by posing it in the Fourier space, which is often referred to as Fourier Transform Traction Cytometry (FTTC) [140]. As stated in the previous sections of BMI, gradient computation is typically very expensive in optimization and evaluating gradients directly with respect to each optimization variable can easily lead to significant overhead, which is a shortcoming of the above-mentioned iterative methods. This problem can be addressed by properly deriving the adjoint equations as described in this thesis.

Another significant contribution of this thesis is the application of the iterative 3D TFM algorithm to the regime of finite deformation. The strains in a typical matrix are in the range of 50% and can often exceed 100% [144], [159], [160], and yet most researchers to date have modeled the deformation of the substrate using a infinitesimal strain assumption [144], [150], [152], [157]. In this thesis, we forgo this simplification and derive and implement a finite deformation algorithm.

1.4 Organization of this thesis

This dissertation makes original contributions to the field of biomechanics and mechanobiology. It is mainly concerned with quantifying the mechanical environment in biological systems. It does so by developing and implement new algorithms for biomechanical imaging (BMI) and the 3D traction force microscopy (TFM). In Chapter 2, we apply our adjoint-based iterative algorithm to shear modulus reconstruction with displacement measured by OCT in 2D under plane strain and linear elasticity assumptions. In Chapter 3, we incorporate adaptive mesh refinement and domain decomposition strategies into our iterative scheme. We apply the resulting algorithms to phantoms and *ex-vivo* and *in-vivo* tissue samples. We also demonstrate the benefit of our approach over simpler first-order methods. In Chapter 4, we develop an adjoint-based iterative algorithm with finite deformation capability for the 3D cell TFM problem. The algorithm is validated *in silico* and errors when linear elasticity is inappropriately assumed in large deformation is quantified numerically. We also present initial results for experimental data acquired on human

umbilical vein endothelial cells (HUVECs) in stiff and soft substrates. We end the thesis in Chapter 5 with conclusions and future work.

CHAPTER 2

Quantitative Compression Optical Coherence Elastography as an Inverse Elasticity Problem

2.1 Introduction

It has been well established that the mechanical properties of soft tissues are inextricably linked to the form and function of disease pathologies [38], [161]–[163]. For instance, fibrosis in liver has been observed to increase its stiffness through increased production and decreased degradation of extracellular matrix constituents [164]. During metastasis, invasive cancer cells have been reported to reduce the stiffness of the surrounding extracellular matrix, aiding in their own migration through healthy tissues [165], [166], whilst developed tumors, such as ductal carcinoma and fibroadenoma of the breast, have been characterized to be up to 14 times stiffer than surrounding fatty tissue [167], [168].

Knowledge of the mechanical properties can provide fundamental insight into the state of disease [161], [165], [169]; indeed, the biomechanics approach to identifying and characterizing disease has been emerging in the recent literature [162]. Particularly, a family of imaging techniques, termed elastography, have been developed to spatially map the mechanical properties of tissue into images, termed *elastograms*, on different length scales [39], [170], [171]. Ultrasound (US) and magnetic resonance (MR) elastography have been developed for whole organ imaging, with resolutions of 100 μm and 1 mm [172], respectively, reaching commercial success by demonstrating significant improvement in disease diagnosis within a clinically relevant environment, primarily in characterizing breast cancer [5], [11] and liver fibrosis [173]. Over the past 15 years, optical coherence elastography (OCE), based on optical coherence tomography (OCT), has been following the precedent set by US and MR; however, on a finer length scale of tissue, with resolution down to 10 μm [53], [174]. OCE

Portions of this chapter previously appeared as: L. Dong, P. Wijesinghe, J. T. Dantuono, D. D. Sampson, P. R. T. Munro, B. F. Kennedy *et al.*, “Quantitative compression optical coherence elastography as an inverse elasticity problem,” *IEEE J. Sel. Top. Quantum Electron.*, vol. 22, no. 3, pp. 277–287, May–Jun. 2016.

has demonstrated potential in a wide range of applications, including breast cancer [57], [175], ophthalmology [62], [176], and cardiology [177]–[179].

US, MR and optical elastography, at their core, involve the measurement of local displacement in tissue, which is elicited by some form of mechanical stimulation. From the displacement, it is possible to obtain some measure parameterizing tissue’s mechanical behavior, such as local strain [56], [180], phase velocity [181], [182], creep [183], [184] or resonant vibration amplitude [177], [185]. Such measurements, however, depend intrinsically upon the experimental method and tissue geometry, and do not usually represent a one-to-one mapping of the tissue’s mechanical properties. Quantitative elastography uses some form of mathematical inversion, which we will describe in this paper, to retrieve quantitative elasticity images, *i.e.*, quantitative maps of a sample’s intrinsic mechanical properties, which should be largely independent from the tissue loading, geometry and boundary conditions .

This process of mathematical inversion entails solving an inverse problem. The solution of such inverse problems is the subject of a large body of work, which we briefly introduce here before considering it in more detail in Section 2.2.1. There are broadly two principal ways in which the inverse elasticity problem can be solved: direct and iterative. The direct approach can be employed using so-called first-order approximations such as simplified models of tissue, limiting the accuracy of recovered elastic moduli [53]. When such first-order approximations are not made, direct approaches perform poorly when the measured data is incomplete or noisy [40]. Iterative approaches have been studied extensively in US and MR elastography [40]; however, few have implemented them for OCE [186], [187]. Iterative methods allow for the inverse elasticity problem to be solved within a more general framework, requiring fewer assumptions, at the cost of higher computational complexity.

In this paper, we apply an iterative approach, using an adjoint method [98] to solve the inverse elasticity problem in compression OCE, reconstructing the shear modulus in a tissue-simulating phantom and airway tissue. Furthermore, the retrieved spatial distributions of shear modulus are made absolute by the use of a calibration layer of known stiffness. This is the first time that an iterative solution of the inverse elasticity problem has been applied in OCE using experimental, rather

than synthetic [186], [187] data. The iterative approach makes fewer assumptions about the nature of mechanical deformation than direct approaches, which will likely lead to an improvement in the accuracy of reconstructed elastic moduli, and may enable more accurate longitudinal, multi-site and inter-sample comparison.

2.2 Background

2.2.1 Quantitative elasticity imaging

Quantitative elasticity imaging refers to the measurement, or estimation, of local intrinsic mechanical properties of a sample. The extracted properties must be premised on a mathematical model assumed to describe the underlying mechanical interactions under study. The most general model of tissue mechanics would include, for example, viscoelasticity, poroelasticity, anisotropy, and a nonlinear relationship between stress and strain [188], [189]. It is usually necessary, and indeed reasonable, to neglect several, application specific properties in order to quantify one, or perhaps two, of the most significant tissue mechanical properties, the most common of which being the elastic moduli.

Quantitative elasticity imaging should disentangle, as far as is possible, the elastic properties of the sample from its aggregate mechanical behavior, which is obfuscated by the loading method, sample geometry and boundary conditions. If performed correctly, it means that quantitative elasticity images from different samples , acquired at different sites using different imaging systems, should be able to be compared quantitatively. Such techniques allow for the development of objective methods of assessing or diagnosing disease. They also support longitudinal studies by allowing measurements, taken over the course of a study, to be compared. Finally, quantitative elasticity imaging also reduces, or eliminates, artifacts introduced by instrument operators.

There is a substantial body of prior work on the subject of quantitative elasticity imaging, spanning imaging modalities such as US, MR and optical. Within each modality, a variety of physical models are employed to link applied load and measured displacement to elasticity parameters. Furthermore, within a particular modality and mechanical model, a variety of methods exist for solving the inverse

elasticity problem, *i.e.*, the retrieval of elasticity parameters from the measured displacement. Good reviews of this subject were published recently by Barbone and Oberai [39] and Doyley [40], to which we direct the reader for a comprehensive treatment of this subject. We summarise here the state of the art in order to provide the context for the current work.

2.2.2 Assumed model of tissue mechanical properties

Quantitative elasticity imaging methods are differentiated by the particular model of tissue mechanics upon which they are based. Assuming, as we do in this case, incompressible, linear elastic, isotropic tissue, one starts with the most general model, composed of the time varying equation of equilibrium and constitutive relation. This assumption means that instead of having potentially 21 independent elasticity parameters, we are left with only one [40], with Young's modulus, E , being related to shear modulus, μ , as $E = 3\mu$. The principal models of tissue mechanics then differ according to how the equation of equilibrium's temporal dependence is treated. The three prevailing approaches are: quasi-static (as employed in this paper), harmonic and transient, in accordance with the principal ways in which all partial differential equations with a temporal dependence can be analysed. Equations (2.2)-(2.4), upon which our method is based, can be derived from the aforementioned general equations by assuming a quasi-static loading.

2.2.3 First-order solutions to the inverse elasticity problem

One approach to performing quantitative elasticity imaging is to implement simplified mechanical models which are readily invertible, either algebraically or numerically. These methods are often termed as first-order approximations [40] as they allow for measured displacements to be linearly related to elastic moduli. These models simplify the estimation of elastic moduli but with the penalty of using a potentially unrealistic model, which limits the accuracy of estimated elastic moduli in mechanically heterogeneous tissues possessing complex boundary conditions. A first-order approach to quasi-static elastography has been employed by researchers using US [35], MR [67] and OCT [68]. Under this approximation, the stress throughout a sample is assumed to be approximately constant. The strain throughout the

sample, estimated from the measured displacement field, may, thus, be used directly in combination with Hooke's law to obtain Young's modulus. This approach works well in small tissue samples possessing only weak variations in Young's modulus [190], yet will likely break down in general, heterogeneous cases.

First-order approximations have also been applied to harmonic elastography in US [64], MR [66] and OCT [65]. One way in which a first-order modulus retrieval can be performed is to note that plane-wavefront shear waves propagate in homogeneous media with a velocity given by [38]:

$$c_s = \sqrt{\frac{\mu}{\rho}}, \quad (2.1)$$

where μ is the shear modulus and ρ is the mass density. Thus, under the assumption of plane shear propagation, which applies in a homogeneous region, shear modulus can be accurately extracted from measured values of shear wave velocity. This approach clearly breaks down in the presence of mechanical inhomogeneities and requires *a priori* knowledge of tissue density. Whilst not all harmonic techniques are based on this shear wave relationship, in general, they all rely on some approximation based on homogeneous wave propagation or resonance, which limits their generality.

Transient first-order models have also been applied in US [59] and MR [63] elastography. These methods were introduced to overcome the limited depth penetration of shear waves. Transient elastography uses an ultrasound transducer to remotely generate shear waves within tissue. This approach to quantitative elasticity imaging is considered a first-order approximation as it also uses (2.1) to relate shear wave velocity to shear modulus, and in so doing assumes that the shear wave travels in a reflection-free medium. Although schemes have been proposed to overcome this limitation [40], using such approaches for quantitative elasticity imaging in heterogeneous tissue still appears challenging.

First-order methods have also been applied in the field of optical elastography, including in optical coherence elastography (OCE). Such a method has recently been applied in quasi-static OCE by assuming that stress remains constant throughout a sample [68]. It has been used in a transient mode, where surface acoustic waves are generated using an air-puff [60] and a pulsed laser [61], [62]. The group velocity of

the resulting surface waves was measured using OCT [60],[62]. In another approach, low-coherence interferometry was used to measure the surface wave dispersion relationship [61]. In the former two cases [60],[62], Young's modulus is retrieved from the surface wave group velocity, assuming that the surface wave travels on the boundary of an infinite half-space. In the latter case [61], a depth-resolved estimate of Young's modulus is obtained by analysing the dispersion relationship of the surface wave's spectral components, by exploiting the fact that lower frequency surface waves penetrate deeper into tissue. First-order harmonic approaches which make use of surface wave phase velocity to make depth-dependent estimates of Young's modulus have also been demonstrated [181],[191]. The analytic relationship expressed in (2.1) has also been exploited within the context of harmonic optical coherence elastography to estimate Young's modulus within tissue from the phase velocity of shear waves [192]. Finally, we note that magnetomotively actuated optical coherence elastography can also be considered a harmonic first-order quantitative technique [193],[194]. In one example [194], tissue samples were assumed to be in the form of cylinders fixed to a base but otherwise free. An analytic model was then used to predict resonant modes of longitudinal vibration of the cylinders based upon the physical (including Young's modulus) properties of the sample. This allows a sample's Young's modulus to be extracted so long as there is sufficient information about the sample's length, radius, density and Poisson's ratio.

First-order methods have limited generality as a result of the approximations required to obtain a readily invertible relationship between measured displacement and retrieved elasticity modulus. For example, common amongst the previously discussed approaches, are approximations such as assuming mechanical homogeneity or constant stress. A different approach to solving the inverse elasticity problem is required if these, and other, assumptions are not to be made. Beyond first-order approaches, and for each temporal flavor of elastography as stated, there are two principal ways of solving the inverse elasticity problem: direct and iterative.

2.2.4 Direct, general solutions of the inverse elasticity problem

Direct methods of solving the elasticity inverse problem begin with a mathematical statement of the direct elasticity problem and transform this into a problem that may be solved directly for the tissue mechanical properties. One example of a direct approach using quasi-static elastography derives a set of coupled partial differential equations, which may be solved to yield the shear modulus and hydrostatic pressure within tissue [94]. Although direct approaches have been proposed for harmonic and transient approaches to elastography, we will focus on quasi-static methods since this is the focus of this paper, and the limitations of direct methods are common to all methods.

Although considerable work has been done on the use of direct inversion methods [94], [95], [195], [196], they are not dominant, in general as a result of some weaknesses. The primary weakness is that these methods require accurate measurements of all components of the displacement field within the entire imaging plane. For example, in US elastography, accurate displacement measurements in any direction perpendicular to the direction of propagation of sound, are unfeasible. This limits the application of these methods.

2.2.5 Iterative, general solutions of the elasticity inverse problem

An alternative to direct solution of the inverse elasticity problem is iterative solution. This approach allows solutions to be obtained which rely on, potentially, very few assumptions and approximations. Prior information, such as the expected range of values of shear modulus, can be integrated into the solution method. There is a considerable body of work on iterative solution methods to inverse problems, which provides tools that can be applied to the particular application of quantitative elasticity imaging [197]. Each iterative solution method is based upon a robust and realistic forward model, *i.e.*, one which predicts displacements based upon given mechanical properties and applied load. The solution method iterates through candidate distributions of mechanical properties, ceasing when a satisfactory match has been reached between predicted and measured displacements as determined by an objective function such as (2.5), below. The main way in which iterative methods

differ from one another is by how the estimate for mechanical properties is refined at each iteration.

Finally, we note that iterative solutions to the OCE inverse problem have previously been proposed [186], [187]. In the first paper [187] to appear, the method of Kallel and Bertrand [198], the approximated Hessian iterative method, was employed. The paper presents results employing only synthetic data. The second paper to appear [186] differs significantly from the first, most likely due to the high computational overhead of requiring to calculate the Jacobian at each iteration. In this second work, the sample is segmented into a small number of (say up to four) regions with each region having a constant Young's modulus. The second difference is that the inverse problem is solved using a genetic algorithm, which would be a very computationally demanding approach for general problems such as that considered in this paper.

A classical approach to iteratively finding a solution which minimizes a functional such as (2.5) is to calculate the gradient vector and the Hessian matrix of (2.5) with respect to the spatially resolved elastic moduli, the unknowns of the inverse problem. Naïve approaches to calculating these quantities result in an inversion method that is computationally demanding. More advanced implementations [89], [187], [198] approximate the Hessian and evaluate the gradient in a significantly more efficient manner, which nonetheless increases in cost with the number of unknowns possessed by the inverse problem. An alternative method, which calculates the Jacobian of (2.5) by the solution of two direct problems, is known as the adjoint method [98], which results in a significant reduction in computational complexity, thus, making three-dimensional inverse problems tractable. It is this method which is employed in this paper.

2.3 Methods

2.3.1 Computational method

Optical coherence elastography, as considered here, yields spatially resolved measurements of tissue displacement which result from the quasi-static compression loading of tissue. Displacement fields are obtained using phase-sensitive OCT [199]

and are typically measured on a plane or within a volume, which we denote Ω in both cases. We express the measured displacement, mathematically, at location $\mathbf{x} \in \Omega$ as $\tilde{\mathbf{u}}(\mathbf{x})$. We note, however, that in general, only displacement components parallel to the OCT system's optical axis are measured, meaning that only one component of $\tilde{\mathbf{u}}(\mathbf{x})$, $\tilde{u}_{x_3}(\mathbf{x})$, is actually measured.

The time scale of the applied deformation is chosen such that the tissue inertia does not play a role in its mechanical response. As a result, the equations of equilibrium reduce to

$$\nabla \cdot \boldsymbol{\sigma} = \mathbf{0}, \quad \text{in } \Omega, \quad (2.2)$$

where $\boldsymbol{\sigma}$ is the Cauchy stress tensor and Ω represents the domain of the material. We model the material as an incompressible, isotropic solid, and assume a linear relation between stress and strain, which is reasonable since the applied strains are small. Under these assumptions, the stress-strain relation is given by

$$\boldsymbol{\sigma} = -p\mathbf{I} + 2\mu\boldsymbol{\epsilon}, \quad (2.3)$$

where p is the pressure, \mathbf{I} is the identity tensor, $\boldsymbol{\epsilon} = \frac{1}{2}(\nabla\mathbf{u} + \nabla\mathbf{u}^T)$ is the strain tensor, \mathbf{u} is the displacement vector, and μ is the shear modulus. The constraint of incompressibility implies that

$$\text{trace}(\boldsymbol{\epsilon}) = 0. \quad (2.4)$$

The forward elasticity problem may be stated as: given the shear modulus distribution in the domain Ω , and displacement/traction boundary conditions on the boundary $\partial\Omega$, determine the displacement field and the pressure field, such that (2.2) and (2.4) are satisfied.

In the corresponding inverse problem, the displacement is known (measured), and the elastic parameter is sought. In particular, the inverse problem may be stated as: given the displacement field in Ω , and displacement/traction boundary conditions on the boundary $\partial\Omega$, determine the shear modulus such that (2.2) and (2.4) are satisfied. Note that the pressure field is neither measured, nor is it explicitly sought. The pressure can be determined rather simply from (2.3) once the shear modulus is known.

When displacement data is available on a plane (as opposed to in a volume), a modeling choice has to be made. When the sample is relatively free to strain in the out-of-plane direction, it is conjectured that the stress components in this direction are small, and a state of plane-stress is assumed. On the other hand, when the sample is confined in the out-of-plane direction (due to boundary conditions, for example), it is conjectured that the strain in this direction is small, and a state of plane-strain is assumed. In this paper, due to boundary conditions at the top and bottom of the sample, the plane-strain assumption is made.

The solution to the inverse elasticity problem in three spatial dimensions, and in two dimensions in the plane strain configuration, is non-unique. In particular, there is an infinite set of solutions for μ that are consistent with the measured displacement field and equations (2.2) and (2.4). Prescribing traction data on the boundaries is equivalent to prescribing the shear modulus/pressure, and therefore, the existence of traction boundary conditions tends to reduce the solution set size of the inverse problem. For a detailed discussion of these topics, the reader is referred to [200]–[202].

The inverse problem is posed and solved as a constrained minimization problem. In particular, we seek the shear modulus distribution that minimizes the functional

$$\pi = \frac{1}{2} \int_{\Omega} |\mathbf{T}(\mathbf{u} - \tilde{\mathbf{u}})|^2 d\mathbf{x} + \alpha \int_{\Omega} \sqrt{|\nabla \mu|^2 + c^2} d\mathbf{x}, \quad (2.5)$$

where the predicted displacement field, \mathbf{u} , is constrained to satisfy (2.2) and (2.4), and the prescribed boundary conditions. Further, \mathbf{T} is a tensor whose values are used to weight displacement components according to their known or expected accuracy, α is a regularization parameter ($c \leq |\nabla \mu|$) that ensures the regularization term, which is a smoothed version of a total variation (TV) diminishing regularization [203], is a smooth function of μ . In the examples considered in this manuscript, $c = 0.01$. Further, it has been verified that in the regions where μ varies substantially, $c \ll |\nabla \mu|$, and that the smoothed version of the TV term closely approximates the TV term. The first integral in (2.5) measures the mismatch between measured and predicted displacement, and is referred to as the displacement mismatch term. The second term is the regularization term added

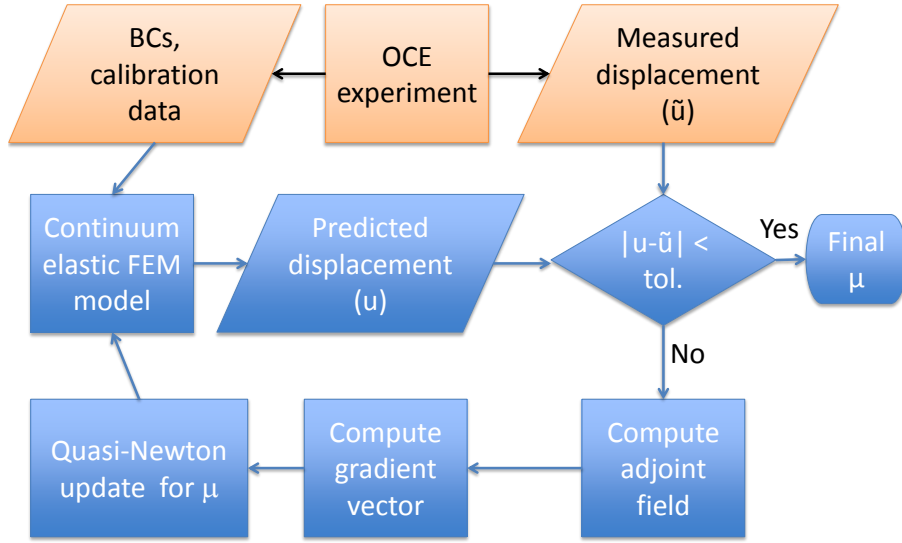


Figure 2.1: Flow diagram of the inverse problem solver (shaded blue) and how it interacts with the experimental system (shaded in orange). Computation concludes when the discrepancy between the predicted and measured displacement fields falls below a prescribed tolerance (denoted tol.).

to account for the ill-posed nature of the inverse problem, *i.e.*, small noise in the measured displacements leads to large, unphysical variations in the shear modulus distribution. These oscillations are suppressed by a large value of the regularization parameter which ensures smaller total variation in the recovered modulus distribution. It is worth noting that it does so at the expense of increasing the displacement matching term.

The problem of minimizing π reduces to a discrete optimization problem with nonlinear constraints once all the field variables are represented using finite element basis functions, and the constraint equations are discretized using the finite element method. The optimization parameters are the nodal values of the shear modulus field. This problem is solved using a quasi-Newton method, as depicted in Fig. 2.1, that builds the Hessian information by repeatedly evaluating the gradient of π with respect to the optimization parameters [204]. A straightforward evaluation of this gradient requires as many solves of the forward elasticity problem as the number of parameters, which can be very large ($O(10^4)$ for our problems). A much more efficient approach is to derive and solve the adjoint equations for the adjoint field,

and use the adjoint and the predicted displacement fields to evaluate the gradient vector [98], [109]. Within this approach, the gradient of π with respect to μ can be evaluated by solving a single forward and a single adjoint problem (which is of the same complexity as the forward problem) *independent of the number of parameters used to represent the shear modulus*. Considering that this number is $O(10^4)$, this is a significant, and necessary, computational saving.

2.3.2 Experimental setup

A fiber-based Fourier-domain OCT system was employed to perform OCE. The imaging system is described in detail in [57], and briefly here. The system was set up in a common-path configuration, such that the reference signal is provided by the reflection from the interface of a 2-mm glass window and a sample situated upon it. A superluminescent diode source with a central wavelength of 835 nm and a bandwidth of 50 nm was used to illuminate the sample with ~ 7.5 mW of power. The sensitivity was measured as 102 dB for an exposure time of 36 μ s, and an exposure time of 2–3 μ s was used in general. The system provides axial and lateral resolutions of 6.1 and 11 μ m, respectively, assuming a sample refractive index of 1.4 [205]. This refractive index was also used, throughout this paper, to scale the axial coordinates of the measured OCT intensities and displacements to closer match their true locations.

Compression OCE was performed by placing a sample on top of a 600- μ m thick compliant poly-dimethylsiloxane (PDMS) silicone layer of known stiffness, which was used to constrain the solution set of the inverse problem, hereby referred to as the calibration layer. Fabrication of the layer is described in detail in [205]. The sample-silicone assembly was situated between a rigid plate and a glass window coupled to a piezoelectric ring actuator [56], such that the OCT beam would pass through the window, then the silicone, and finally into the sample. To ensure even contact, the rigid plate was used to apply 5–10% preload strain. Following the preload, the piezoelectric actuator was used to apply step-wise micro-scale compression to the sample-silicone assembly, and two-dimensional images were captured sequentially, in the uncompressed and compressed (relative to the preload) states. The actua-

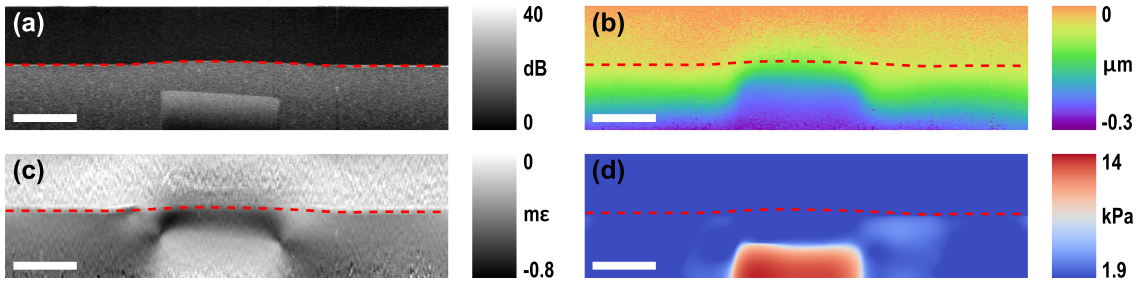


Figure 2.2: Tissue-simulating silicone phantom. (a) OCT image in dB, (b) local displacement from micro-scale actuation, (c) axial strain, where $m\epsilon$ is milli-strain, and (d) shear modulus image, reconstructed by solving the elasticity inverse problem. The scale bar represents 500 μm . Red dashed lines represent the layer-tissue boundary.

tor stroke was set between 1 and 2 μm , to ensure a high displacement and strain sensitivity [206]. The maximum attainable displacement and strain sensitivity was measured previously as 0.34 nm and 2.6 $\mu\epsilon$ ($\mu\epsilon$ is microstrain, strain $\times 10^{-6}$), respectively [57]. Actuation frequency was set below 25 Hz, which was experimentally verified to avoid any detectable wave propagation. We employ phase-sensitive OCE, described in detail in [199], in which the axial component of the displacement field, resulting from the micro-scale compression, is obtained from the difference between the angles of the polar-form complex OCT scans, corresponding to the uncompressed and compressed tissue states. Using this approach, we can measure axial displacement within the range $\pm 2.2 \mu\text{m}$ [57].

2.4 Results

In this section, we demonstrate the solution of the inverse elasticity problem for two samples: a tissue-simulating silicone phantom and a transverse section of an equine bronchus. The silicone phantom incorporated a 830- μm wide, rectangular, stiff inclusion embedded approximately 300 μm below the surface of a softer homogeneous matrix, following the fabrication method described in detail in [205]. The inclusion and the matrix were experimentally characterized using a standard bulk compression test (Instron, Norwood, MA, USA) to possess a shear modulus of 9.3 and 1.9 kPa, respectively, for preload applied in the experiment. The calibration

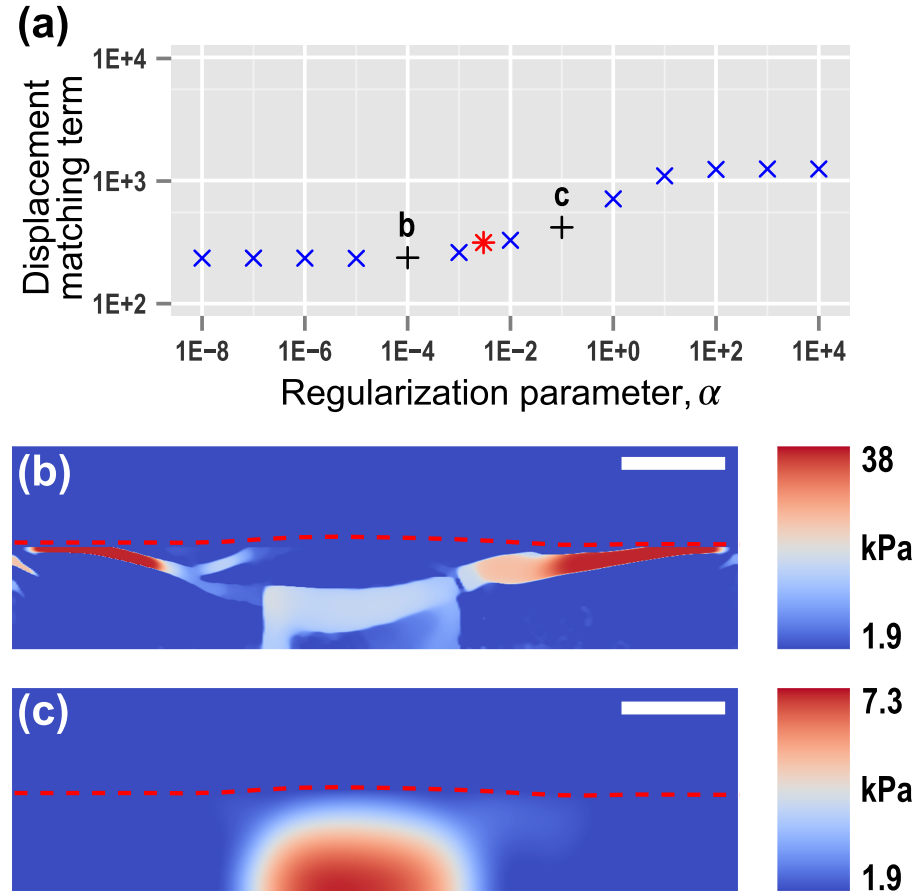


Figure 2.3: (a) Displacement matching term with respect to the regularization parameter in the inclusion phantom; red star marker shows the selected optimal regularization parameter used in Fig. 2.2(d). Shear modulus images evaluated with regularization parameters labeled by black plus markers are shown in (b) as under-regularized, and (c) over-regularized. Red dashed lines represent the layer-tissue boundary.

layer, described in Section 2.3.2, was also characterized to have a shear modulus of 1.9 kPa.

The OCT image of the already preloaded phantom is presented in Fig. 2.2(a), in which we can identify the calibration layer (black) and the inclusion embedded in a matrix. The displacement due to the micro-scale compression provided by the piezoelectric actuator is presented in Fig. 2.2(b). It is apparent how the feature distorts the otherwise uniform displacement field gradient: the result of the contrast in stiffness between it and the matrix. Fig. 2.2(c) shows an image of the axial strain,

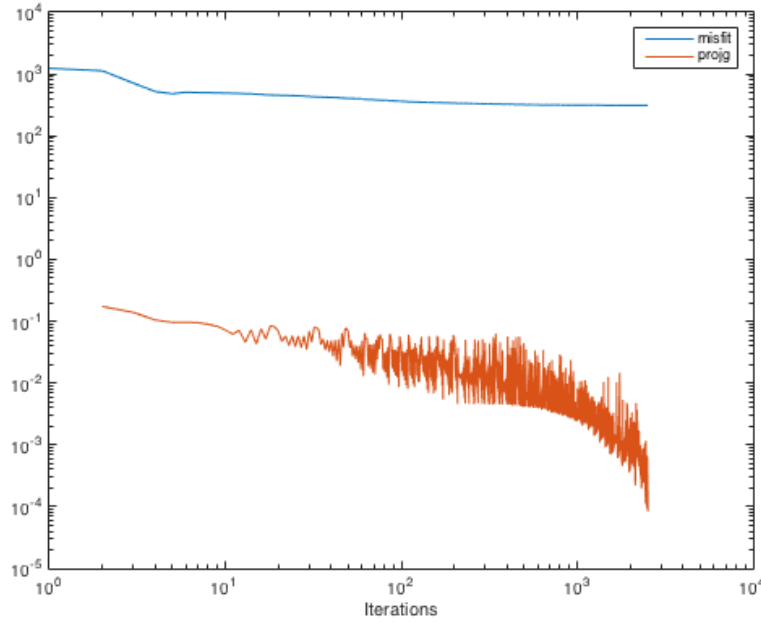


Figure 2.4: Convergence of the phantom solution with optimal regularization parameter.

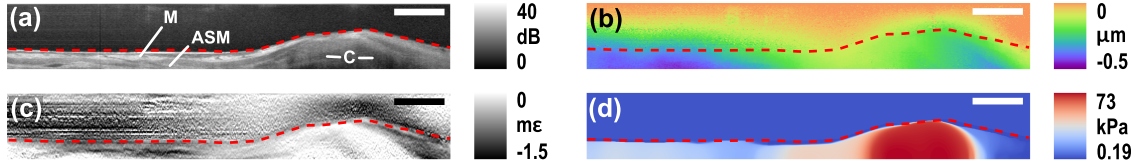


Figure 2.5: Transverse section of an equine bronchus. (a) OCT image in dB. M: mucosa, ASM: airway smooth muscle, and C: cartilage; (b) local displacement from micro-scale actuation; (c) axial strain, where $m\epsilon$ is milli-strain; and (d) shear modulus image, reconstructed by solving the elasticity inverse problem. The scale bar represents 500 μm . Red dashed lines represent the layer-tissue boundary.

calculated as the gradient of axial displacement in depth [56], which constitutes a standard elastogram that would be produced by compression OCE [57]. Although we can identify the presence of the inclusion in the strain alone, it is evident that its relation to the stiffness of the material is distorted by the effects of material property heterogeneities, particularly apparent at the boundaries of the inclusion.

The axial component of the displacement data, Fig. 2.2(b), was used to infer the spatial distribution of the shear modulus using the method described in Sec-

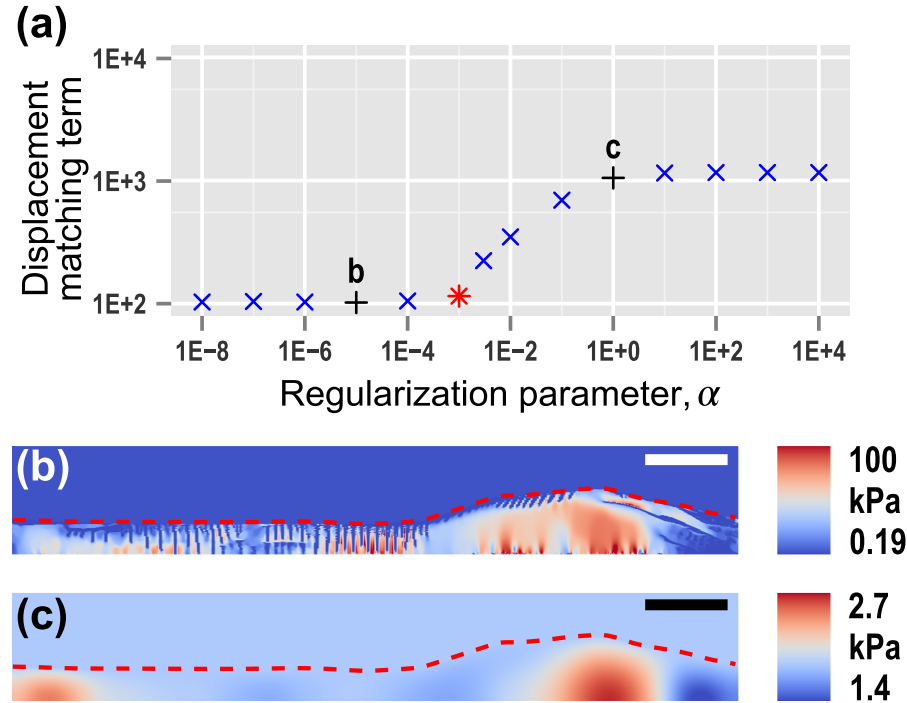


Figure 2.6: (a) Displacement matching term with respect to the regularization parameter in tissue; red star marker shows the selected optimal regularization parameter used in Fig. 2.5(d). Shear modulus images evaluated with regularization parameters labeled by black plus markers are shown in (b) as under-regularized, and (c) over-regularized. Red dashed lines represent the layer-tissue boundary.

tion 2.3.2. This was achieved by setting $T_{x_3x_3} = 1$, and all other components of \mathbf{T} to zero. The shear modulus is presented in Fig. 2.2(d). Due to the relatively large out-of-plane extent of the phantom and the compression plate, a state of plane strain was assumed within the imaging plane. The OCT intensity map was used to determine the extent of the region within this plane over which the inverse problem was solved. Specifically, points with lower OCT intensity (and hence larger displacement noise) were discarded. This led to a rectangular domain of 982 by 3,500 microns (axial by lateral), containing 300 by 350 grid points; only this domain is presented in Fig. 2.2. On every boundary edge of this region the measured displacement was prescribed as a boundary condition along the axial direction. Along the lateral direction, zero traction was assumed on all edges except the edge in contact with the compression plate (the top edge), where, due to the stickiness of the contact, zero

lateral displacement was enforced.

The value of the shear modulus in the calibration layer was held fixed at unity, and the shear modulus at every other point was determined by solving the inverse problem. This resulted in a problem with 52,150 optimization parameters. These parameters were constrained to lie in the interval (1, 20), and a uniform value of unity was used as an initial guess. The quasi-Newton algorithm used to solve the inverse problem was considered converged whenever the maximum number of iterations (6,000) was achieved, or the change in the displacement matching term over the last 5 iterations was below a certain tolerance. We note that the modulus distribution in Fig. 2.2(d) is quantitative, and is obtained by multiplying the reconstructed modulus by the known value of the shear modulus (1.9 kPa) in the calibration layer. We can see that by obtaining shear modulus, we can, to a significant extent, decouple the inclusion feature from strain artifacts. The average measured shear modulus in the inclusion and the matrix was measured to be 10.6 and 2.2 kPa, respectively, which was within 15% of the expected values. The upper and lower limits of the colormap in this and all modulus images in this paper were set equal to the minimum and maximum modulus values, respectively, within the domain.

A sweep was performed in order to determine the “optimal” value of the regularization parameter. For every value of the regularization parameter, an inverse problem was solved and the value of the displacement matching term was determined. This yielded a single data point on the curve plotted in Fig. 2.3(a). In these curves, we observe two asymptotes corresponding to small and large values of the regularization parameter. The largest value of the regularization parameter which yielded a displacement matching term close to the lower asymptote was selected to be the optimal value by using the L-curve [207]. This value ($\alpha = 0.003$) is indicated by the red marker in Fig. 2.3, and the corresponding modulus distribution is the one displayed in Fig. 2.2(d).

Maps of the reconstructed modulus at small and large values of the regularization parameter (values marked by the black markers in Fig. 2.3(a)) are shown in Fig. 2.3(b) and (c). These clearly demonstrate the smoothing effect on the modulus distribution of increasing the regularization term.

The convergence history is plotted in Fig. 2.4, where the data mismatch term and the infinity norm of the projected gradient are plotted against iteration number. In this case, the algorithm terminates due to the data mismatch convergence criterion. Meanwhile, the norm of the projected gradient is also sufficiently small. We note that though we have both convergence criteria implemented, the criterion based on data mismatch dictates for most cases.

The OCT image of the transverse section of an equine bronchus is presented in Fig. 2.5(a). The luminal side, *i.e.*, the side facing the center of the bronchus, faces the top in the OCT image. Three clearly identifiable tissue types are labeled in Fig. 2.5(a), namely: the mucosa, airway smooth muscle and cartilage. The features were classified with the aid of histological sections, and previously classified OCT images of airway tissue [208]. Similarly to the phantom results, the displacement due to the micro-scale compression is presented in Fig. 2.5(b), and a standard strain elastogram in Fig. 2.5(c). We can see that both the mucosa and the airway smooth muscle exhibit higher compressive strain than the cartilage, consistent with the expected greater stiffness of the cartilage.

The axial component of the measured displacement data was used to infer the shear modulus presented in Fig. 2.5(d). Further, a state of plane strain was assumed, and the OCT image was used to determine the region of interest (ROI) for the inverse problem. A domain of size 524 by 4,400 microns (axial by lateral), with 160 by 440 grid points, was considered, and the same kind of boundary conditions, as for the tissue-phantom case, were imposed. Again, only this domain is presented in Fig. 2.5.

The value of the shear modulus in the calibration layer was fixed at unity, which resulted in 26,379 optimization parameters, which were constrained to be in the interval (0.1, 100). Their initial value was set to unity, and the convergence criterion for the algorithm was unchanged from the tissue-phantom problem. A sweep over the regularization parameter resulted in the curve plotted in Fig. 2.6(a). This curve was used to determine the optimal value of the regularization parameter, $\alpha = 0.001$. The resulting shear modulus distribution, after rescaling by the modulus in the calibration layer (1.9 kPa), is shown in Fig. 2.5(d). In this figure, we

can clearly observe the cartilage as a very stiff region with a mean shear modulus of around 63 kPa. The modulus distributions at small and large values of the regularization parameter are shown in Fig. 2.6(b) and (c). Once again, they demonstrate the smoothing effect of the regularization term. In Fig. 2.6(b), we observe highly localized regions (just below the cartilage) where the modulus attains the upper bound (190 kPa). This lack of smoothness is a consequence of a regularization parameter that is too small for the level of noise in the measured data.

2.5 Discussion

In this paper, we have formulated quantitative OCE as an inverse problem. We have solved this problem as a constrained minimization problem, wherein the objective function is a measure of the mismatch between the measured displacement field and a predicted displacement field, which is constrained to satisfy the equations of equilibrium in conjunction with a constitutive model. The nodal values of the material parameter(s) (in this paper, the shear modulus) of the constitutive model are the optimization parameters. A gradient-based optimization algorithm is used to drive the displacement matching term to its minima by computing iterative updates to these parameters. To our knowledge, this work presents the first instance of the application of the iterative solution of the inverse elasticity problem to quantitative OCE of tissue and tissue-mimicking phantoms. As discussed below, this approach has several advantages when compared with other quantitative OCE methods.

Iterative solution of the inverse elasticity problem is consistent with completely heterogeneous stress states, which are almost always found in any specimen with heterogeneous material properties. In contrast to this, most other OCE methods assume that the axial stress component is homogeneous along the axial direction. The violation of this assumption leads to artifacts in modulus images generated using these methods. These artifacts are absent in images constructed using our approach. This can be observed in the tissue-phantom study results by comparing the strain image in Fig. 2.2 (which is typically interpreted as the reciprocal of Young's modulus) to the reconstructed shear modulus image in the same figure. The former displays artifacts at the upper corners of the inclusion that are absent in the latter.

Another advantage of iteratively solving the elasticity inverse problem is its flexibility. For example, in this paper, we have assumed that the sample is in a state of plane-strain, because (a) the width of the sample along the out-of-plane direction is much larger than that of the imaging plane (field of view), and (b) the compression plate is in contact with most of the top surface of the sample. Due to these assumptions, the out-of-plane strain components are expected to be small. On the other hand, in a typical ultrasound elastography application, such as breast elastography, the tissue is unconfined and is compressed using the transducer itself. The footprint of the transducer then only covers a small fraction of the surface of the tissue. Consequently, there is significant strain in the direction normal to the B-scan imaging plane, and the situation is closer to that of plane-stress. The approach presented here allows for both plane-strain and plane-stress (and other) scenarios by simply modifying the constitutive relation (2.3) in the forward problem. The reader is referred to [92] for results obtained under the plane-stress hypothesis.

Our approach of iteratively solving the inverse elasticity problem also allows for flexibility in including prior information about measurement noise and material parameter distributions. For example, in this paper, we have independent estimates of the shear modulus of the calibration layer, and we know that its distribution is uniform. We make use of this knowledge to fix the modulus value in the calibration layer, and to rescale the reconstructed modulus in order to obtain quantitative modulus images. Also, the lateral component of displacement is unknown. We account for this by setting all but the axial component of the tensor \mathbf{T} to zero. We note that in general this tensor should be set equal to the inverse of the covariance tensor for the noise in the displacement measurements.

The choice of the regularization term and the regularization parameter is an area of active research in inverse problems. We have used total variation (TV) regularization in this study because it penalizes variations in modulus distribution without smearing out sharp variations [203]. TV is appropriate for biomedical applications in which tissue types and/or pathologies are distinguished by sharp boundaries, which is often the case.

The regularization parameter can dramatically alter the reconstructed mod-

ulus results, with larger values leading to smoother distributions with very little contrast, and smaller values leading to sharp, noise-induced artifacts (see Figs. 2.2-2.6). An appropriate value of this parameter can be selected by using the L-curve (as was done in this paper) [207] or the Morozov discrepancy principle [209]. In the discrepancy principle, this parameter is selected so that the displacement mismatch term is approximately equal to the magnitude of the noise in the measured displacement. Both approaches are effective in determining an optimal parameter; however, both require multiple solutions of the inverse problem, which is a computationally expensive problem to solve to begin with.

The robustness of the choice for the optimal value of the regularization parameter was tested by studying the effect of varying this value on the reconstructions (results not shown here). When the regularization parameter was increased by 50%, the reconstructed contrast in the shear modulus for the tissue phantom decreased by about 5%; whereas, the contrast in the equine bronchus specimen reduced by about 20%. When the regularization parameter was decreased by 50%, the shear modulus contrast in the tissue-phantom increased by 10%, and the contrast in the equine bronchus specimen increased by about 20%. These results demonstrate that our reconstructions are robust (to within 20%) to the choice of the regularization parameter.

While the results presented in this paper validate the proposed approach and the choices made therein (plane-strain, boundary conditions, etc.), we believe that there is room for improvement in making these choices and for extensions of this approach. In particular, our plans for future work are as follows.

1. Solving the inverse elasticity problem on displacement data measured in a three-dimensional volume, to generate three-dimensional modulus images. In addition to the obvious advantage of generating volumetric modulus images, this would eliminate the plane-strain assumption and the inaccuracies that come with it. In fact, we have readily captured three-dimensional volumes of displacement previously [57] for qualitative strain imaging; however, the challenge in the reconstruction of three-dimensional modulus lies in addressing the computational expense of solving the inverse problem, which will invariably

be increased from more optimization parameters introduced by the additional dimension.

2. Measuring lateral displacement components. Including lateral displacement data will make our reconstructions more robust and will provide data for boundary conditions along the lateral direction. Although phase-sensitive methods, used in this paper, provide access to only the axial component of displacement, other methods, such as speckle tracking [210], [211], have been used to measure all displacement components. Speckle tracking, natively, has a lower sensitivity to displacement than phase-sensitive methods: however, both can in principle be used in tandem, through incremental loading, to provide high-sensitivity axial, and low-sensitivity lateral displacement measures. The variance can be readily accounted for by generating a tensor \mathbf{T} , whose components are selected in inverse proportion to the magnitude of error in displacement measurements [56]. This accounts for the spatial variation of this error, as well as the differences in the error between the axial and lateral displacement components.
3. Applying additional loads which would lead to multiple independent displacement measurements. The inverse elasticity problem with just one displacement field is non-unique in three dimensions and in two dimensions under the plane-strain assumption. The uniqueness and the robustness of this inverse problem can be improved by measuring multiple, independent displacement fields [201], [202]. One way to generate an independent field would be to compress the specimen after rotating the compression plate a little (say 10 %) about an axis that is perpendicular to the imaging plane.
4. Making incremental displacement measurements about significantly pre-stressed (about 10-30 % strain) states. These displacement measurements will provide information about the nonlinear elastic response of the specimen, and in conjunction with a nonlinear hyperelastic constitutive model could be used to create maps of the nonlinear elastic parameters of tissue [11], [92].
5. Estimating the spatial resolution sensitivity of this approach to quantitative

OCE. This is a challenging endeavor that is complicated by the fact that the resolution and sensitivity of the modulus image is determined by the resolution of the optical system, the algorithm used to estimate displacements, the spectrum of the inverse elasticity operator, the type of regularization employed in the inverse problem, the precise value of the regularization parameter, and all sources of noise.

2.6 Conclusion

We have demonstrated quantitative OCE: a method for performing quantitative elasticity imaging using compression OCE. This method is based upon the iterative solution of an inverse problem with the use of the adjoint equations to make the method computationally feasible. We applied the method to two examples: a tissue-mimicking phantom and an equine bronchus sample, both of which resulted in predicted distributions of shear modulus which were within the expected range. Although both examples were two-dimensional and within the plane-strain approximation, this method is amenable to solving three-dimensional problems. This method, is in fact, very general in that different types of prior information, boundary conditions, and tissue mechanical models can be incorporated into it. We anticipate that this approach to quantitative elasticity imaging will become an important tool in the study of biomechanics and medical imaging applications.

CHAPTER 3

Inverse Methods for 3D Quantitative Optical Coherence Elastography

3.1 Introduction

The motivation to perform elastography in biomedical engineering is explained in detail in Sec. (1.1), and the techniques that are used are described in Sec. (1.2). The strengths of quantitative elastography over conventional qualitative elastography (mainly strain imaging) are also elaborated in Sec. (1.2.2).

Among all techniques in quantitative elastography, Brendan *et al.* [68] innovatively insert a silicon layer (calibration layer hereafter) with known material properties between the compression plate and the specimen and compute the stress field on the plane right below the calibration layer. With the stress field determined in this layer, and the assumption of uniaxial stress, the Young's modulus can then be obtained by dividing stress by strain point-wise. This method is termed “algebraic inversion” in the rest of this chapter. Although the improvement of the algebraic inversion method over conventional strain imaging is obvious, such as quantitative results and relatively fewer artifacts, its assumption of a uniaxial stress state within the sample leads to artifacts when the specimen is complex.

In the method employed in this chapter a finite element model of the mechanical behavior of the tissue is constructed. The shear modulus within this model is allowed to vary spatially, and its distribution is updated iteratively until an optimal match between the displacement field predicted by the finite element model and the measured field is attained. A clear advantage of the iterative method employed in this study is its applicability to tissue and tissue constructs with heterogeneous mechanical properties.

The benefit described above comes at a higher computational cost, which has limited the application of the iterative method to two-dimensional problems [69]. In this chapter, we overcome this barrier through the use of adaptive spatial resolution and domain decomposition methods. These techniques allow us to focus

our computational effort in regions where the spatial variations in the shear modulus are most significant, and analyze different sub-regions within the tissue in parallel and independently of each other. This leads to three-dimensional shear modulus images whose spatial resolution in critical regions is close to the spatial resolution with which displacement is measured. The ability to visualize tissue structures in three dimensions has clinical benefits in applications like tumor margin assessment. It also obviates the need to make the assumption of plane stress or plane strain in our finite element model, which can lead to artifacts in the recovered shear modulus distribution.

We have applied the three-dimensional iterative method to recover the shear modulus distribution in tissue-mimicking phantoms, and *ex-vivo* and *in-vivo* tissue samples. The tissue-mimicking phantom study is used to evaluate the ability of this method to recover quantitative estimates and spatial variation of shear modulus distribution. The *ex-vivo* tissue study, which is performed on an invasive breast lesion, demonstrates its utility in identifying the tumor margins and elucidating mechanical heterogeneity within the tumor. Finally, the *in-vivo* study, which is performed on human skin points to the applicability of this approach in detection and diagnosis of diseases like skin cancer.

3.2 Results

3.2.1 Mechanical imaging of heterogeneous tissue-mimicking phantoms

In this section, we compare the performance of strain imaging, algebraic and iterative inversion methods in elastography by applying them to OCE data from tissue-mimicking phantoms with inclusions with various stiffness and shapes.

3.2.1.1 Phantom with multiple inclusions

Figure 3.1 shows various images of a phantom containing four inclusions spanning a range of shear modulus values, including one that is less than that of the bulk matrix material. The primary purpose of this figure is to compare three methods of analyzing OCE data: strain images ((e) and (h)), shear modulus retrieved using algebraic inversion ((f) and (i)) and shear modulus retrieved by iteratively solving the

elasticity inverse problem for shear modulus ((k) and (n)). The surface renderings of (c), (g) and (l) are obtained by segmenting the raw OCT, shear modulus using algebraic inversion and shear modulus obtained from iterative inversion, respectively. The average shear modulus values, along with the standard deviation, are plotted in (a) for each inclusion and for the algebraic and iterative retrieval methods, along with values of shear modulus, measured directly using a standard bulk compression test (Instron, Norwood, MA, USA). The compression test was performed on purpose-made samples that were created at the same time and from the same mixture as the inclusions. The raw OCT, strain, shear modulus and mesh images include both en-face and B-scan views, all corresponding to the same planes in each case. The dashed line in the en-face views indicate where the B-scan view intersects the en-face view.

We begin the analysis of Fig. 3.1 by noting that (a) demonstrates that, with the exception of inclusion 1 (the stiffest inclusion), the mean shear modulus obtained using a compression test falls within the range of shear modulus values obtained by iteratively solving the elasticity inverse problem. Elastography is, however, concerned with retrieving the three-dimensional distribution of shear modulus rather than bulk values. In the context of the phantom presented in Fig. 3.1, this means retrieval of the spatial distribution of shear modulus, as is depicted in Fig. 3.1 (k) and (n). Perhaps the most obvious difference between these results and their algebraic counterparts in Fig. 3.1 (f) and (i), is the homogeneity of the modulus retrieved for each inclusion by iteratively solving the elasticity inverse problem. In particular, the modulus distributions for each inclusion arising from the iterative solution are significantly more homogeneous than the algebraic case. The inclusions are physically homogeneous and so we expect the modulus distributions to be homogeneous. This demonstrates the superiority of the presented method over the algebraic method.

Aside from the homogeneity of the retrieved modulus, the retrieved inclusion shapes (Fig. 3.1l)) show good agreement with those obtained from the raw OCT data (Fig. 3.1c)). This qualitatively confirms that the spatial distribution of the shear modulus has been accurately retrieved. We note, however, that the segmentation

information arising from the raw OCT is not used in the solution of the elasticity inverse problem. The surface renderings for the iterative solution are in general smoother than those based upon the algebraic solution. This is consistent with the renderings based on raw OCT data and also with the method by which the inclusions were manufactured. This is due to two primary causes: the accuracy inherent to the iterative inversion algorithm and the adaptive nature of the mesh. The algebraic approximation to shear modulus assumes that the stress at a point within a sample is equal to the stress at the sample surface directly above that point. In this context, “directly above” means in the axial direction. The stress does, however, vary with depth, leading to artifacts in the modulus retrieved using the algebraic method. Relaxing this assumption allows for more accurate retrieval of the inclusion shapes.

The adaptive mesh also allows the solution to the elasticity inverse problem to yield more accurate inclusion shapes. The iterative solution is obtained by representing the shear modulus value on an unstructured grid (depicted in Fig. 3.1 (j) and (m)) and linearly interpolating it between grid points. The mesh that connects these grid points is comprised of tetrahedral elements, whose faces appear as triangles when they are cut by a plane. The element size thus directly determines the accuracy of the retrieved shape. In particular, the resolution of a segmented inclusion is limited by the size of elements used to solve the inverse problem. Using smaller elements where the gradient of the shear modulus is large, thus allows for more accurate inclusion shape retrieval. In general we conclude from this that the adaptive mesh approach allows for the recovery of interfaces between materials of different shear modulus with greater accuracy and resolution.

3.2.1.2 Phantoms with single inclusion

Similarly, we apply the strain imaging, algebraic and iterative inversion methods to other tissue-mimicking phantoms with a stiff cuboid inclusion and a stiff star-shaped inclusion. Following the same analysis as the multi-inclusion case in Sec. (3.2.1.1), it is not hard to arrive at the same conclusions, that is the superiority of the iterative inversion method over conventional strain imaging and the algebraic inversion method. Moreover, we note that in the presence of local tension, the al-

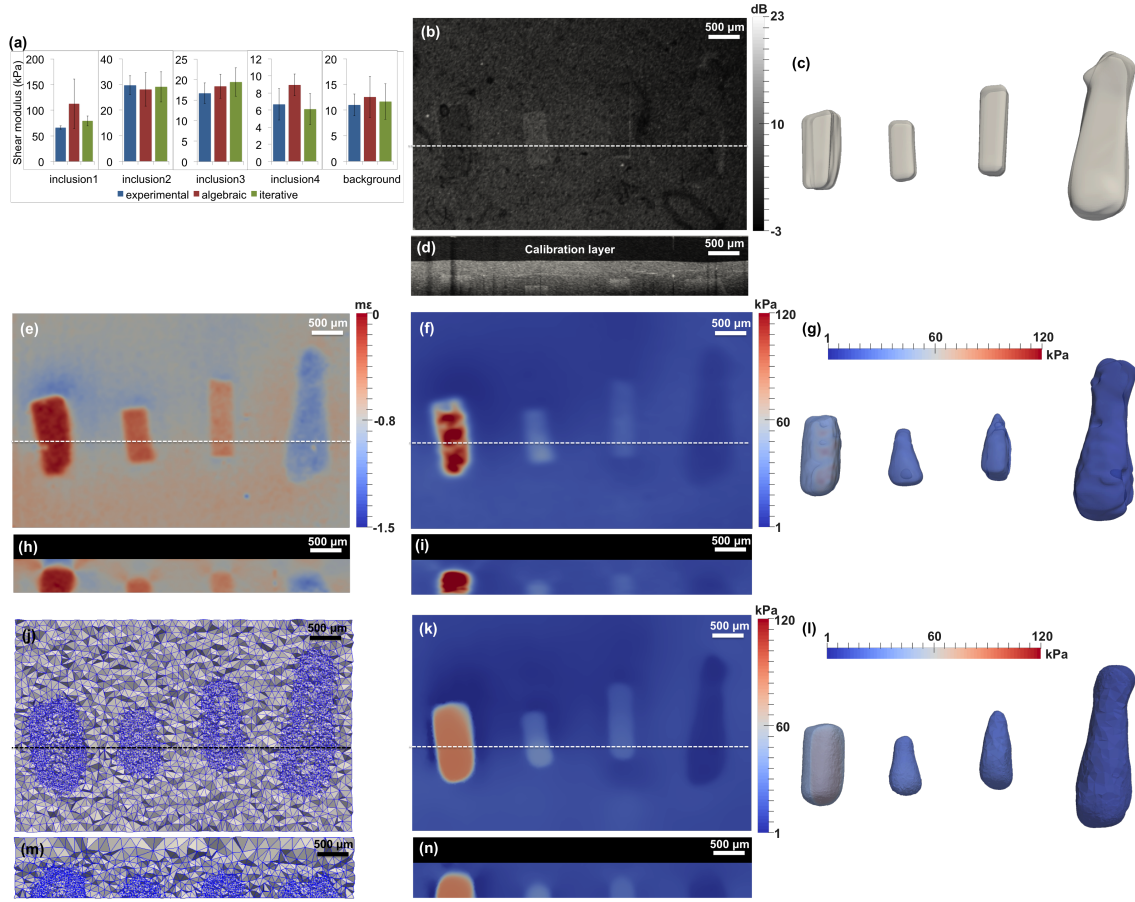


Figure 3.1: OCE of tissue-mimicking phantom with multiple inclusions. (a) Average shear modulus and its variance for the experimental test, the algebraic method, and the iterative method. *En-face* (b), B-scan (d), and segmented (c) images from OCT data. *En-face* (e), and B-scan (h) images of strain data. *En-face* (f), B-scan (i), and segmented (g) images of shear modulus from algebraic inversion. *En-face* (j), and B-scan (m) images of the mesh generated during iterative inversion. *En-face* (k), B-scan (n), and segmented (l) shear modulus images from iterative inversion.

gebraic inversion method can result in negative modulus, as indicated by the void regions in Figure 3.2 (f) and Figure 3.3 (f) and (i).

3.2.2 *Ex-vivo* mechanical imaging of malignant breast tumor

Fig. 3.4 demonstrates our study on the freshly exercised breast tissue. Tumor, adipose and stroma tissues can be observed in Fig. 3.4 (a). In Fig. 3.4 (b-d), we

observe that though the adipose and stroma structures are still visible, the OCT signal in the tumor region is dissipated substantially. OCE was performed to retrieve stiffness information of the tissue. In Fig. 3.4 (e,g,h) which correspond to strain images, we observe very oscillatory strain patterns below and above zero. Fig. 3.4 (f,i,j) were created using algebraic inversion. We can observe large void regions, which correspond to locations where the modulus was computed as being negative.

Fig. 3.4 (k) is the segmented tumor region from algebraic inversion. By employing the adaptive grids as shown in Fig. 3.4 (l,n,o), the shear modulus distribution is reconstructed as shown in Fig. 3.4 (m,p,q). The final grid is refined in regions where the shear modulus gradient is large. The two elliptical tumor regions are shown in Fig. 3.4 (r). These regions correspond to two distinct foci of the tumors, and the low shear modulus in the center of these tumors is likely due to necrosis.

We note that the stroma region has a much lower modulus than the tumor itself. This is likely because the calibration layer was more compressed above the tumor to ensure contact over the entire surface of the tissue. Since malignant tumors have been shown to display nonlinear elastic behavior, this meant that the tangent modulus over these regions was elevated. It is perhaps due to this reason that the recovered shear modulus in the tumor was higher than in the stroma.

Since the modulus reconstruction was performed on an *ex-vivo* sample of tissue, we can think of this study as a mechanical biopsy. In particular, the approach described in this study provides a rapid way to probe the mechanical properties of tissue at high spatial resolution. This method will likely find applications in understanding the mechanical changes that accompany and promote tumorigenesis. It is also likely to find applications in quantifying the margins of the excised tissue after a surgical procedure in order to ensure that the entire extent of the tumor has been removed.

3.2.3 *In-vivo* mechanical imaging of skin

Figure 3.5 shows *in vivo* OCE of a human fingertip, similarly demonstrating the performance of the algebraic and iterative methods of retrieving tissue elasticity. OCT images (a-c) show the structure of the fingertip. The *en face* region in

(a) spans three papillary ridges (fingerprint). B-scans, sectioned at locations in (a) identified by the dashed line, readily distinguish layers of the skin, from top to bottom: the stratum corneum (SC), a protective layer of dead anucleated keratinocytes (corneocytes); the living sections of the epidermis (E); and the dermis (D), typically comprising dense irregular connective tissue. Sweat glands can also be seen in (b) and (c).

Strain images (d-f) show some capacity to distinguish the ridged and layered structure of the skin. The algebraic (g-i) and iterative (k-m) reconstructions of shear modulus exemplify this contrast. In (g) and (k), a higher modulus in the ridges is observed. In depth ((h), (i), (l), (m)), a variation in the shear modulus is observed corresponding to the skin layers. The mean shear modulus values for the three layers are: 24 kPa (SC), 27 kPa (E), and 32 kPa (D), which are within the range reported previously [212]. Direct comparison of shear modulus is challenging because in the OCE results we are compressing the tissue first, and then measuring what amounts to a tangent modulus.

Skin tissue is highly heterogeneous, thus, a high mesh density is desired. Performing inversion over the entire tissue volume with a high mesh density is computationally demanding. This is made feasible through domain decomposition, where multiple independent inversions were performed, still on the entire domain, however, with separate complementary partitions being refined with a dense mesh. The results from each refined partition in each inversion were fused together to obtain a full, high-resolution reconstruction of shear modulus.

The use of iterative inversion presents a number of advantages over the algebraic inversion. In the algebraic inversion (g-i), white masked-out areas represent where a negative modulus was estimated. In such areas, the principal component of compressive strain is likely to be orthogonal to the loading direction, thus, showing up as tensile strain in the z direction. Such scenarios cannot be handled with the assumption of local uniaxial stress. Furthermore, the iterative approach is superior in identifying local features, such as the sweat ducts. In the 3D segmentation of the fingertip, the iterative method (n) is able to visualize individual sweat ducts (labeled by red arrows, with corresponding OCT images (o) and (p)). It is challenging to

see these features in the algebraic reconstruction (j).

Accurate mapping of mechanical properties *in vivo* in skin may find important clinical applications in dermatology, such as in characterizing cancer [16], pathological scarring [213] and scleroderma [214]. Further, it may find applications in the cosmetics industry, where the mechanical properties of skin are important in aging, treatment and regeneration [215]. First steps toward this with OCE have been recently demonstrated, showing the capacity to further distinguish burn scars, moles and image other locations of the skin, however, still with the algebraic approach [216].

The use of iterative inverse methods in *in vivo* data presents a new set of challenges. In tomographic acquisition (where the data is acquired sequentially across each location), movement in the tissue, such as bulk movement and blood flow, can generate areas of discontinuity in displacement or the coordinate system. In an iterative inverse method that rigorously adheres to the assumption of incompressibility and continuity, this may cause significant artifacts.

3.3 Discussion

We have presented an approach to iteratively solving for the three-dimensional sample shear modulus distribution from OCE data. The solution is found by solving a constrained minimization problem whereby a modulus distribution is found which minimizes the difference between measured and predicted displacement. We employ a gradient-based optimization algorithm which takes advantage of an adjoint problem to efficiently calculate the gradient of the mismatch functional with respect to the sample's three-dimensional shear modulus distribution. We have applied the solution method to three heterogeneous tissue-mimicking phantoms, *ex-vivo* malignant breast tumour and *in-vivo* human skin. The phantom examples verify that the solution method accurately retrieves modulus distributions in three-dimensional heterogeneous samples with what believe is unprecedented accuracy. Mesh refinement and computational domain decomposition allows for shear modulus to be retrieved with a finer spatial resolution and accuracy for a given sample dimension and computer hardware. The solution method is free of unrealistic assumptions such as

the sample having uniform stress or the plane strain and plane stress assumptions inherent to two-dimensional approximations. Although we assume that the sample is linear elastic, incompressible and isotropic, the solution framework could be extended to relax these assumptions. The primary challenge in relaxing such assumptions is the development of a suitable forward model and the acquisition of the required data from the sample. At the same time as relaxing assumptions, it is also possible to seamlessly incorporate prior information into the solution method. This was done in the presented work where a calibration layer of known shear modulus was used. This allowed the magnitude of shear modulus throughout the sample to be retrieved absolutely.

The presented modulus retrieval method results in modulus maps from three-dimensional data with fewer artifacts. This results from requiring fewer restrictive assumptions, clear examples of which are given in modulus distributions retrieved for the heterogeneous phantoms of Fig. 3.1, Fig. 3.2 and Fig. 3.3. We believe the method’s ability to obtain modulus maps for heterogeneous samples is unparalleled. The iterative solution method also implicitly solves the problem sometimes referred to as ”mechanical coupling”, whereby features within a sample perturb the perceived mechanical response of other features within a sample.

This work will enable images of sample shear modulus to be obtained with improved spatial resolution and accuracy. Higher spatial resolution is achieved through the use of mesh refinement which means that small mesh elements are used only where they are required, as dictated by the sample. The improved accuracy of the retrieved modulus distributions has been demonstrated in the presented examples. Aside from simply providing ”clearer” images of tissue mechanical properties, it will also allow for the development of objective clinical diagnosis methods based upon absolute values of tissue shear modulus. In research applications, it will allow for new approaches for longitudinal studies due to the retrieval of absolute shear modulus values.

3.4 Methods

3.4.1 Construction and characterization of phantom

This part of effort was carried out by our collaborators at University of Western Australia. It is included here sake of completeness. Tissue-mimicking phantoms and the compliant stress layers were fabricated from two-compound room-temperature vulcanizing silicone. Two compounds were used: Elastosil P7676 and ELastosil RT601 (Wacker Chemie AG, Munich, Germany). The optical properties were controlled though the addition of titanium dioxide particles of known size distribution. The refractive index of the silicones is 1.4 and 2.5 for the titanium dioxide [205]. The mechanical properties were controlled by changing the mixing ratio of the two components of the silicone (parts A and B), and further varied by diluting the silicone parts with polydimethylsiloxane (PDMS) oil (AK50, Wacker Chemie AG, Munich, Germany). PDMS oil was also used to lubricate the samples to minimize friction in the experiments. Each composition is presented as Compound A:B:Oil (e.g., P7676 2:1:0.3). The phantom mixture was mixed and sonicated to ensure uniform distribution of constituents and scatterers, and was oven-cured at 80°C.

The compliant stress layers were fabricated from P7676 1:1:0 with no added scattering. The layers were fabricated to a 500- μm thickness.

The bulk of the four-inclusion phantom was fabricated from P7676 1:1:0, and the inclusions were fabricated from (in order of descending modulus): RT601 5:1:0, RT601 10:1:10, RT601 10:1:30 and P7676 2:1:0.3. 1 g/L of titanium dioxide was added to the bulk and 2.5 g/L was added to the inclusions to provide optical contrast. Each inclusion material was fabricated independently and then manually cut into roughly rectangular shape, and incorporated into the bulk during its curing process. Each inclusion was roughly 6 \times , 3 \times , 1.5 \times and 0.5 \times the bulk stiffness, with actual values shown in Fig. 3.1(a).

3.4.2 Preparation of breast tumor sample

This part of effort was carried out by our collaborators at University of Western Australia. It is included here sake of completeness. The imaging system acquired B-scans and C-scans in 0.1 s and \sim 16 min, respectively. 3D dataset was acquired

with dimensions ($x \times y \times z$) up to $10 \times 10 \times 2.25$ mm, comprising 1,000 A-scans in each B-scan and 10,000 B-scans in each C-scan. The data was acquired using a custom-made software package written in C++. Signal processing of the raw data was performed in Matlab (Mathworks, USA, v2012b).

Informed consent was obtained from patients and the study approved by the Human Research Ethics Committee of Royal Perth Hospital, Perth, Western Australia. The sample was imaged, taken from a 60-year-old female undergoing mastectomy and classified as invasive ductal carcinoma. After excision, a fresh tissue sample was dissected for scanning, with approximate dimensions ($x \times y \times z$) of $1.5 \times 1.5 \times 0.5$ cm. Samples were kept hydrated in saline until imaging, which occurred within 4 hours of excision. After imaging, samples were fixed in 10% neutral buffered formalin, embedded in paraffin, sectioned and stained with haematoxylin and eosin (H&E) following the standard histopathology protocols used at Royal Perth Hospital. The H&E-stained sections were digitally micrographed using an automated system (ScanScope, Leica Biosystems, Nussloch, Germany) and manually co-registered with the corresponding *en face* OCT images using in-house viewing software. Interpretation of histology was performed by an experienced pathologist (B. Latham).

3.4.3 Preparation of skin sample

This part of effort was carried out by our collaborators at University of Western Australia. It is included here sake of completeness. Skin imaging was approved by the University of Western Australia Human Research Ethics Committee. Imaging was performed on a 26-year-old Caucasian male. Prior to imaging, the fingertip was cleaned and lubricated with PDMS oil. The compliant layer was also lubricated and placed on top of the fingertip. The finger was placed on a cushion to minimize discomfort and movement. The imaging probe was then applied to the fingertip, preloading it until there were no qualitatively observable movement artifacts and bulk motion in the displacement images. It was also preloaded to ensure that there was complete contact, and that all layers were straining due to compression.

3.4.4 OCE system and displacement estimation

This part of effort was carried out by our collaborators at University of Western Australia. It is included here sake of completeness. The Fourier-domain OCT system used to perform OCE is described in detail in [57]. Compression OCE was performed by placing the specimen on top of a $600\text{-}\mu\text{m}$ thick compliant poly-dimethylsiloxane (PDMS) silicone layer of known material properties. As demonstrated in the previous Chapter, this calibration layer can constrain the solution to the inverse elasticity problem to be absolute. The specimen-layer assembly was placed between a rigid plate and a glass window coupled to a piezoelectric ring actuator [56]. 5 – 10% preload strain was applied with the rigid plate to ensure even contact. Phase-sensitive OCE was used to estimate axial displacement components within the range of $\pm 2.2\mu\text{m}$ [57], [199].

3.4.5 Inverse problem solution

We split the domain of interest, Ω , into the volume occupied by the calibration layer Ω_c and the volume occupied by the tissue, Ω_t . We let (x, y, z) denote the lateral, axial and elevational coordinates within the domain of interest, and $\tilde{u}(x, y, z)$ denote the axial component of measured displacement increment. We model the calibration layer as well as the tissue as incompressible elastic materials. Within the calibration layer we measure the average axial strain through the thickness, $\epsilon_c(x, z)$ that is applied to ensure proper contact. This, in conjunction with the knowledge of the elastic behavior of the calibration material allows us to calculate the tangent shear modulus, $\mu_c(x, z)$, within the calibration layer.

The inverse problem we wish to solve is: given \tilde{u} and μ_c determine the spatial distribution of the shear modulus, $\mu(x, y, z)$ in the tissue. This problem is supplemented by the constraint that the equations of equilibrium must be satisfied. We solve this problem as a minimization problem, where we seek to find the distribution μ that minimizes the functional

$$\pi = \int_{\Omega_t} (u - \tilde{u})^2 dx + \alpha \int_{\Omega_t} \sqrt{|\nabla \mu|^2 + c^2} dx. \quad (3.1)$$

In the equation above, the first term is the data mismatch term and the second

term is the regularization term. In the data mismatch term u is the predicted displacement field which is constrained to satisfy the equations of equilibrium for a linear, incompressible elastic solid. The regularization term, which is of the total variation type (TV), addresses the ill-posedness of the inverse problem and penalizes large variations in the recovered Young's modulus. It does so, without regard to the steepness of the slope of these variations. In this term, α is the regularization parameter, and c is another parameter that ensures that this term has continuous derivatives (wrt. to μ) when $\nabla\mu = 0$.

We note that the shear modulus, μ , influences the data mismatch term indirectly via the predicted displacement, u , since the spatial distribution of μ determines u through the solution of the equations of equilibrium. Any change in μ leads to a change in u , which changes the data mismatch term. The goal is to find the distribution of μ that minimizes the sum of the mismatch and the regularization terms. This is accomplished by representing both μ and u using the standard finite element basis functions, and then using a gradient-based quasi-Newton algorithm to solve the minimization problem (3.1). The gradient vector, whose components represent the rate of change in π due to change in the value of μ at a finite element vertex, is determined by solving the forward problem (equations of equilibrium) and an adjoint problem.

The algorithm described above is efficient; however its cost can become prohibitive when solving problems in three dimensions on a fine grid. For example, if we were to apply this algorithm to the problem of a tissue- mimicking phantom with a single inclusion (see Fig. 3.2), we would solve for 31 million optimization variables, which is very challenging. To address this challenge, we propose two novel approaches.

Adaptive mesh refinement

First, when solving the inverse problem we make use of adaptive spatial resolution. In particular, we first solve the inverse problem on a coarse grid. Thereafter we define a mesh size field that is inversely proportional to the absolute value of the gradient of the recovered Young's modulus. This leads to a new finite element mesh

that has finer resolution wherever the shear modulus varies sharply. We repeat this step several times and arrive at a final mesh whose resolution is optimal for the problem at hand. The mesh is fine where the gradients in μ are large, and coarse in other places. As shown in Fig. 3.6, we use the tissue-mimicking phantom with a single stiff inclusion as an example to explain the adaptive approach. In Fig. 3.6, each row corresponds to one adaptive stage. The grids are gradually refined at the interface between the inclusion and the bulk matrix. As a continuation strategy, the solution from the previous stage is used in the immediate following stage. The adaptive grids make full use of the measured displacement data and achieve similar resolution as the displacement measurement grid in the finest regions, as can be seen from the first column of Fig. 3.6. The effect of the adaptive grids can also be observed from the recovered shape of the inclusion as shown in the second column of Fig. 3.6.

Domain decomposition

The approach described above works well for problems with a large field of view and relatively few significant features. In cases where there are many features within the field of view, this approach will lead to a fine resolution everywhere, and therefore a very large computational problem. In order to tackle these types of problems, we combine this approach with a domain decomposition method. In this approach the overall problem is simultaneously solved on N distinct meshes. In each mesh an adaptive strategy is applied to a smaller subdomain of the total volume, and a fixed, coarse mesh is used in the rest of the domain. The fact that the adaptive strategy is applied to a single subdomain in each problem allows us to focus on the features contained within that subdomain, and the fact that the region outside this subdomain is represented through a coarse discretization, allows us to account for the effect of the remainder of region without expending large computational resources. Another advantage of this method is that it is “embarrassingly parallelizable.” That is each of the N problems described above can be solved independently of each other on separate processors or computers, with no communication. This approach is applied to the *in-vivo* fingertip tissue problem due to the very hetero-

geneous structure of skin tissues. In this case, the large problem is divided into three subproblems as shown in Fig. 3.7 (a) and (b), (c) and (d), (e) and (f), where adaptive grids are applied in the regions within the orange box and the rest of the domain is kept uniformly coarse. The three subproblems are solved simultaneously and the solution from each of the refined regions are stitched together as shown in Fig. 3.7 (g) and (h).

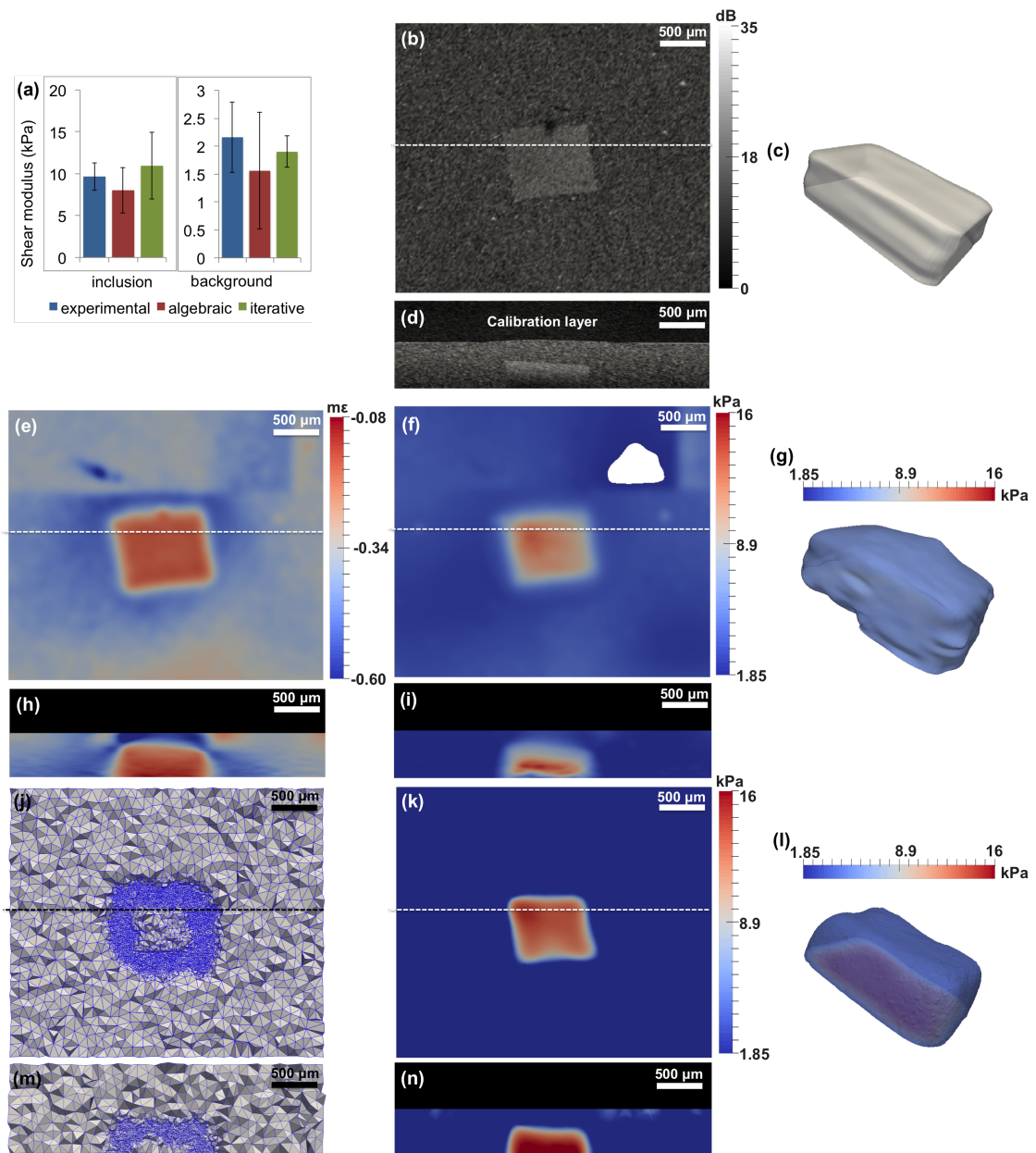


Figure 3.2: OCE of tissue-mimicking phantom with single inclusion. (a) Average shear modulus and its variance for the experimental test, the algebraic method, and the iterative method. *En-face* (b), B-scan (d), and segmented (c) images from OCT data. *En-face* (e), and B-scan (h) images of strain data. *En-face* (f), B-scan (i), and segmented (g) images of shear modulus from algebraic inversion. *En-face* (j), and B-scan (m) images of the mesh generated during iterative inversion. *En-face* (k), B-scan (n), and segmented (l) shear modulus images from iterative inversion.

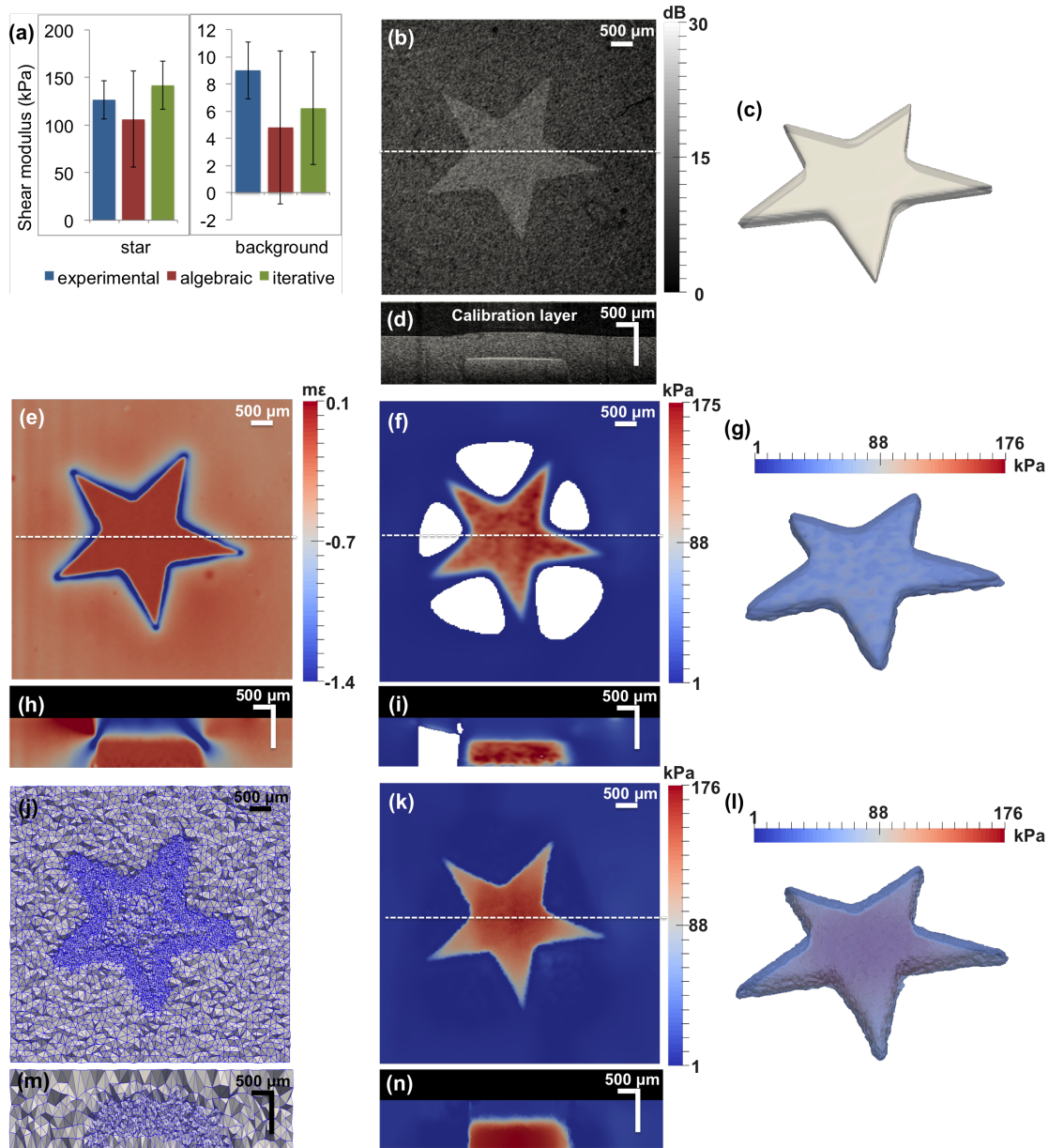


Figure 3.3: OCE of tissue-mimicking phantom with star inclusion. (a) Average shear modulus and its variance for the experimental test, the algebraic method, and the iterative method. *En-face* (b), B-scan (d), and segmented (c) images from OCT data. *En-face* (e), and B-scan (h) images of strain data. *En-face* (f), B-scan (i), and segmented (g) images of shear modulus from algebraic inversion. *En-face* (j), and B-scan (m) images of the mesh generated during iterative inversion. *En-face* (k), B-scan (n), and segmented (l) shear modulus images from iterative inversion.

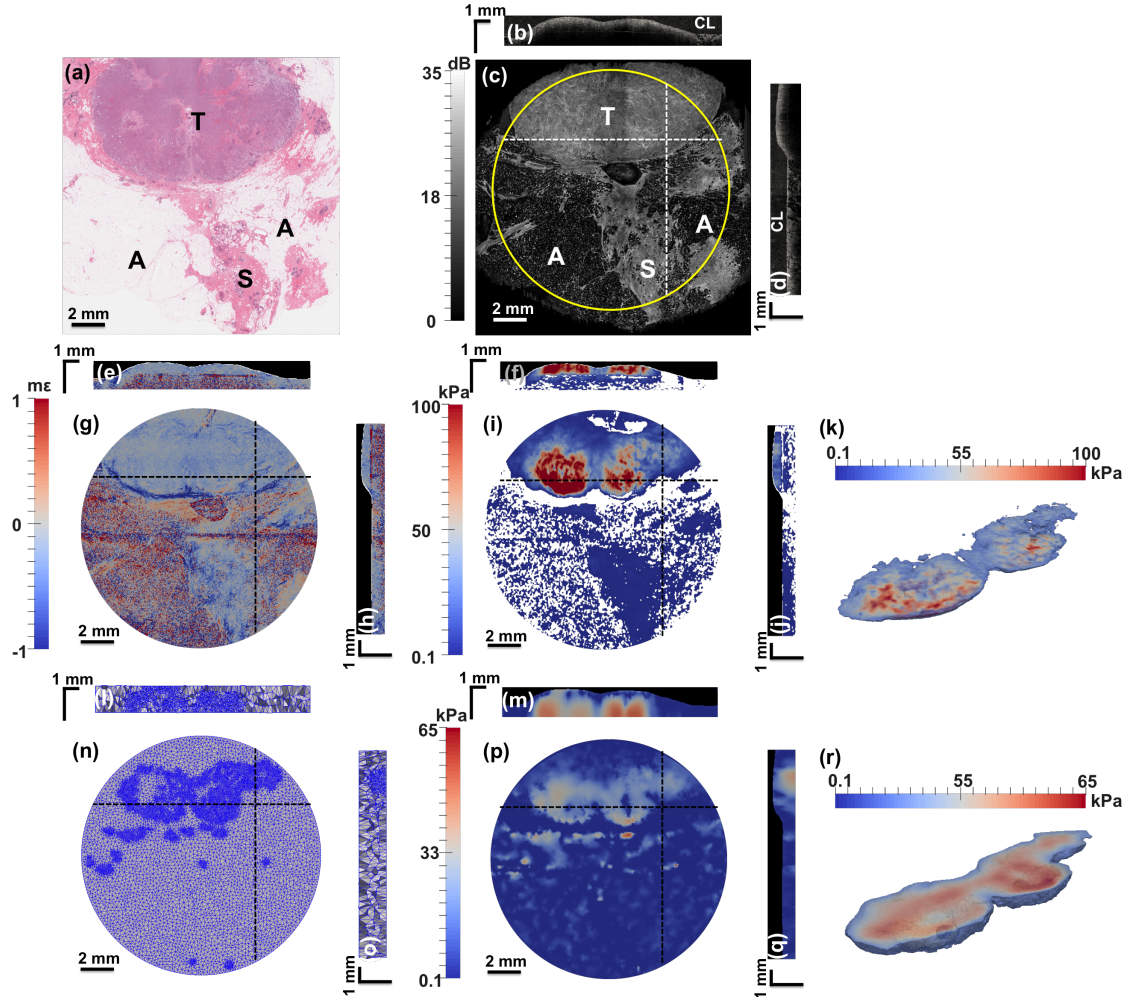


Figure 3.4: *Ex vivo* OCE of a malignant breast tumor. (a) H&E histology. B-scan (b) and (d), and *en-face* (c) images from OCT data. B-scan (e) and (h), and *en-face* (g) images of strain data. B-scan (f) and (j), *en-face* (i), and segmented (k) images of shear modulus from algebraic inversion. B-scan (l) and (o), and *en-face* (n) images of the mesh generated during iterative inversion. B-scan (m) and (q), *en-face* (p), and segmented (r) images of shear modulus from iterative inversion. A = adipose, S = stroma, T = tumor, CL = calibration layer.

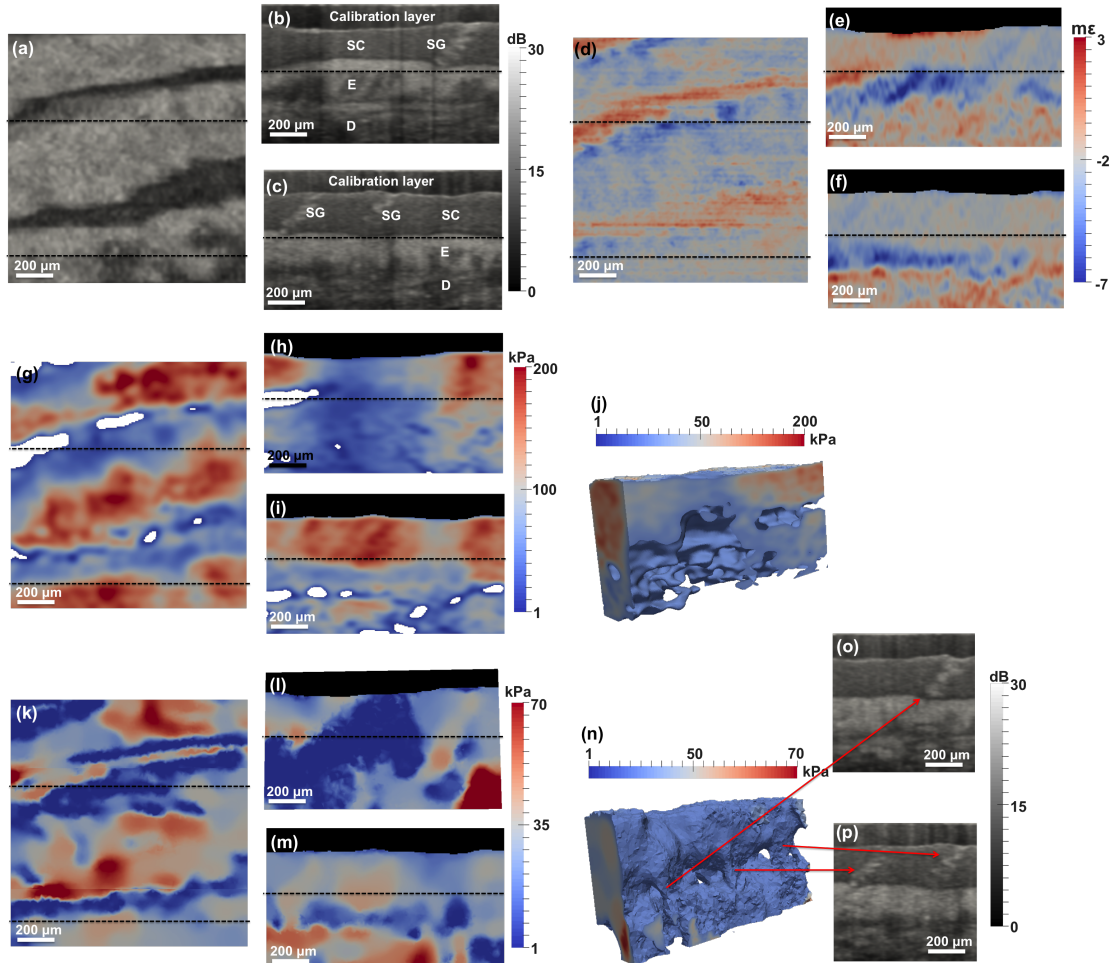


Figure 3.5: *In vivo* OCE of fingertip tissue. *En-face* (a), and B-scan (b), (c), (o) and (p) images from OCT data. *En-face* (d), and B-scan (e) and (f) images of strain data. *En-face* (g), B-scan (h) and (i), and segmented (j) images of shear modulus from algebraic inversion. *En-face* (k), B-scan (l) and (m), and segmented (n) images of shear modulus from iterative inversion. SC = stratum corneum, E = epidermis, D = dermis, SG = sweat gland.

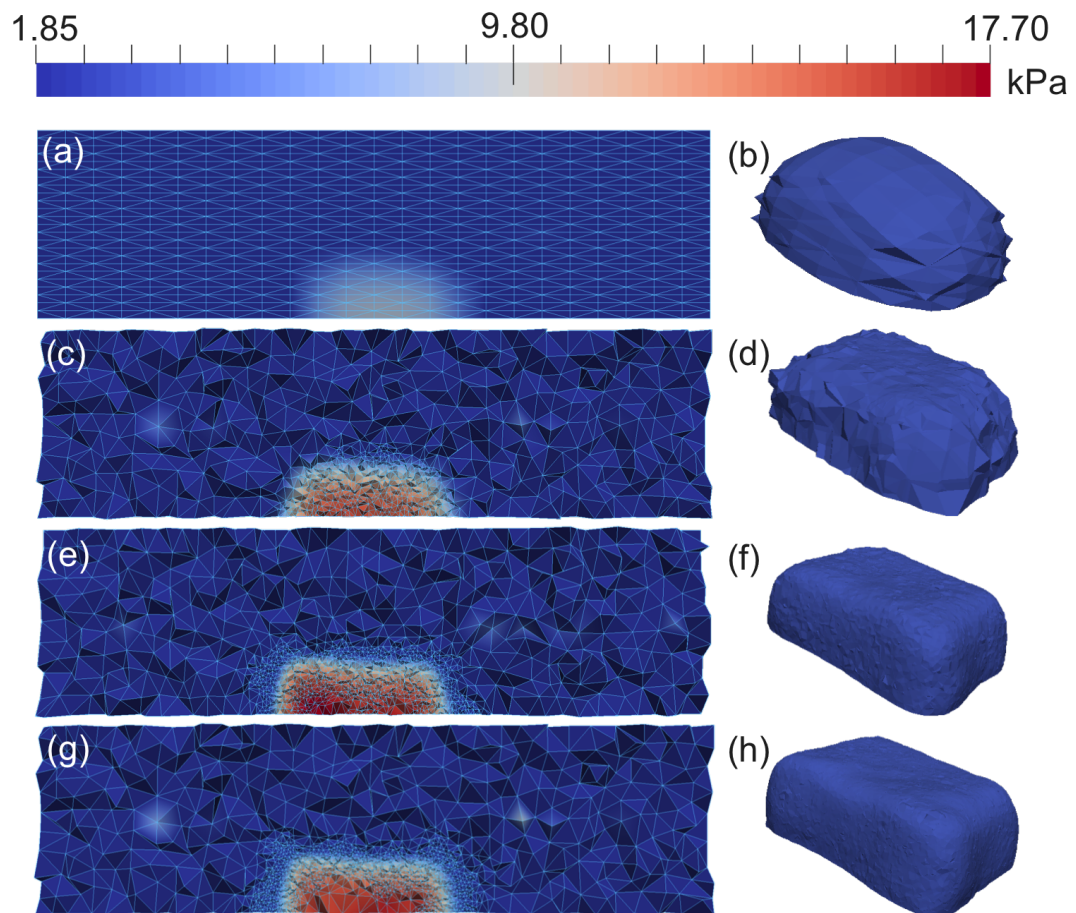


Figure 3.6: Illustration of adaptive mesh refinement. First column (a,c,e,g) displays the adaptive grids in the B-scan view in different adaptive stages. Second column (b,d,f,h) displays the segmented shapes of the inclusion in different stages.

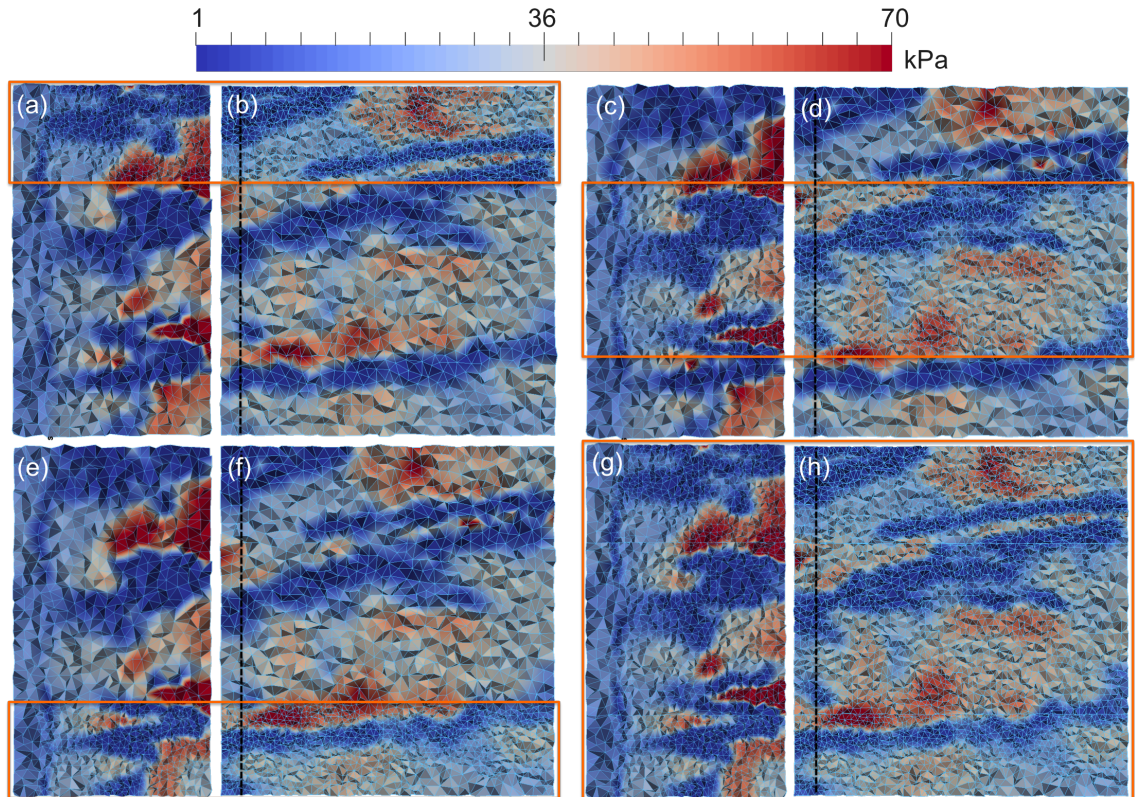


Figure 3.7: Illustration of domain decomposition. (a) and (b), (c) and (d), (e) and (f) are the three subproblems. (g) and (h) are the composite solution. (a), (c), (e) and (g) are the B-scan planes of (b), (d), (f) and (h) on the black dashed lines, respectively. Orange boxes indicate the regions with refined mesh.

CHAPTER 4

Recovery of Cellular Traction in Three-Dimensional Nonlinear Hyperelastic Matrices

4.1 Introduction

The traction exerted by a cell on its surroundings (and by the surroundings on a cell) plays a critical role in cell development and migration, and is therefore important in understanding and manipulating important biological processes such as stem cell differentiation, cancer cell metastasis, and embryonic morphogenesis [217]–[219]. In order to quantitatively measure the traction field, several techniques have been developed. These include the use of wrinkling membranes [127], cantilever-based sensing devices [133], [220] and traction force microscopy (TFM)[140], [221], [222].

In TFM, the extracellular matrix (ECM) surrounding the cell is embedded with beads, and the motion of these beads in response to cellular tractions is tracked. Given this motion, and the mechanical behavior of the extracellular matrix, the traction at the cell-matrix interface is recovered [144]. When TFM is applied to a thick, two-dimensional, linear-elastic substrate, the problem of determining the tractions is further simplified by utilizing the Boussinesq solution [158] in the Fourier space. This technique is often referred to as Fourier Transform Traction Cytometry (FTTC)[140], and yields a rapid solution for the traction field. However, its application is limited to thick two-dimensional substrates undergoing small strains.

The extension of TFM to three dimensions is considered in [144]. This reference describes an approach to TFM for cells that are geometrically complex and are embedded in a three-dimensional matrix. This problem is solved by constructing a numerical Green’s function using the finite element method that connects the traction applied at a point on the cell-matrix interface to the displacement at a given

Portions of this chapter previously appeared as: L. Dong and A. A. Oberai, “Recovery of cellular traction in three-dimensional nonlinear hyperelastic matrices,” *Comput. Methods in Appl. Mech. Eng.*, vol. 314, pp. 296–313, Feb. 2017.

bead location. Once this map is determined, a minimization problem is solved in order to determine the traction field that produces a bead displacement field that best matches the measured displacement field. A similar approach can also be found in [223].

A natural extension to the ideas described above would involve accounting for the nonlinear effects during the elastic deformation of the ECM. There are several sources of this nonlinear behavior:

1. When the strain in a solid exceeds a certain threshold (usually around 10%), the linear measure of strain (the infinitesimal strain tensor) is no longer appropriate, and other nonlinear measures that accurately measure the deformation of the material must be adopted [224]–[226]. We note that in TFM studies, where 30-70% strains are quite common [144], [159], [160], this level of strain is routinely exceeded.
2. When the displacement incurred by the solid is large, the change in the current configuration due to this displacement must be accounted for, and this introduces the so-called geometric nonlinearity to the problem.
3. Some materials display a nonlinear stress-strain response, and this leads to a nonlinear constitutive model. This is especially true for materials such as gelatin-agar co-gels [227], that are commonly used as tissue-mimicking phantom, or real biological gels [228].

For all these reasons, it is important to consider the nonlinear behavior of the ECM while computing the traction field exerted by the cell on the matrix.

We note that there have been some attempts at solving the 3D nonlinear TFM problem. In [229], the authors consider a nonlinear constitutive model, but do not account for nonlinearities in strain and in the geometrical description of the problem. Moreover, the applicability of their technique appears to be limited to a small range of traction magnitudes, and to a relatively small number of traction beads.

We also note that there are instances adopting a “forward computation method” (described as such by [230]) for determining the cell traction, in contrast to the inverse problem approach described above [142], [153], [154], [222], [231]. In the forward

method, the strain is obtained by differentiating the experimentally measured displacement field and the stress/traction fields are then determined by applying the constitutive equation. Clearly, the quality of the cellular tractions recovered using this approach depends heavily on the ability to measure the displacement field close to the cell-matrix interface [230]. This places a significant burden on the experimental set up. The inverse problem approach, on the other hand, can make use of all available bead displacement data, including those that are at some distance from the interface.

In this manuscript we present a new approach to solving the nonlinear TFM problem. We pose the problem as an inverse problem, where we are given the displacement of a finite number of beads, and a model for the the mechanical response of the matrix, and we wish to determine the traction field that is consistent with these observations. We solve the inverse problem as a constrained minimization problem, where we seek to find the traction field that yields a displacement field that best matches measured bead displacements. This is done under the constraint that the predicted displacement field satisfies the equations of equilibrium for a non-linear hyperelastic material. We solve this problem using gradient-based algorithms, and efficiently compute the gradient using an linearized adjoint equation. We account for noise by regularizing the recovered traction field through a Tikhonov term. Similar methods for solving inverse problems have been used to determine the spatial distribution of material properties in different fields of mechanics and physics [11], [39], [78], [91], [92], [95], [98], [103], [107]–[113], [168], [202], [232], [233]. We test the performance of the proposed approach on synthetic data. We create geometric models of cells embedded in a matrix with known material behavior. Thereafter, we apply tractions at the cell-matrix interface and compute the displacement field in the matrix by solving a forward problem. We utilize a portion of the displacement field as the “measured” displacement field, and in some instances, add noise to it. Using this measured displacement in our algorithm, we determine the traction field at the interface. We also utilize this set-up to determine the effect of making the linear elastic assumption while solving the inverse problem, when the actual response of the material is nonlinear. In the inverse problems literature, this error is referred

to as model error. We conclude that for some problems the model error can be significant. Last but not least, we apply our algorithm with linear elasticity to two *in-vitro* problems, human umbilical vein endothelial cells (HUVECs) embedded in stiff and soft hydrogels, respectively. This proves the applicability of our algorithm to real data. We also explain the difficulties in directly applying our algorithm with nonlinear elasticity to real data.

Moreover, we note that the problem of recovering tractions is not limited to applications in biomechanics, and has also been studied in structural dynamics [234]–[236]. In these studies also, the assumption of linear elasticity is invoked.

The organization of the remainder of this manuscript is as follows: In Section 4.2, we present the nonlinear forward elasticity problem that describes the response of a three-dimensional hydrogel to cellular traction. In Section 4.3, we formulate the nonlinear inverse problem to determine the traction field at the cell-matrix interface, given the “experimentally measured” displacements. We also present the essential ingredients of our solution strategy which include a gradient-based minimization algorithm, an adjoint equation, and a special regularization approach. In Section 4.4, we describe two numerical examples that include tractions exerted on a hydrogel by a microglial cell and a neuronal cell. We use these examples to quantify and understand errors in the reconstructed traction field due to noise as well as incorrect model selection. In Section 4.5, we apply our algorithm with linear elasticity to HUVECs in stiff and soft hydrogels, respectively, and explain the difficulties in directly applying our algorithm with nonlinear elasticity to real data. We conclude with a summary in Section 4.6.

4.2 The forward elasticity problem

A typical problem of interest consists of a cell embedded within a three-dimensional scaffold made from a hydrogel. It is assumed that the mechanical properties of the cell are not known, while that of the gel are known [140], [144], [221], [231]. In this study, the hydrogel around the cell is modeled as an incompressible hyperelastic solid using a modified version of the Blatz (or the Veronda-Westmann) model. Treating hydrogel as incompressible is common [140], [144], [221], [231]. In addition,

several commonly used hydrogels, such as agar-gelatin co-gels, display significant nonlinear elastic behavior in range of strains encountered in cell-traction studies. For these types of gels the modified Blatz model is a simple constitutive model (with just 2 parameters) that captures the nonlinear stress-strain response.

4.2.1 Strong form

The problem is posed on the domain obtained by subtracting the cell from the hydrogel. Typically, the extent of the hydrogel is too large to fully model in this problem, so the domain is truncated at a certain distance away from the cell where the displacements (due to cellular tractions) have decayed significantly. This truncation is common [143], [144], [229], and the truncation distance usually depends on how fast the traction decays. Authors in [143], [144], [222] have presented some nice illustrations of the decay of tractions.

The displacement field, \mathbf{u} , and the pressure, p , within the hydrogel obey the equations of equilibrium given by:

$$\nabla \cdot \mathbf{P} = \mathbf{0} \quad \text{in } \Omega_0, \quad (4.1)$$

$$\mathbf{u} = \mathbf{g} \quad \text{on } \Gamma_g, \quad (4.2)$$

$$\mathbf{P} \cdot \mathbf{N} = \mathbf{h} \quad \text{on } \Gamma_h, \quad (4.3)$$

along with the incompressibility constraint:

$$J - 1 = 0, \quad \text{in } \Omega_0. \quad (4.4)$$

Here Eq.(4.1) is a statement of equilibrium in the reference configuration Ω_0 , where \mathbf{P} is the first Piola-Kirchhoff stress tensor, and Eqs.(4.2) and (4.3) define the Dirichlet (displacement) and Neumann (traction) boundary conditions, respectively, where the displacement data, \mathbf{g} , is prescribed on Γ_g , and the traction data, \mathbf{h} , is prescribed on Γ_h . Further, $\partial\Omega_0 = \overline{\Gamma_g \cup \Gamma_h}$ defines the closed boundary of Ω_0 , $\Gamma_g \cap \Gamma_h = \emptyset$, and \mathbf{N} is the outward normal vector on the surface, Γ_g , in the reference configuration. Eq.(4.4) enforces the incompressibility constraint, and $J = \det(\mathbf{F})$ is the jacobian of the deformation gradient, which is defined as $\mathbf{F} = \nabla \mathbf{u} + \mathbf{1}$.

These equations are appended with a constitutive equation for the stress. In particular, first Piola-Kirchhoff stress tensor is given by $\mathbf{P} = \mathbf{F}\mathbf{S}$, where \mathbf{S} , the second Piola-Kirchhoff stress tensor, is defined as, $\mathbf{S} = -J \times p\mathbf{F}^{-1}\mathbf{F}^{-T} + 2\frac{\partial W}{\partial \mathbf{C}}$. In the expression above, W is the strain energy density function that depends on the invariants of the right Cauchy-Green strain tensor, $\mathbf{C} = \mathbf{F}^T\mathbf{F}$. For the constitutive model used in this paper, W is given by

$$W = \frac{\mu}{2\gamma}(e^{\gamma(J^{-\frac{2}{3}}I_1-3)} - 1), \quad (4.5)$$

where μ is the shear modulus at zero strain, and γ is the nonlinear parameter that determines the nonlinear change of stress with strain. Further, $I_1 = \text{trace}(\mathbf{C})$, is the first principal invariant of the Cauchy-Green strain tensor. More details about this material model can be found in [110], [237]–[239].

4.2.2 Weak form

We solve the forward problem using the finite element method, which is based on the weak, or the variational form, of the forward problem. The variational form may be derived by either minimizing the total potential energy of the system under the constraint of incompressibility, or it may be derived by multiplying the equilibrium equation and the incompressibility equations with weighting functions, integrating over Ω_0 , performing integration-by-parts on the former, and then imposing the traction boundary condition Eq.(4.3). In either case, we arrive at the following statement: Find $\mathbf{U} \equiv [\mathbf{u}, p] \in \mathcal{S} \times \mathcal{P}$ such that

$$\mathcal{A}(\mathbf{W}, \mathbf{U}) = (\mathbf{w}, \mathbf{h})_{\Gamma_h}, \quad \forall \mathbf{W} \equiv [\mathbf{w}, q] \in \mathcal{V} \times \mathcal{P}, \quad (4.6)$$

where

$$\mathcal{A}(\mathbf{W}, \mathbf{U}) \equiv \int_{\Omega_0} \nabla \mathbf{w} : \mathbf{P} d\Omega + \int_{\Omega_0} q(J-1) d\Omega, \quad (4.7)$$

$$(\mathbf{w}, \mathbf{h})_{\Gamma_h} \equiv \int_{\Gamma_h} \mathbf{w} \cdot \mathbf{h} d\Gamma. \quad (4.8)$$

The function spaces \mathcal{V} , \mathcal{S} , and \mathcal{P} that appear in the equations above are defined as,

$$\mathcal{V} = \{\mathbf{w}|w_i \in H^1(\Omega_0); w_i = 0 \text{ on } \Gamma_g\}, \quad (4.9)$$

$$\mathcal{S} = \{\mathbf{u}|u_i \in H^1(\Omega_0); u_i = g_i \text{ on } \Gamma_g\}, \quad (4.10)$$

$$\mathcal{P} \subseteq L_2(\Omega_0), \quad (4.11)$$

where L_2 is the space of square-integrable functions, and H^1 is the Sobolev space of square-integrable functions with square-integrable derivatives.

The standard Galerkin finite element method is obtained by restricting the weak form (Eq.4.6) to finite-dimensional function spaces. However, for incompressible materials, it is well known that the Galerkin finite element method leads to unstable solutions unless very specific choices are used for the displacement and pressure function spaces. This restriction can be overcome by stabilizing this formulation with residual-based terms [240], [241]. With that addition, the discrete stabilized formulation is given by: Find $\mathbf{U}^h \equiv [\mathbf{u}^h, p^h] \in \mathcal{S}^h \times \mathcal{P}^h$ such that

$$\mathcal{A}_s(\mathbf{W}^h, \mathbf{U}^h) = (\mathbf{w}^h, \mathbf{h})_{\Gamma_h}, \quad \forall \mathbf{W}^h \equiv [\mathbf{w}^h, q^h] \in \mathcal{V}^h \times \mathcal{P}^h, \quad (4.12)$$

where

$$\mathcal{A}_s(\mathbf{W}^h, \mathbf{U}^h) \equiv \mathcal{A}(\mathbf{W}^h, \mathbf{U}^h) - \sum_{e=1}^{n_{el}} (\tau \nabla \cdot (\mathbf{F}^h \mathbf{S}^h), \mathbf{F}^{h-T} \nabla q^h)_{\Omega_0^e}. \quad (4.13)$$

The second term in Eq.4.13 represents the stabilization term. The subscript Ω_0^e indicates that the L_2 inner product is evaluated in the interior of the e -th element, and the stabilization factor, $\tau = \frac{\alpha h^2}{2\mu}$, where $\alpha \approx 0.5$, and h is the characteristic element length. A detailed discussion of this stabilization method can be found in [110]. In our implementation, all variables, including displacement, pressure and traction, are represented by bilinear finite element basis functions.

4.3 Inverse problem for the traction vector field

In this section, we consider the inverse problem of determining the traction field, \mathbf{h} , on the boundary, Γ_h , given measured displacements at discrete locations in the hydrogel. The overall scheme to obtain the solution of this inverse problem is similar to that of the material property identification inverse problem described in [110] and [109]. The key difference is that we wish to recover the traction, \mathbf{h} , and not the material properties. In the terminology of the PDE-constrained optimization, this inverse problem can be viewed as a boundary source inversion since the optimization variable \mathbf{h} appears on the right hand side in Eq.4.12. In most PDEs, right hand side is the source term. The inverse problem is formulated as a minimization problem subject to the constraint of satisfying the forward problem. A gradient-based optimization approach, L-BFGS [156], is used to solve the minimization problem iteratively and the gradients are efficiently evaluated by solving the appropriate adjoint equation [98]. Similar use of the adjoint method to efficiently compute gradients can also be found in other applications [242]–[245].

4.3.1 Inverse problem statement

The inverse problem is stated as follows: Given the measured displacement field, $\tilde{\mathbf{u}}$, find the traction field, \mathbf{h} , such that the objective function

$$\pi(\mathbf{u}, \mathbf{h}) = \frac{1}{2} \|\mathbf{T}\mathbf{u} - \mathbf{T}\tilde{\mathbf{u}}\|_0^2 + \alpha \mathcal{R}(\mathbf{h}) \quad (4.14)$$

is minimized subject to the constraint that the predicted displacement field, \mathbf{u} , satisfies Eqs.(4.1)-(4.4).

In Eq.(4.14), the first term is the displacement matching term. The mismatch between the predicted and measured displacement field is measured in the L_2 norm denoted by $\|\cdot\|_0$. It is weighted by the tensor \mathbf{T} , which can be used to augment the contributions from the more accurate components of measured displacements. The second term of Eq.(4.14) is the regularization term, where α is the regularization parameter. The regularization term embeds prior information about the unknown field, in our case the traction field, \mathbf{h} , into the inverse problem. In most cases, it is assumed that the recovered field is smooth in a sense defined by the choice of

this term. This has the effect of regularizing the inverse problem, which is typically ill-posed, as it lacks uniqueness or stability. In this manuscript, Tikhonov (H_1) regularization [246] and total variation diminishing(TVD) regularization[203] are implemented:

$$H_1 \text{ regularization : } \mathcal{R}(\mathbf{h}) = \frac{1}{2} \int_{\Gamma_h} |\nabla_\Gamma \mathbf{h}|^2 d\Gamma \quad (4.15)$$

$$\text{TVD regularization : } \mathcal{R}(\mathbf{h}) = \int_{\Gamma_h} |\nabla_\Gamma \mathbf{h}| d\Gamma. \quad (4.16)$$

In the equations above, ∇_Γ represents the gradient operator restricted to the surface Γ_h . At any location $\mathbf{x} \in \Gamma_h$, it is given by $\nabla_\Gamma \equiv (\mathbf{1} - \mathbf{N} \otimes \mathbf{N})\nabla$, where $\mathbf{1}$ is the identity tensor, \mathbf{N} is the outward normal to the surface and ∇ is the gradient operator. We note that ∇_Γ only retains the tangential components of ∇ . The H_1 -regularization term penalizes gradients of \mathbf{h} and leads to smooth solution. The TVD regularization also penalizes gradients but does so without regard to the steepness. More accurately, it penalizes the total variation of \mathbf{h} . For fields that have rapid variations, the TVD regularization represents a more accurate means to convey the prior information, and is preferred. One disadvantage of the TVD term is its lack of smoothness when $\nabla \mathbf{h} = 0$. At these locations, the derivative of the TVD term with regard to \mathbf{h} is discontinuous, and this causes difficulties when it is used in conjunction with algorithms that work with approximations of the Hessian of the minimization functional. In this case, the TVD is smoothed about $\mathbf{h} = 0$ by replacing Eq.(4.16) with

$$\mathcal{R}(\mathbf{h}) = \int_{\Gamma_h} \sqrt{|\nabla_\Gamma \mathbf{h}|^2 + \beta^2} d\Gamma, \quad (4.17)$$

where $\beta \ll |\nabla_\Gamma \mathbf{h}|$ is a small positive constant [247]. In the following sections, H_1 regularization is applied to the numerical examples and TVD regularization is applied to experimental data since the true traction fields in the numerical examples are smooth and traction fields are considered less smooth in actual experiments.

4.3.2 Formulation of the gradient

In order to solve the inverse problem using a quasi-Newton method, we need to evaluate the derivative of π with respect to \mathbf{h} . This is relatively easily evaluated for the regularization term. However, its evaluation for the displacement mismatch term is cumbersome. This is because the predicted displacement field, \mathbf{u} , depends upon \mathbf{h} implicitly through the constraint of Eq.(4.12). This difficulty is circumvented through the use of an appropriately chosen adjoint field, which is derived by constructing the Lagrangian corresponding to π . That is,

$$L(\mathbf{U}^h, \mathbf{W}^h, \mathbf{h}) = \pi(\mathbf{u}^h, \mathbf{h}) + \mathcal{A}_s(\mathbf{W}^h, \mathbf{U}^h) - (\mathbf{w}^h, \mathbf{h})_{\Gamma_h}, \quad (4.18)$$

where $\mathbf{W}^h \in \mathcal{V}^h \times \mathcal{P}^h$ and $\mathbf{U}^h \in \mathcal{S}^h \times \mathcal{P}^h$. Here \mathbf{W}^h plays the role of a Lagrange multiplier field.

We denote the variation of a function $f(x)$ in the direction δx by δf ,

$$\delta f = D_x f \cdot \delta x = \left. \frac{d}{d\epsilon} f(x + \epsilon \delta x) \right|_{\epsilon \rightarrow 0}. \quad (4.19)$$

The variation of L is given by

$$\delta L = D_{\mathbf{U}^h} L \cdot \delta \mathbf{U}^h + D_{\mathbf{W}^h} L \cdot \delta \mathbf{W}^h + D_{\mathbf{h}} L \cdot \delta \mathbf{h}. \quad (4.20)$$

Setting $D_{\mathbf{W}^h} L \cdot \delta \mathbf{W}^h = 0$, $\forall \delta \mathbf{W}^h \in \mathcal{V}^h \times \mathcal{P}^h$ in the above equation immediately yields an equation for \mathbf{u}^h , that is

$$\mathcal{A}_s(\delta \mathbf{W}^h, \mathbf{U}^h) = (\delta \mathbf{w}^h, \mathbf{h})_{\Gamma_h}, \quad \forall \delta \mathbf{W}^h \in \mathcal{V}^h \times \mathcal{P}^h. \quad (4.21)$$

This implies that \mathbf{U}^h satisfies the forward problem Eq.(4.12). Under this condition, from Eq.(4.18), we conclude $\pi = L$, and hence $\delta \pi = \delta L$.

We now examine the condition for which the expression for δL can be further simplified. In particular, we set $D_{\mathbf{U}^h} L \cdot \delta \mathbf{U}^h = 0$, $\forall \delta \mathbf{U}^h \in \mathcal{V}^h \times \mathcal{P}^h$ to arrive at

$$\mathcal{B}_s(\mathbf{W}^h, \delta \mathbf{U}^h; \mathbf{U}^h) = -(\mathbf{T} \delta \mathbf{u}, \mathbf{T} \mathbf{u} - \mathbf{T} \tilde{\mathbf{u}}), \quad \forall \delta \mathbf{U}^h \in \mathcal{V}^h \times \mathcal{P}^h. \quad (4.22)$$

where $\mathcal{B}_s(\mathbf{W}^h, \delta\mathbf{U}^h; \mathbf{U}^h) \equiv \frac{d}{d\epsilon}\mathcal{A}_s(\mathbf{W}^h, \mathbf{U}^h + \epsilon\delta\mathbf{U}^h)|_{\epsilon \rightarrow 0}$ is the linearization of $\mathcal{A}_s(\cdot, \cdot)$ about \mathbf{U}^h . Eq.(4.22) yields a well-posed linear problem for \mathbf{W}^h . The left hand side of this problem is the adjoint of the linearized version of the original forward problem Eq.(4.12). For this reason, this problem is referred to as the adjoint problem, and \mathbf{W}^h the adjoint field.

With \mathbf{U}^h given by the primal problem Eq.(4.21) and \mathbf{W}^h given by the adjoint problem Eq.(4.22), we have from Eq.(4.20)

$$\delta L = \delta\pi = D_h L \cdot \delta\mathbf{h} = \alpha D_h \mathcal{R} \cdot \delta\mathbf{h} - (\mathbf{w}^h, \delta\mathbf{h})_{\Gamma_h}, \quad (4.23)$$

where \mathcal{R} is the regularization term defined by Eq.(4.15). As a result, the algorithm to calculate the change in the objective function corresponding to a change in the traction vector proceeds as follows:

1. Solve Eq.(4.21) to determine the primal field $\mathbf{U}^h = [\mathbf{u}^h, p^h]$.
2. Solve Eq.(4.22) to determine the adjoint field $\mathbf{W}^h = [\mathbf{w}^h, q^h]$.
3. Use \mathbf{w}^h in Eq.(4.23) to determine the variation in the objective function.

In this study, the optimization variables are the traction components at each node on the cell-matrix interface. The value of the objective function, Eq.(4.14), and its gradient, Eq.(4.23), are the input for the L-BFGS optimization algorithm, which returns an updated estimate of tractions for each node and the whole process is repeated until convergence or until the maximum number of iterations is achieved.

Remark

We note that the primal problem, Eq.(4.21), is a system of nonlinear equations which is solved using the Newton method. This represents the major computational cost of our algorithm. This cost is kept in check by utilizing a continuation scheme described in [110] and [109]. Within this approach, when solving the forward traction problem for a new guess of the traction field, the solution from the previous step is used as an initial state. Consequently, the forward problem is solved within 10 Newton iterations, as opposed to on the order of 100 iterations otherwise.

4.4 Numerical examples

In this section, two geometrically accurate cell models are used to demonstrate the applicability of our nonlinear algorithm in recovering cell traction. In each case, a known traction field, $\hat{\mathbf{h}}$, is applied at the cell-matrix interface and the forward problem is solved. This results in the displacement of the matrix which is sampled at some select nodes. We denote this displacement vector by $\hat{\mathbf{u}}^{(j)}, j = 1, \dots, n_{node}$. In some cases, in order to simulate the effect of instrument noise and errors in the displacement estimation algorithm in actual experiments, noise is added to this displacement. The noisy “measured” displacement field is given by

$$\tilde{\mathbf{u}}^{(i)} = \hat{\mathbf{u}}^{(i)} + \eta \times \frac{\sum_{j=1}^{n_{node}} |\hat{\mathbf{u}}^{(j)}|}{\sum_{j=1}^{n_{node}} |\mathbf{n}^{(j)}|} \times \mathbf{n}^{(i)}, i = 1, \dots, n_{node} \quad (4.24)$$

where $|\cdot|$ denotes the magnitude of a vector, $n_k^{(j)} \in N(0, 1)$, $k = 1, 2, 3$ and $N(0, 1)$ is standard normal distribution. In this case, η , represents the fraction of noise in the “measured” displacement field. The effect of this parameter on the quality of the reconstruction is examined.

In order to quantify the performance of our algorithm, the difference between the recovered traction field, \mathbf{h} , and the applied traction field, $\hat{\mathbf{h}}$, is measured,

$$e(\mathbf{h}) = \frac{\|\mathbf{h} - \hat{\mathbf{h}}\|_0}{\|\hat{\mathbf{h}}\|_0}. \quad (4.25)$$

For simplicity, a weight of unity is selected for the entire displacement vector, which means that the tensor, \mathbf{T} , in Eq.(4.14) is set to the identity tensor. In order to be unbiased, the initial guess for the traction field is set to 0. Also, the regularization parameter for the following results in this paper was obtained by solving the inverse problem with different values of the regularization parameter, and plotting the variation of displacement mismatch term as a function of the regularization parameter (the so-called L-curve [248]). See Figure 4.1, for the L-curve for a typical case considered in this study. The quasi-Newton iterations were considered “converged” when the relative change in the displacement matching term over the last five iterations was smaller than 1×10^{-8} .

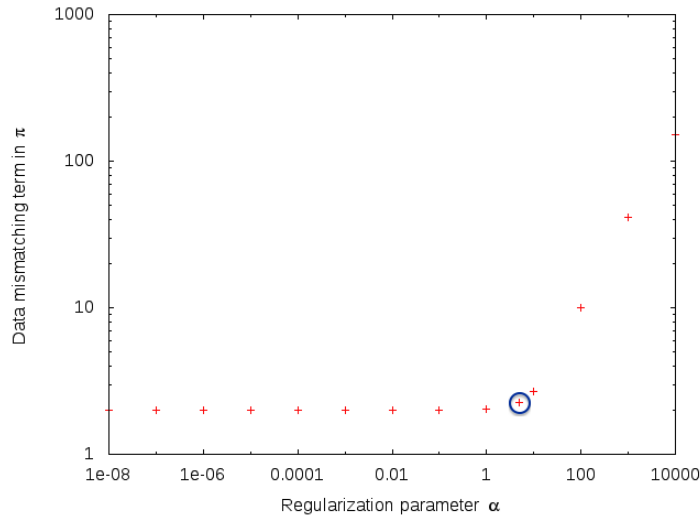


Figure 4.1: L-curve for the microglial cell model with nonlinear effects and 1% noise.

4.4.1 Microglial cell model

The 3D model of the microglial cell (see Figure 4.2a) is reconstructed through a set of pictures of z-stack microscopy (image courtesy of Sebastian Rhode at Carl Zeiss Microscopy and Sabine Scheibe) with ImageJ [249] and meshed with Simmodeler (Simmertrix.Inc, New York, US). The cell is about $20 \mu\text{m} \times 20 \mu\text{m} \times 15 \mu\text{m}$ and is contained within a cubical matrix with an edge length of $100 \mu\text{m}$. The finite element mesh is comprised of 9,641 vertices and 51,544 tetrahedral elements. Out of these, the vertices that are on the surface of the cell, and beyond a sphere of $50 \mu\text{m}$ diameter, are treated as location without beads. That is the displacement field from these locations is not used in solving the inverse problem. This gives us a total of 7,023 bead locations to work with. The exclusion of other locations helps us in avoiding the “inverse crime” of using all the forward data in the inverse problem. It is also consistent with the experimental protocol where most of the beads that are close to the cell are tracked [250]. We note that the number of beads considered in this study is comparable to experiments [144] and is much more than some of the state-of-the-art cell traction recovery algorithms can handle [223], [229].

In the numerical experiments reported here, the shear modulus, μ , of the matrix is set to either 400 Pa or 600 Pa. The values lie within the range of commonly

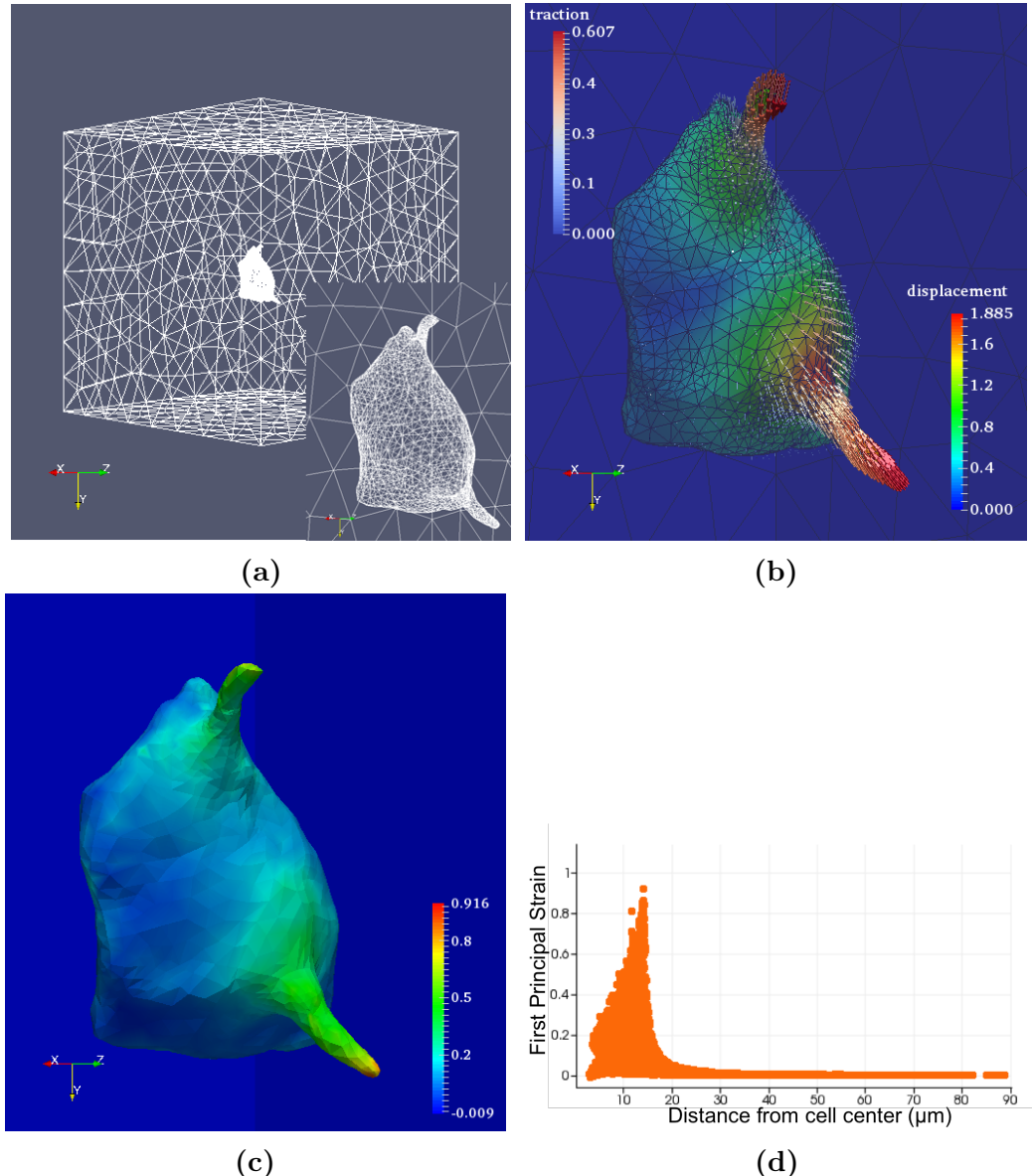


Figure 4.2: Microglial cell: (a) Mesh on the exterior surface and the cell-matrix interface. Results of the simulated forward problem on the deformed surface with $\gamma = 1$. (b) Arrows display the traction field (in kPa), and the deformed surface is colored by the displacement magnitude in μm . (c) The first principal component of the Green-Lagrange strain tensor. (d) Distribution of the strain at the bead locations as a function of distance from the center.

used experimental hydrogels, extracellular matrices and real tissues [144], [251], [252]. The dimensionless nonlinear parameter, γ , in the modified blatz model is set to either

1 or 5. With $\gamma = 1$ the material behaves linearly up to about 100% strain, and with $\gamma = 5$ it starts to deviate from linear behavior at about 15% strain [110]. All six surfaces of the box are assumed fixed in the x , y and z directions ($u_x = u_y = u_z = 0$).

As shown in Figure 4.2b, the traction field is applied such that it is maximum along the two protrusions of the cell, and is smoothly interpolated between these regions. The direction of the traction field is roughly pointed to the center of the cell. This loading condition simulates the contraction of the matrix close to the cell after the cell is lysed with detergent [144].

In the following sections, we consider the effect of material and geometric nonlinearity in recovering the traction vector field. In the first section, we set $\gamma = 1$ so that within the range of strains considered, the matrix behaves like a linear elastic solid. Thereafter, we consider $\gamma = 5$, where the material displays a nonlinear elastic response. We note that while gelatin substrates tend to be linear elastic for large values of strain, gelatin-agar substrates display nonlinear elastic behavior at relatively small ($\approx 15\%$) strains [227].

Linear material ($\gamma = 1$)

The shear modulus for the matrix is set to 400 Pa. In Figure 4.2b, we observe that the largest tractions are applied at the tips of the cell, and the magnitude drops as we approach the center of the cell. The traction pulls each arm of the cell toward the center of the cell. The resulting displacement fields are maximum at the tip of the arms, and at the connections between arms and the rest of the cell. Significant strains are generated on the cell-matrix interface, and are illustrated in Figures 4.2c, where we have plotted the first principal component of the Green-Lagrange strain tensor. We note that this strain ranges from about 50% to 90% on the arms - Figure 4.2d. The large strain indicates that the use of a linear measure of strain is inappropriate for this problem.

For each set of “measured” displacements (with 1% and without noise), the traction field was reconstructed using either a finite strain or an infinitesimal strain model. The resulting traction vector fields are shown in Figure 4.3. We observe that while the spatial variation of these fields is very similar, their magnitudes are

significantly different. This is made clear by computing the error, $e(\mathbf{h})$, in the reconstructed traction field (see Figure 4.4). For the no-noise case with the finite strain model, this error is 4.23%, and with the infinitesimal strain model it is 12.7% (regularization parameters = 0.0001 and 1, respectively). When 1% noise is added to the displacements, the error is 12.75% for the finite strain model, and 20.7% for the infinitesimal strain model (regularization parameters = 5 and 10, respectively). The difference between these two errors, which is around 8%, is therefore the error incurred in incorrectly making the infinitesimal strain assumption. Here we note that the infinitesimal strain assumption is often made [140], [144], [221]–[223], [229]. Figure 4.1 displays the L-curve for the case with finite deformation and 1% noise as a typical curve for the cases considered in this paper. According to [248], the value of the regularization parameters at the point of largest curvature is the “optimal” regularization parameter. For the example considered in this curve, this corresponds to $\alpha = 5$ (circled in blue in Figure 4.1). We use this approach to find the regularization parameters for all cases in this paper. For the sake of brevity, we do not show all the L-curve plots.

Nonlinear material ($\gamma = 5$)

In this case when solving the forward problem, in order to generate the “measured” data, the shear modulus for the matrix is set to 600 Pa, and the nonlinear parameter is set to $\gamma = 5$. The traction field is identical to the $\gamma = 1$ case described above. The traction field and the displacement magnitude are shown in Figure 4.5. We observe that when compared with the linear elastic case, the displacement for this case is smaller. In examining the image for the principal component of the Green-Lagrange strain, we observe that the maximum strain is also much smaller (approximately 40% as opposed to 90%). This is attributed to the higher shear modulus and the larger values of the nonlinear parameter in this case. This leads to a large value of the tangent modulus for the matrix, particularly at large values of strain. Given that the traction vector field for the two cases is the same, a larger elastic tangent modulus implies a small overall strain.

Once again two cases were considered: one with no noise and one with 1%

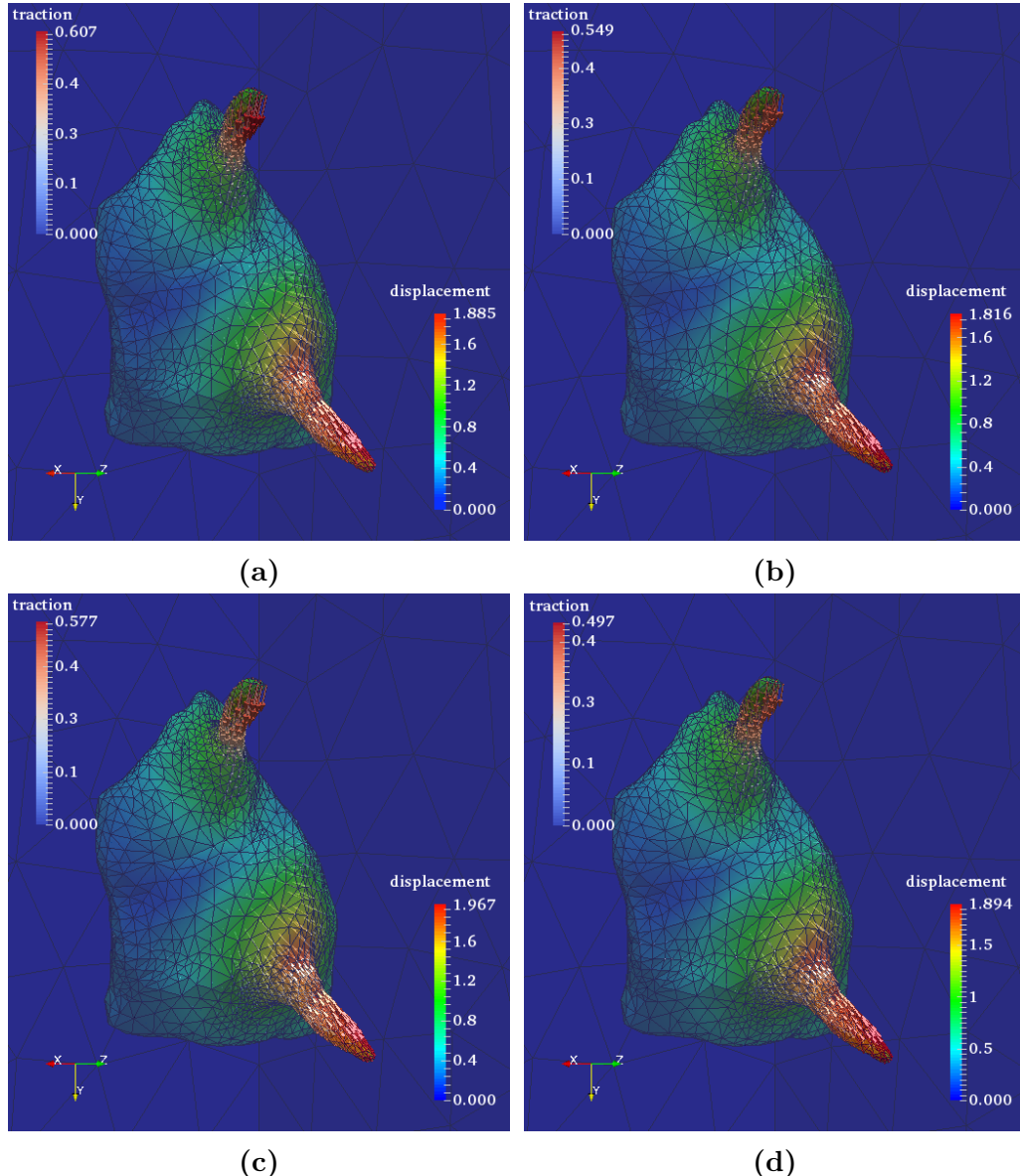


Figure 4.3: Results of the inverse analysis for the microglial cell on the deformed surface with $\gamma = 1$. Arrows display the recovered traction field (in kPa), and the deformed surface is colored by the recovered displacement magnitude in μm . (a) Solution with nonlinear effects and 0% noise. (b) Solution with nonlinear effects and 1% noise. (c) Solution without nonlinear effects and 0% noise. (d) Solution without nonlinear effects and 1% noise.

noise. For each case, two inverse problems were solved. In one problem, the matrix deformation was treated with a finite strain theory and the appropriate nonlinear

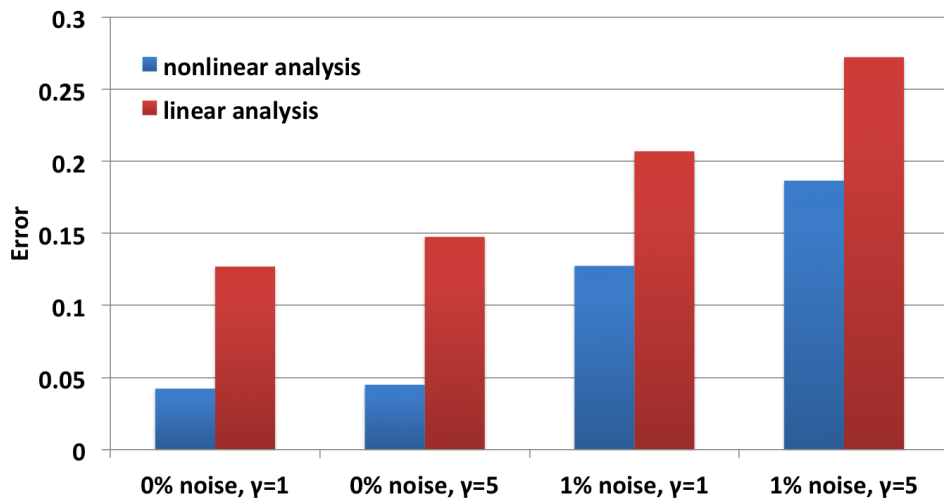


Figure 4.4: Error summary for the microglial cell model.

elastic model was utilized. In the second problem, the deformation was incorrectly treated as linear elastic, and an infinitesimal strain model was used. The resulting traction vectors are shown in Figure 4.6. The spatial distribution of these fields is very close to the “exact” traction field, however their magnitudes are different. Their departures from the applied traction field are quantified in Figure 4.4. In the no-noise case, the errors, when using the finite strain and infinitesimal strain models, are 4.5% and 14.76%, respectively (regularization parameter = 0.0001 and 1, respectively). The difference between the two is significant. For the 1% noise case, the corresponding errors are 18.66% and 27.23% (regularization parameter = 5 and 10, respectively), and the difference is around 9%. Once again we observe that the model error, that is the error associated with assuming an incorrect model in the inverse problem, is significant.

4.4.2 Neuronal cell model

As the second example, the geometry of a multi-polar neuronal cell is considered (see Figure 4.7a). Recently, there has been significant interest in understanding the traction exerted by these cells [253], [254]. The size of the neuronal cell is about $10 \mu\text{m} \times 10 \mu\text{m} \times 10 \mu\text{m}$, and it is contained within a cube of length $80 \mu\text{m}$. The unstructured mesh for this configuration consists of 54,587 elements with 10,673 vertices. Out of these, 6,971 are treated as tracked beads (that is the displacement at

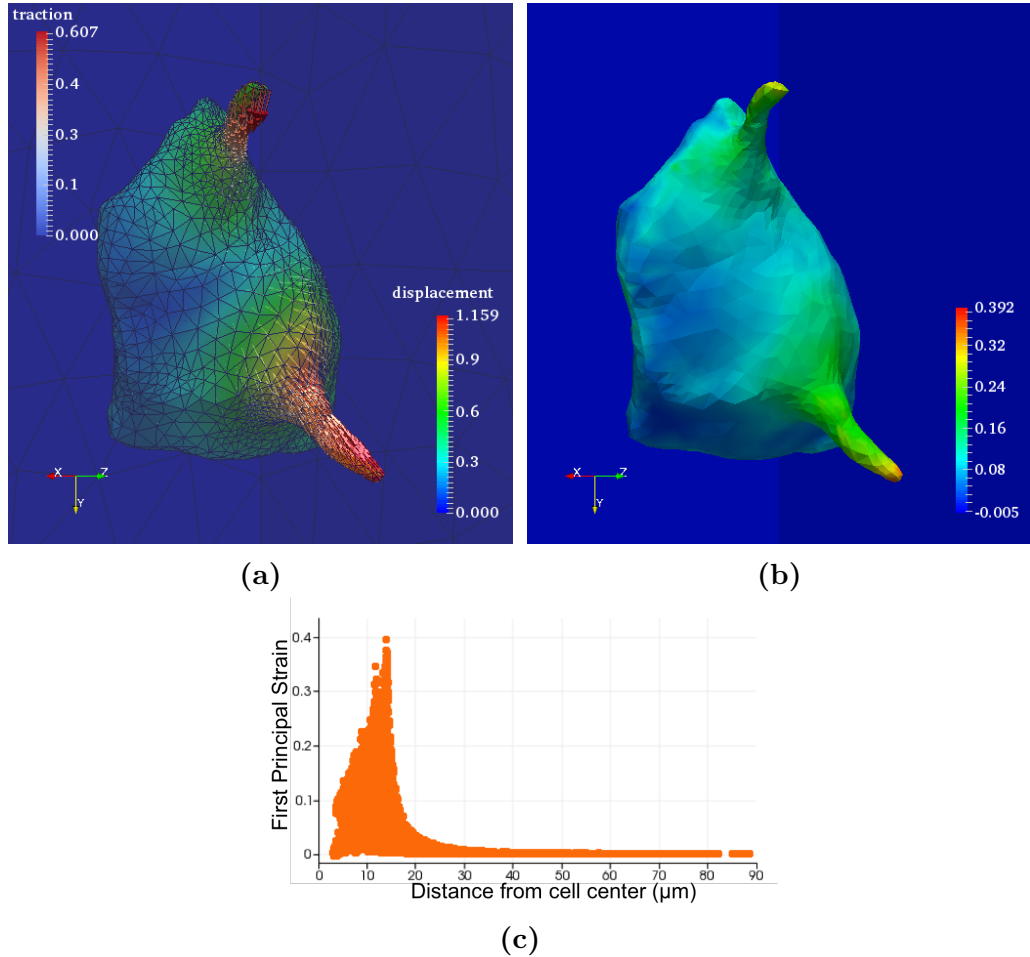


Figure 4.5: Results of the simulated forward problem for the microglial cell model on the deformed surface with $\gamma = 5$. (a) Arrows display the traction field (in kPa), and the deformed surface is colored by the displacement magnitude in μm . (b) The first principal component of the Green-Lagrange strain tensor. (c) Distribution of the strain at the bead locations as a function of distance from the center.

these locations are “measured”). These locations are selected so that they are close to the cell-matrix interface (but not on it). The shear modulus of the surrounding matrix is 400 Pa, and the nonlinear parameter is set to either 1 or 5. Five of the outer surfaces of the box are fixed in the x , y and z directions ($u_x = u_y = u_z = 0$), and the sixth surface is traction free, which is to mimic the free top surface of the matrix in experiments.

As shown in Figure 4.7b, the traction field is selected such that its magnitude

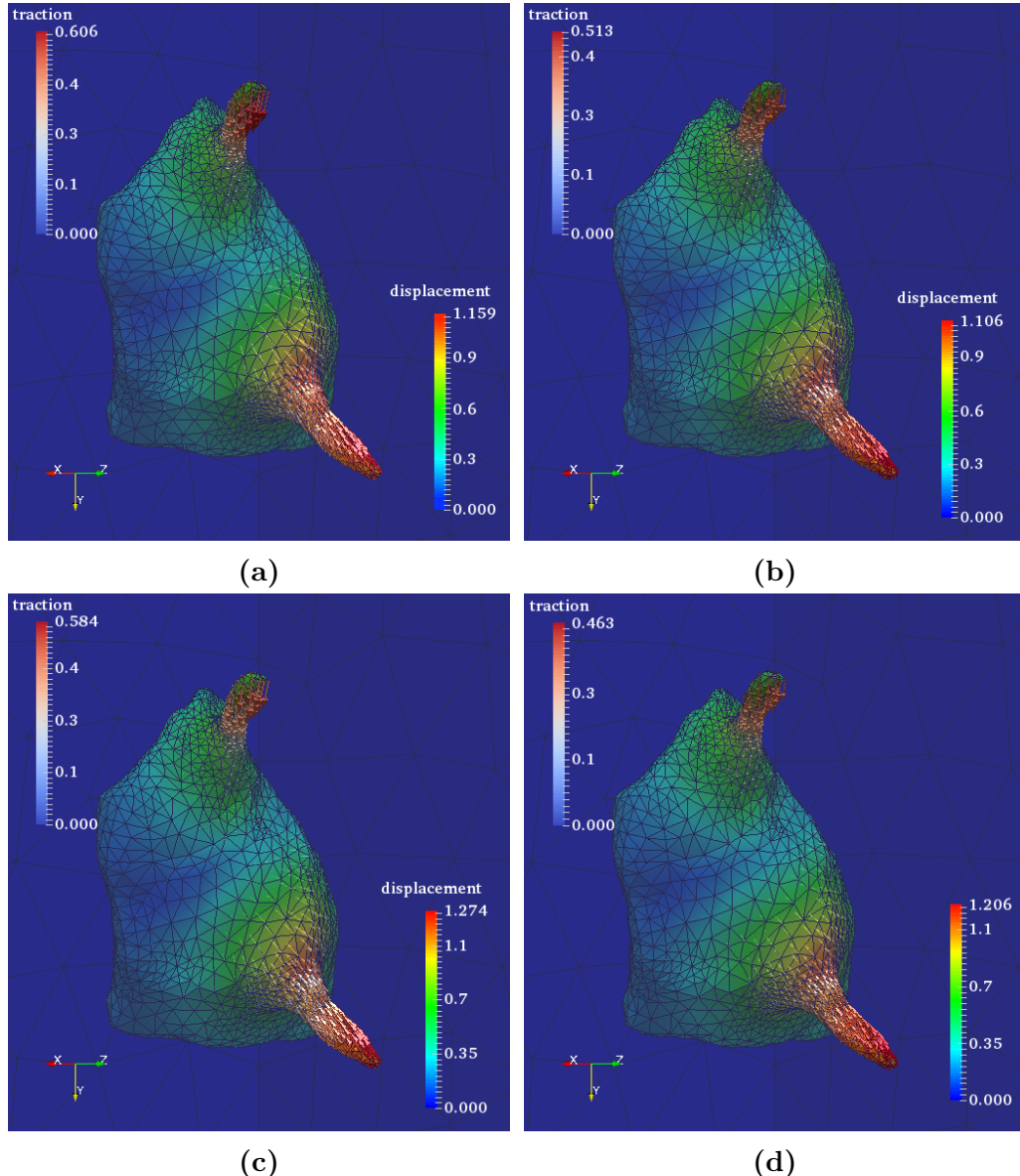


Figure 4.6: Results of the inverse analysis for the microglial cell on the deformed surface with $\gamma = 5$. Arrows display the recovered traction field (in kPa), and the deformed surface is colored by the recovered displacement magnitude in μm . (a) Solution with nonlinear effects and 0% noise. (b) Solution with nonlinear effects and 1% noise. (c) Solution without nonlinear effects and 0% noise. (d) Solution without nonlinear effects and 1% noise.

is largest along the arms of the cell and smoothly reduces towards the center. In addition, the traction vector is pointed inward toward the center of the cell. Similar

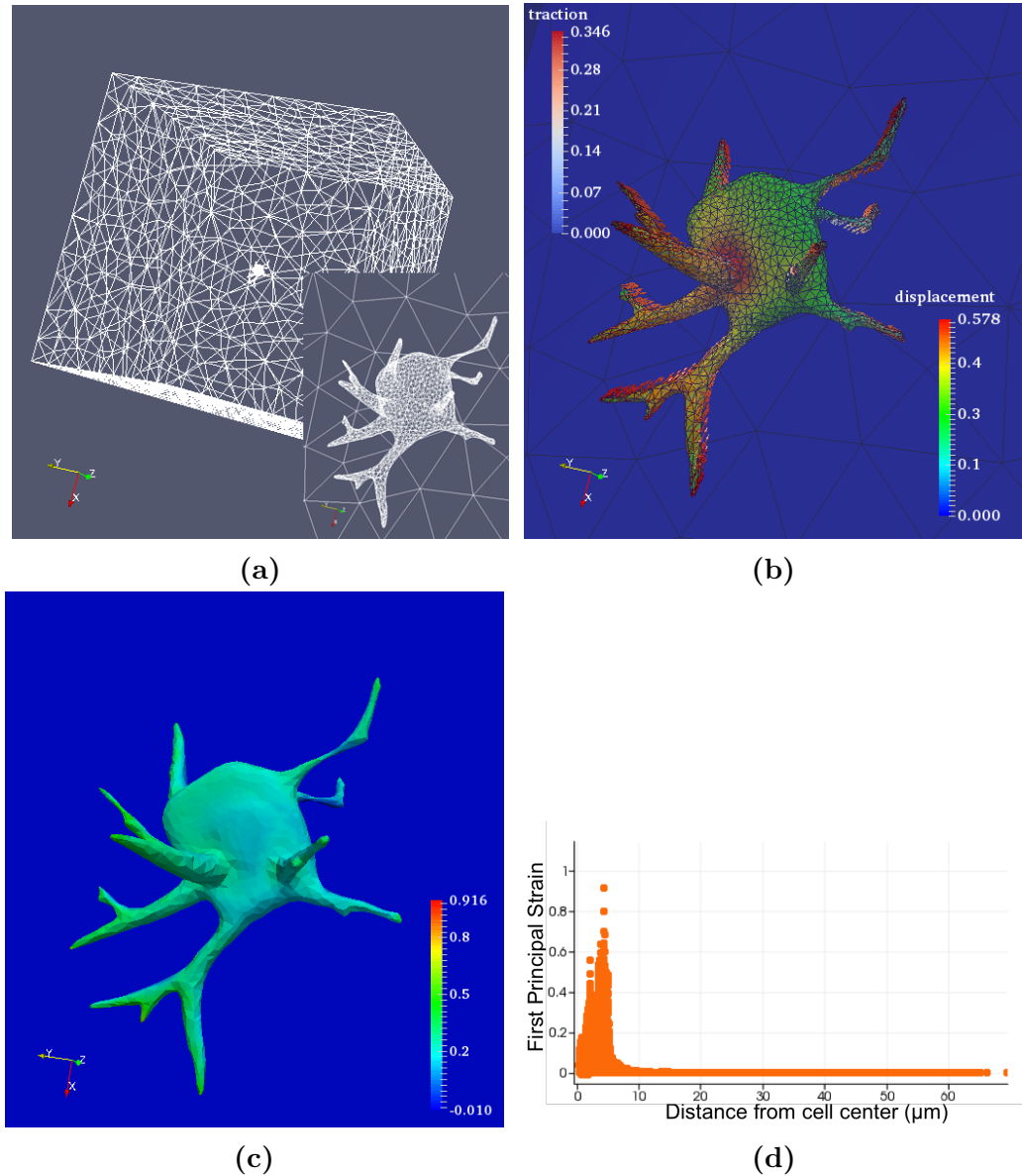


Figure 4.7: Neuronal cell: (a) Mesh on the exterior surface and the cell-matrix interface. Results of the simulated forward problem on the deformed surface with $\gamma = 1$. (b) Arrows display the traction field (in kPa), and the deformed surface is colored by the displacement magnitude in μm . (c) The first principal component of the Green-Lagrange strain tensor. (d) Distribution of the strain at the bead locations as a function of distance from the center.

to the first example, this loading condition also simulates the contraction of the matrix close to the cell after the cell is lysed with detergent [144].

Linear material ($\gamma = 1$)

In Figure 4.7c, we observe that the largest strain occurs at the dendritic ends of the cell, and pulls the dendrites toward the center of the cell body. Significant strains (50% to 90% along the dendrites) are generated at the cell-matrix surface, and are illustrated in Figure 4.7d, where we have plotted the first principal component of the Green-Lagrange strain tensor.

When solving the inverse problem, we use displacements with no noise and 1% noise, and then either use a finite strain or an infinitesimal strain model. The recovered traction vector fields appear similar, and are shown in Figure 4.8. However, their magnitudes are different. In Figure 4.9, we quantify this by evaluating the error ($e(\mathbf{h})$) in the traction field for each case. For “measured” displacement with no noise, this error is 0.5% for the finite strain model, and 16.93% for the infinitesimal strain model (regularization parameters = 1×10^{-7} and 0.1, respectively). For “measured” displacement with 1% noise, the error for the finite strain model grows to 26.41%, and that for the infinitesimal strain model is 34.78% (regularization parameters = 0.5 and 1, respectively). The difference between these errors is the penalty associated with invoking the infinitesimal strain assumption.

Nonlinear material ($\gamma = 5$)

The problem described above is repeated with the nonlinear parameter now set to 5. This means that the matrix now stiffens with increasing strain, and given that the traction field is unchanged, it strains less in response to the traction exerted by the cell. This can be seen by examining Figures 4.10a and 4.10b where we have plotted the displacement magnitude and the principal component of the Green-Lagrange strain tensor on the cell-matrix interface.

Once again displacement fields with no noise and with 1% noise are considered, and when solving the inverse problem, a finite strain model (with the appropriate nonlinear elastic response) and an infinitesimal strain model (with a linear elastic response) is used. This is done to quantify the effect of noise and modeling assumptions in solving the inverse problem. In all cases, we observe that the spatial distributions of the traction vector is recovered with remarkable accuracy (see Figure

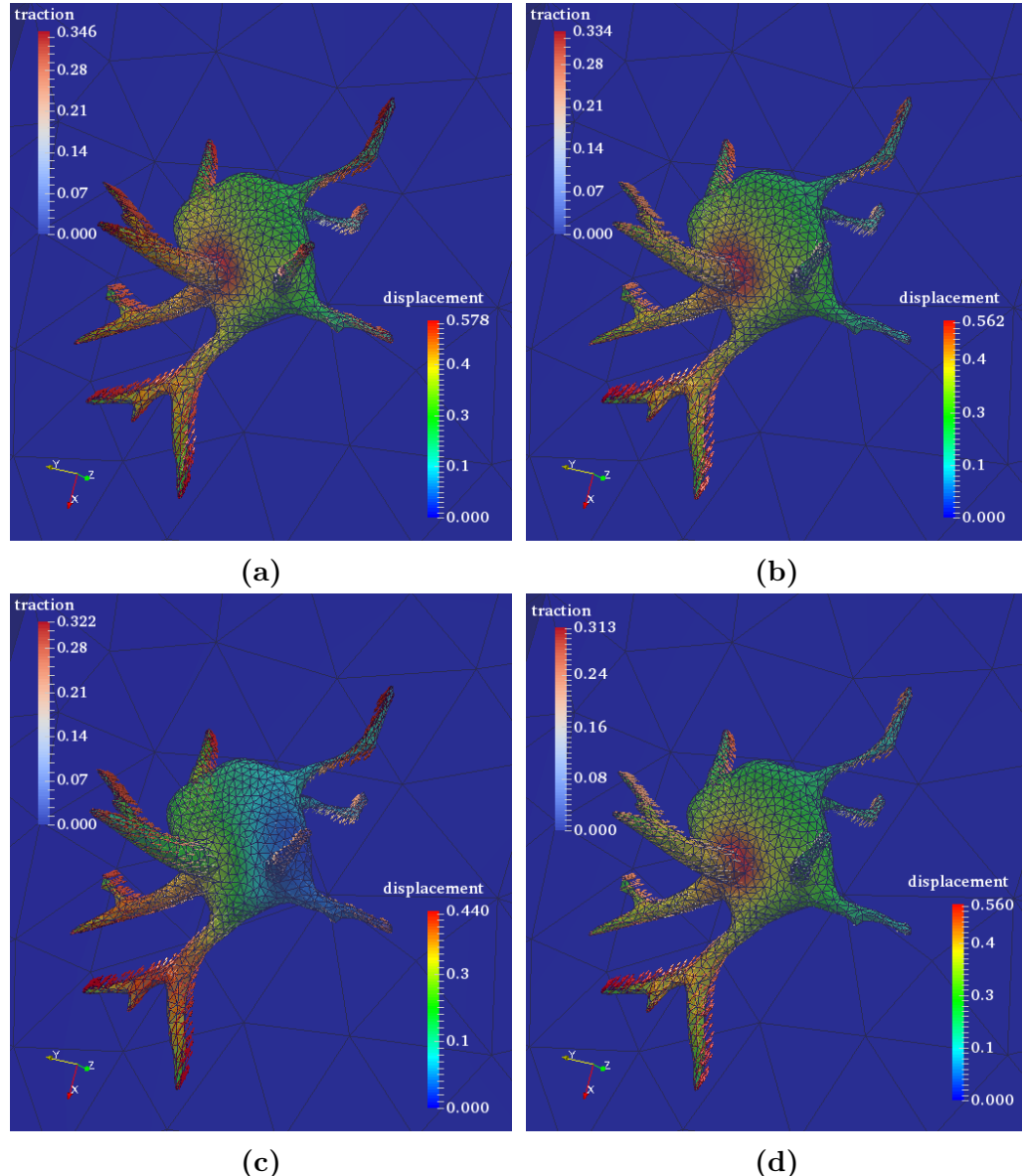


Figure 4.8: Results of the inverse analysis for the neuronal cell on the deformed surface with $\gamma = 1$. Arrows display the recovered traction field (in kPa), and the deformed surface is colored by the recovered displacement magnitude in μm . (a) Solution with nonlinear effects and 0% noise. (b) Solution with nonlinear effects and 1% noise. (c) Solution without nonlinear effects and 0% noise. (d) Solution without nonlinear effects and 1% noise.

4.11, regularization parameter = 1×10^{-7} , 0.5, 0.1 and 1, respectively). However, the magnitude of the traction, and consequently the error in the reconstruction (see

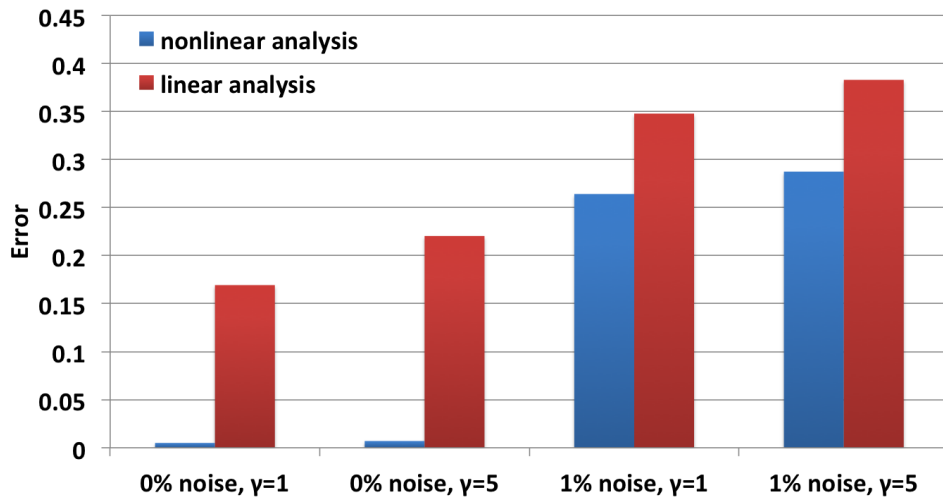


Figure 4.9: Error summary for the neuron cell model.

Figure 4.9), is sensitive to both displacement noise, and model selection. When there is no noise, the contribution of the model error is greater than 20%, and with 1% noise it drops to around 8%.

4.4.3 Discussion

We have selected the microglial and neuorn cells as examples because of their biomedical relevance, and also because of their distinct shapes. While the microglial cell has a relatively smooth shape with very few protrusions, the shape of the neuron is much more complicated with several dendritic structures. We note that in both cases our algorithm could be applied successfully. However, for the no-noise cases the tractions for the neuron cell were recovered with almost no error, whereas for the microglial cell they were recovered to around 4% error. There are several possible explanations for this difference. First, the magnitude of tractions applied to the microglial cell is about two times that of the tractions applied to the neuron, and in both cases the inverse problem begins with a zero initial guess. Consequently, for the microglial cell quasi-Newton algorithm has to cover a larger range in order to achieve the exact value. Also the dendritic shape of the neuron implies that there are many more local regions where the strains are large and these regions are sampled by the tracking beads. This could imply that the measured displacement field for the neuron carries a “stronger” imprint of the traction field making the

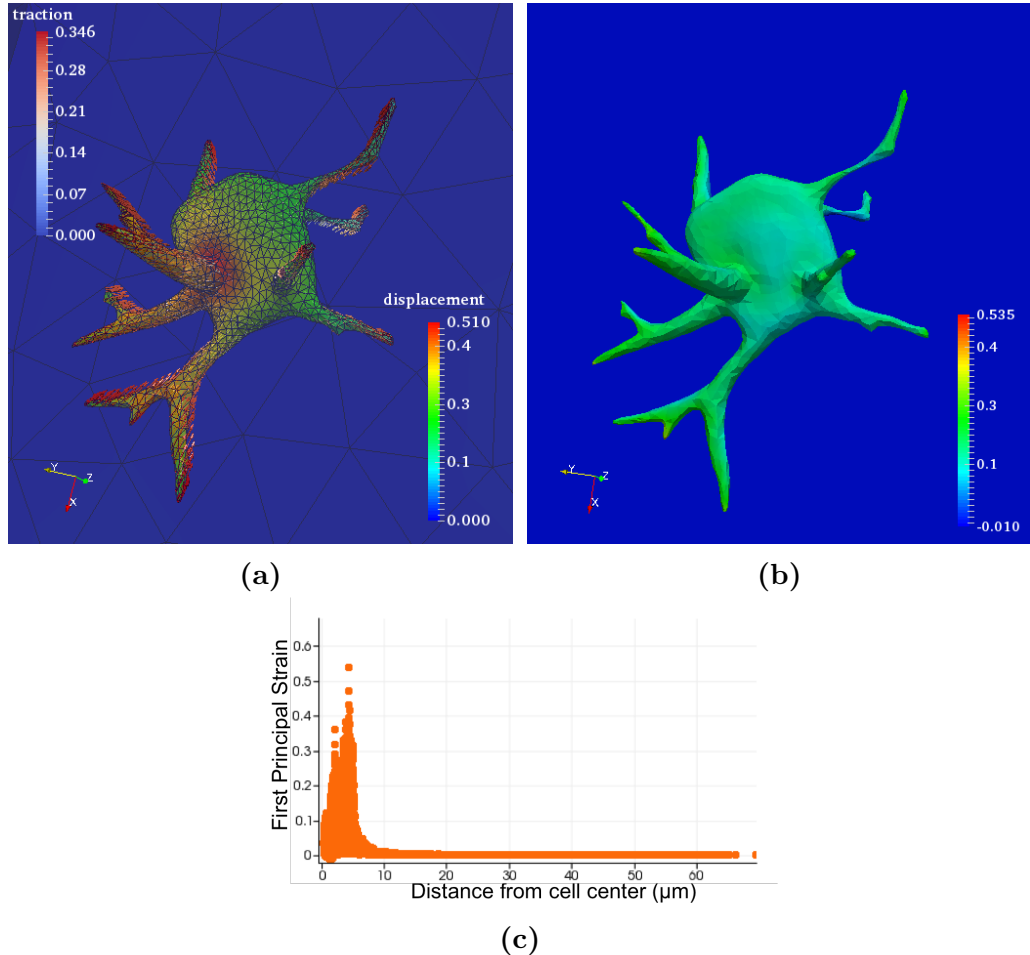


Figure 4.10: Results of the simulated forward problem for the neuronal cell model on the deformed surface with $\gamma = 5$. (a) Arrows display the traction field (in kPa), and the deformed surface is colored by the displacement magnitude in μm . (b) The first principal component of the Green-Lagrange strain tensor. (c) Distribution of the strain at the bead locations as a function of distance from the center.

inverse problem better posed.

In biomechanics applications, often the tractions measured are used to determine average quantities such as the contractile moment of the cell, or the net strain energy in the gel. We may conjecture how the proposed method would perform in evaluating these quantities. We note that the contractile moment is a linear functional of the traction field. Thus we would expect that error observed in this quantity would be similar to the error observed in the traction field. On the other

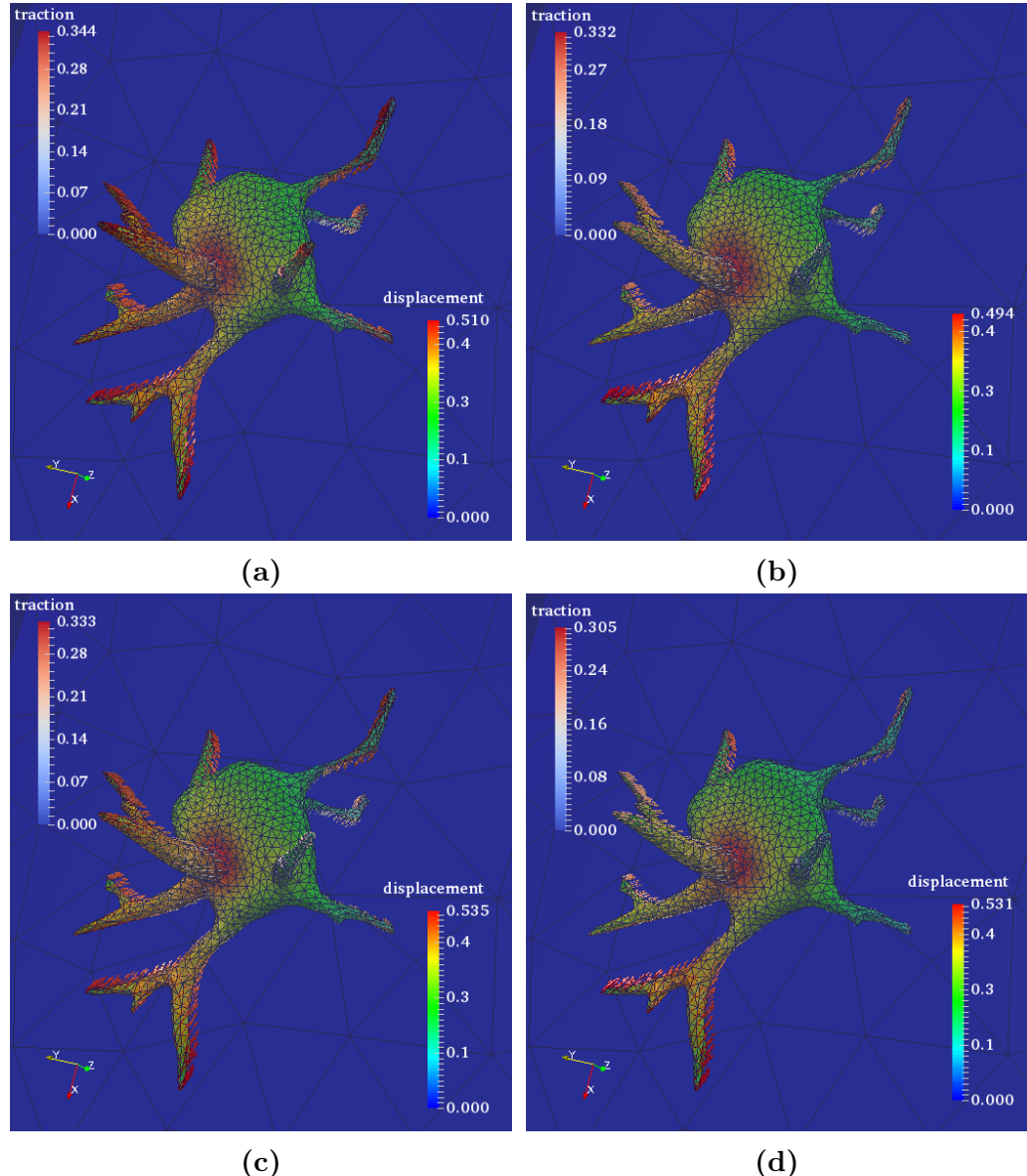


Figure 4.11: Results of the inverse analysis for the neuronal cell on the deformed surface with $\gamma = 5$. Arrows display the recovered traction field (in kPa), and the deformed surface is colored by the recovered displacement magnitude in μm . (a) Solution with nonlinear effects and 0% noise. (b) Solution with nonlinear effects and 1% noise. (c) Solution without nonlinear effects and 0% noise. (d) Solution without nonlinear effects and 1% noise.

hand, the strain energy in the gel may be evaluated by computing the work done by the cell on the gel. That is the integral $\int_{\Gamma} \mathbf{h} \cdot \mathbf{u} d\Gamma$. In this integral, \mathbf{h} is the

reconstructed traction field, and \mathbf{u} is the estimated displacement on the interface. It is reasonable to expect that if the recovered traction is underestimated by a certain fraction, then the recovered displacement will also be underestimated by the same factor. Then roughly speaking, the integral, which involves the product of these quantities, will be underestimated by two times this factor. In this case the importance of including nonlinear elastic effects will be even more significant.

4.5 Applications to experimental data

In this section, we apply the algorithm to the experimentally-measured data on human umbilical vein endothelial cells (HUVECs) cultured in hydrogels (data courtesy of Christopher Chen at Boston University). It is noted that only the results with linear elasticity are presented. The above-mentioned algorithm with nonlinear elasticity does not directly apply to this data, since the actual scenario poses some additionalaaulties that are discussed below.

4.5.1 Demonstration of feasibility with linear elasticity

There is a significant interest in the link between cell-generated forces and the mechanical properties of its micro-environment [23]–[28]. In this section, traction recovery with linear elasticity is applied to HUVECs in hydrogels with different stiffness. In [27], Baker *et al.* devised with innovative synthetic fibrillar materials to demonstrate that cells grow very differently in 3D fiber networks or collagen matrices from those on 2D hydrogels surfaces. It is thus valuable to measure cell-generated forces in 3D matrices. However, performing TFM on cells embedded in fiber networks and collagen matrices is computationally demanding due to their complicated 3D structures. Therefore, observing and computing tractions of cells in 3D hydrogels can be a first step. This section provides a preliminary study on how cells' traction vary with stiff and soft hydrogels. Since only two cases (one with stiff hydrogel and the other with soft hyogel) are presented, we do not intend to interpret the results in a more general sense biologically, but rather try to demonstrate the feasibility of our algorithm in solving actual problems.

The initial shear modulus (within linear regime) of the hydrogel is determined

experimentally with a rheometer-based test to be 780 Pa and 67 Pa for the stiff and soft hydrogels, respectively. Figures 4.12(a)(c) display the mesh for the hydrogel and the cell surface with dimensions of about $40\mu\text{m} \times 40\mu\text{m} \times 30\mu\text{m}$ for the stiff hydrogel case. Figure 4.12(b) shows the measured displacement field from the fluorescent beads. After employing the above-mentioned algorithm with linear elasticity, we are able to recover the traction field on the cell surface and the predicted displacement field on all mesh nodes. The recovered traction field and predicted displacement of the cell surface can be seen in Figure 4.12(d). Figure 4.12(e) shows the predicted displacement field of the fluorescent beads. The good agreement between the measured displacement in Figure 4.12(b) and the predicted displacement in Figure 4.12(e) demonstrates the ability method to match the measured data. In Figure 4.12(f), we have shown the largest eigenvalue associated with the Green-Lagrange strain on the surface of the cell. We observe in most locations this strain is upwards of 50%. Our algorithm works equally well for the soft hydrogel case and the results are shown in Figure 4.13. For both cases, iso2mesh developed by Fang *et al.* [255] is used for mesh generation and there are more than 100,000 tetrahedral elements and about 9,000 optimization variables, i.e. three times of the number of nodes on the cell surface. The mesh is generated by constraining vertices exactly on fluorescent beads, which avoids displacement field interpolation from beads to mesh vertices. One thing worth noting is that in Figure 4.13, the Green-Lagrange strain on most of the cell surface is well beyond 100 %. The huge strain in both cases implies the need of finite deformation theory. However, there are some challenges when applying our algorithm with nonlinear elasticity directly to these data. The challenges are elaborated in the following section.

4.5.2 Illustration of challenges in nonlinear elasticity

Large deformation

In Figure 4.13(d) and (f), the significant displacement and strain indicate the considerable deformation of cell. Although the deformation can be smaller considering nonlinear effects of the hydrogel, the deformation might still be too large to be handled without techniques such as re-meshing or the use of arbitrary Lagrangian

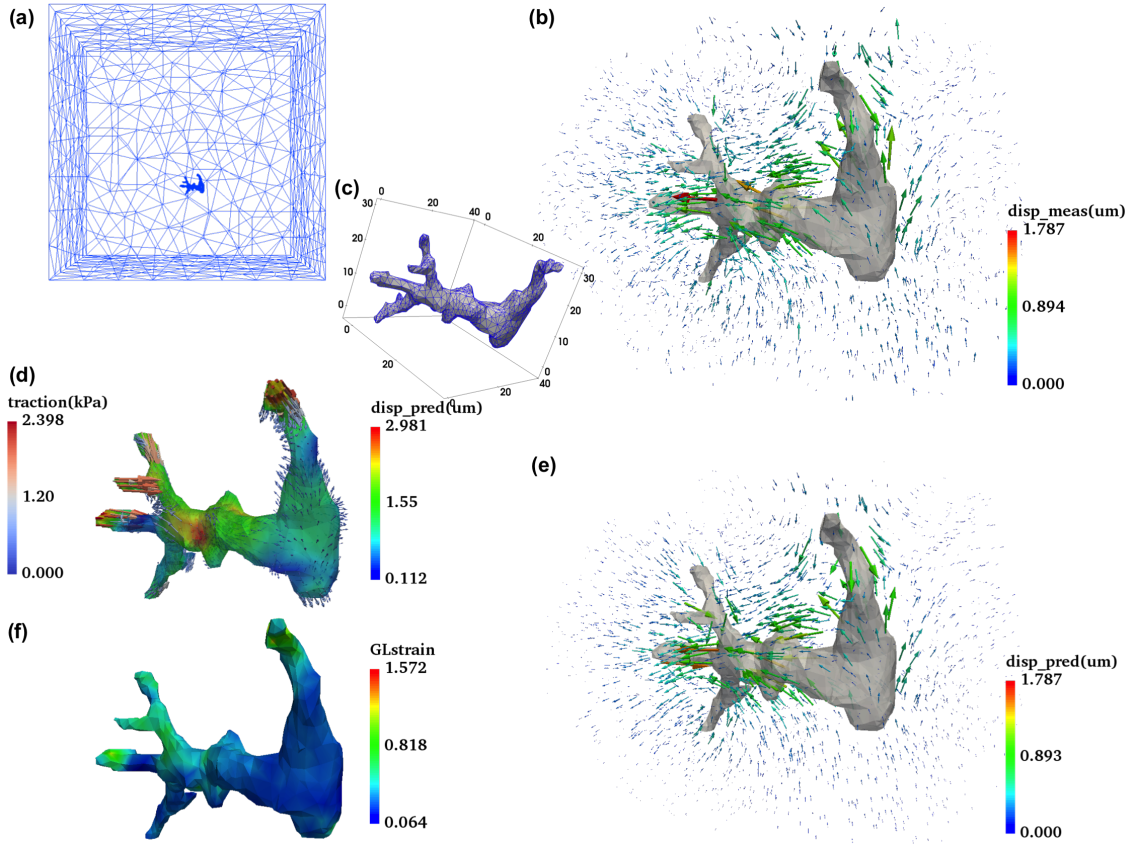


Figure 4.12: TFM with linear elasticity of a HUVEC in the stiff hydrogel ($\mu = 780 \text{ Pa}$). (a) and (c) display the mesh and dimensions. (b) and (e) display the measured and predicted displacement fields of the tracking beads. (d) shows the recovered tractions in arrows and predicted displacement of the cell surface shaded in rainbow colors. (f) shows the principal Green-Lagrange strain on the surface of the cell.

Eulerian (ALE) formulation. Both techniques can effectively solve the problem of over-distorted element in large deformation [256], [257]. The implementation of either of these is a significant step and will be considered as the next step of this research topic.

Unknown reference configuration

One fact that is easy to overlook, and yet is critical in the nonlinear case, is that in this study cell geometry extracted from the z-stack images of the confocal laser scanning microscopy (CLSM) is in the deformed configuration. Since in elasticity

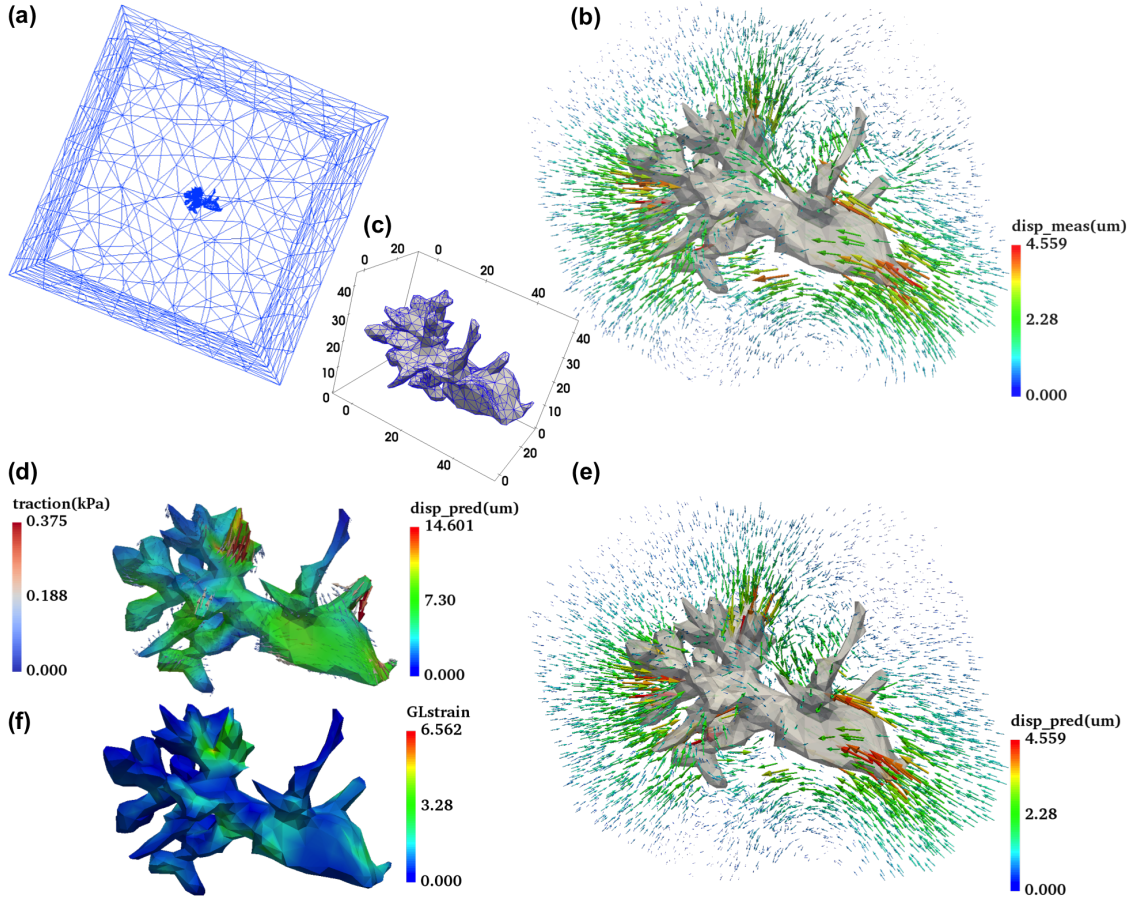


Figure 4.13: TFM with linear elasticity of a HUVEC in the soft hydrogel ($\mu = 67$ Pa). (a) and (c) display the mesh and dimensions. (b) and (e) display the measured and predicted displacement fields of the tracking beads. (d) shows the recovered tractions in arrows and predicted displacement of the cell surface shaded in rainbow colors. (f) shows the principal Green-Lagrange strain on the surface of the cell.

we typically deal with the undeformed shape in the stress-free state, our above-mentioned algorithm cannot be directly applied to the deformed shape. We also note the the undeformed cell geometry is not available because the cell surface loses fluorescence after lysing, which makes it cumbersome to extract the geometry from the z-stack images. Therefore, we are given the deformed configuration and seeking the reference configuration. The seminal work from Govindjee *et al.* shows the well-posedness of this problem and demonstrates examples in 2D for compressible and quasi-incompressible materials in finite deformation [258], [259]. We implemented

their algorithm but found out that the convergence is erratic. This could be due to the very complex geometry of the problem of interest, or the very large strains, or likely both of these factors. The extension of this approach to account for these factors is another interesting topic for future research.

4.6 Summary

Traction force microscopy is an important technique that is used to quantify tractions at the cell-matrix interface. It works by measuring the motion of embedded micro-beads in response to cellular tractions and using this information to infer the traction field. In this manuscript we have posed TFM as an inverse problem, and solved it using a constrained minimization algorithm. In doing so we have accounted for the three-dimensional nature of the problem, the complex geometry of the cell, and the finite-strain and nonlinear elastic behavior of the matrix. Through the use of a quasi-Newton algorithm, a carefully derived adjoint problem, and a novel continuation strategy, we have developed and implemented algorithms that efficiently utilize data from a large number of tracking beads ($\approx 10^4$) and reconstruct traction vectors on a well-resolved surface mesh ($\approx 10^3 - 10^4$ grid points).

We have applied these algorithms to *in-silico* problems with realistic geometric models of microglial and neuronal cells and conclude that the proposed algorithms are able to accurately recover the traction fields. We have also tested the effect of measurement noise on the proposed methods, and examined the error incurred by not including nonlinear effects when solving the TFM problem. We conclude that the error in the recovered traction field is sensitive to noise in the measured displacements, and to neglecting nonlinear effects in the TFM problem. We also demonstrate the feasibility of our algorithm by applying it to *in-vitro* problems with linear elasticity and explain the challenges about directly applying our algorithm to the *in-vitro* problems with nonlinear elasticity.

CHAPTER 5

Conclusions and Future Work

This thesis tackles two crucial aspects centered around biomechanics and mechanobiology - quantifying mechanical properties of tissues and evaluating tractions exerted by cells. Both problems are posed as PDE-constrained optimization problems given displacement fields measured by various imaging modalities, including optical coherence tomography (OCT) and confocal laser scanning microscopy (CLSM).

5.1 Conclusions

Since tissue mechanical properties are tightly related to the pathological development, quantifying these properties can provide complementary perspectives to conventional understanding, detection, diagnosis and therapeutic monitoring of diseases. We address this need by developing and applying a scheme that recovers the spatial distribution of soft tissue shear modulus with high spatial resolution. With displacement fields calculated from the OCT data and a mechanically well-defined calibration layer, the accurate spatial map of the specimens' shear modulus is recovered iteratively using an optimization-based strategy. To achieve the high resolution with reasonable computation resources, we utilize two distinct techniques - adaptive mesh refinement and domain decomposition. Through the former technique, mesh grids are refined in regions with high shear modulus gradients. Through the latter technique, multiple realizations of the original problem with distinct meshes are generated. Each realization has a fine well-resolved mesh in a small subdomain, and a coarse mesh everywhere else. These distinct realizations are then solved independently of each other with no communication between each solution. We validate our biomechanical imaging (BMI) scheme in 2D and 3D on tissue-mimicking phantoms of different stiffness, sizes and shapes against experimental data. Moreover, with our scheme, we are able to recover the three-dimensional spatial distribution of the shear modulus of one malignant breast tumor tissue *ex vivo* as well as to identify the regions of necrosis. We are also able to recover the mechanically distinct properties

of sweat glands in 3D by recovering the shear modulus distribution of fingertip tissue *in vivo*. In all cases, superior results are observed comparing to the widely used simplified methods where the stress is assumed constant either in all three directions or in the depth direction.

Cell-generated tractions are related to many critical biological processes, including stem cell differentiation and cancer cell metastasis. Cell traction force microscopy (TFM) provides an effective way to evaluate cell-generated tractions at the sub-cellular level. We propose an efficient adjoint-based inversion algorithm that infers the tractions exerted by a cell embedded in the three-dimensional extracellular matrix. Through *in-silico* data with real cell geometries, we validate the algorithm and quantify the error when linear elasticity is inappropriately assumed under large deformation. Furthermore, the applicability of the algorithm with linear elasticity is demonstrated on *in-vitro* data, human umbilical vein endothelial cells (HUVECs) in three-dimensional stiff and soft hydrogels. The challenges in directly applying our algorithm with nonlinear elasticity are explained.

5.2 Future work

From the successful applications of our BMI algorithm on data collected by ultrasound [11],[92],[114],[115] and OCT (Chapter 2 and 3), it is not hard to see that our algorithm is independent of imaging modalities. As long as the displacement field is given and the load is applied in a quasi-static manner, our algorithm is able to recover the shear modulus distribution of the specimen. Therefore, we are actively trying to apply our algorithm to data measured by different modalities, such as photoacoustic imaging, confocal microscopy and stimulated emission depletion (STED) microscopy. In these areas, BMI is not well explored yet.

With the high-resolution imaging modalities, it is possible to quantify how cell motion changes the stiffness of the micro-environment as well as to explore the relation between cell-generated forces and the mechanical properties of the micro-environment. However, as the resolution steps into subcellular level, assuming that the surrounding material is a homogeneous continuum can lead to incorrect inferences especially when the scale of the collagen fibers in extracellular matrices

becomes comparable with cell size. This requires more advanced simulation techniques such as using non-continuum material model, where fibers can be modeled as truss elements [260] or beam elements.

When compared with quasi-static BMI where the load needs to be applied very slowly, a less operator-dependent BMI option is to consider the dynamic case - transient BMI where the inertia term plays an important role. As noted in Section 1.2.2.2, solving the time-dependent PDE is a very challenging problem. Apart from using massively parallel computation codes, it is possible to solve the problem in Fourier domain at different frequencies, in which way only multiple Helmholtz equations need to be solved at different frequencies separately. In addition to that, due to the wave-like nature of the solutions to the time-dependent problem, using wavelet basis to compress the solution can be a possible way to tackle the challenge of very large memory requirements. Further, the need of modeling of the domain outside the region of interest can be tackled using techniques that do not require boundary conditions in solving the forward problem [261]. Since no boundary condition is needed, this idea can be further extended to parallelizing the solution of this problem with minimal communication.

As elaborated in Section 4.5.2, there are a couple of challenges that need to be overcome before our nonlinear elasticity TFM can be applied to experimental cell TFM data. According to literature, the challenge of large deformation can be solved with adaptive re-meshing or arbitrary Lagrangian Eulerian formulation [256], [257] and the challenge of unknown reference configuration can be solved with a inverse elastostatic formulation [258], [259]. These methods are to be carefully analyzed and implemented for the cell TFM problem.

In this thesis we have solved the BMI and the TFM problems using the same PDE-constrained optimization framework implemented in a single code - NonLinear Adjoint Coefficient Estimator (NLACE). The code is written in FORTRAN, parallelized with OpenMP on shared-memory machines and runs on Linux. As problems becomes larger, it will be necessary to parallelize NLACE on distributed-memory machines on high performance computers using MPI and OpenMP parallelization. A straightforward way to implement this is to use FEniCS - a popular computing

platform that can generate automated solution of differential equations by the finite element method [262]. Using libraries from FEniCS, parallelism and cross-platform performance are inherently taken care of. Ultimately, the hope is to develop a friendly toolkit that can be used at experimentalists' disposal with minimal interference from computational researchers.

Since both BMI and TFM deal with experimental data and all experimental data are more or less affected by noise, it is essential to supply results with different confidence level. This is especially so considering diseases diagnosis with BMI clinically. Rather than finding the probability distribution of the solution, computing the expectation and variance can be a first step. The topic related to this is uncertainty quantification (UQ).

REFERENCES

- [1] J. Eyckmans, T. Boudou, X. Yu, and C. S. Chen, “A hitchhiker’s guide to mechanobiology,” *Dev. Cell*, vol. 21, no. 1, pp. 35–47, Jun. 2011.
- [2] R. G. Barr, “Real-time ultrasound elasticity of the breast: initial clinical results,” *Ultrasound Q.*, vol. 26, no. 2, pp. 61–66, Jun. 2010.
- [3] W. A. Berg, L. Gutierrez, M. S. NessAiver, W. B. Carter, M. Bhargavan, R. S. Lewis *et al.*, “Diagnostic accuracy of mammography, clinical examination, US, and MR imaging in preoperative assessment of breast cancer,” *Radiology*, vol. 233, no. 3, pp. 830–849, Dec. 2004.
- [4] W. A. Berg, D. O. Cosgrove, C. J. Doré, F. K. Schäfer, W. E. Svensson, R. J. Hooley *et al.*, “Shear-wave elastography improves the specificity of breast US: the BE1 multinational study of 939 masses,” *Radiology*, vol. 262, no. 2, pp. 435–449, Feb. 2012.
- [5] J. M. Chang, W. K. Moon, N. Cho, A. Yi, H. R. Koo, W. Han *et al.*, “Clinical application of shear wave elastography (SWE) in the diagnosis of benign and malignant breast diseases,” *Breast Cancer Res. Treat.*, vol. 129, no. 1, pp. 89–97, Aug. 2011.
- [6] M. L. Palmeri, M. H. Wang, J. J. Dahl, K. D. Frinkley, and K. R. Nightingale, “Quantifying hepatic shear modulus in vivo using acoustic radiation force,” *Ultrasound Med. Biol.*, vol. 34, no. 4, pp. 546–558, Jan. 2008.
- [7] M. L. Palmeri, M. H. Wang, N. C. Rouze, M. F. Abdelmalek, C. D. Guy, B. Moser *et al.*, “Noninvasive evaluation of hepatic fibrosis using acoustic radiation force-based shear stiffness in patients with nonalcoholic fatty liver disease,” *J. Hepatol.*, vol. 55, no. 3, pp. 666–672, Sep. 2011.
- [8] W.-C. Yeh, P.-C. Li, Y.-M. Jeng, H.-C. Hsu, P.-L. Kuo, M.-L. Li *et al.*, “Elastic modulus measurements of human liver and correlation with pathology,” *Ultrasound Med. Biol.*, vol. 28, no. 4, pp. 467–474, Apr. 2002.
- [9] N. M. van Popele, D. E. Grobbee, M. L. Bots, R. Asmar, J. Topouchian, R. S. Reneman *et al.*, “Association between arterial stiffness and atherosclerosis,” *Stroke*, vol. 32, no. 2, pp. 454–460, Feb. 2001.
- [10] M. C. Murphy, J. Huston, III, C. R. Jack, K. J. Glaser, A. Manduca, J. P. Felmlee *et al.*, “Decreased brain stiffness in alzheimer’s disease determined

- by magnetic resonance elastography,” *J. Magn. Reson. Imaging*, vol. 34, no. 3, pp. 494–498, Jul. 2011.
- [11] S. Goenezen, J.-F. Dord, Z. Sink, P. E. Barbone, J. Jiang, T. J. Hall *et al.*, “Linear and nonlinear elastic modulus imaging: an application to breast cancer diagnosis,” *IEEE Trans. Med. Imaging*, vol. 31, no. 8, pp. 1628–1637, May 2012.
 - [12] T. A. Krouskop, T. M. Wheeler, F. Kallel, B. S. Garra, and T. Hall, “Elastic moduli of breast and prostate tissues under compression,” *Ultrasonic Imaging*, vol. 20, no. 4, pp. 260–274, Oct. 1998.
 - [13] J.-M. Correas, A.-M. Tissier, A. Khairoune, G. Khoury, D. Eiss, and O. Hélenon, “Ultrasound elastography of the prostate: state of the art,” *Diagn. Interv. Imaging*, vol. 94, no. 5, pp. 551–560, May, 2013.
 - [14] A. Chronopoulos, T. J. Lieberthal, and A. E. del Río Hernández, “Pancreatic cancer: a mechanobiology approach,” *Converg. Sci. Phys. Oncol.*, vol. 3, no. 1, Feb. 2017. [Online]. Available: <http://stacks.iop.org/2057-1739/3/i=1/a=013001> [Accessed: Jul. 15, 2017].
 - [15] N. Kawada and S. Tanaka, “Elastography for the pancreas: Current status and future perspective,” *World J. Gastroenterol.*, vol. 22, no. 14, pp. 3712–3724, Apr. 2016.
 - [16] S. J. Kirkpatrick, R. K. Wang, D. D. Duncan, M. Kulesz-Martin, and K. Lee, “Imaging the mechanical stiffness of skin lesions by in vivo acousto-optical elastography,” *Opt. Express*, vol. 14, no. 21, pp. 9770–9779, Oct. 2006.
 - [17] K.-J. Streitberger, M. Reiss-Zimmermann, F. B. Freimann, S. Bayerl, J. Guo, F. Arlt *et al.*, “High-resolution mechanical imaging of glioblastoma by multifrequency magnetic resonance elastography,” *PLoS One*, vol. 9, no. 10, Oct. 2014. [Online]. Available: <https://doi.org/10.1371/journal.pone.0110588> [Accessed: Jul. 15, 2017].
 - [18] C. L. de Korte, A. F. van der Steen, E. I. Céspedes, G. Pasterkamp, S. G. Carlier, F. Mastik *et al.*, “Characterization of plaque components and vulnerability with intravascular ultrasound elastography,” *Phys. Med. Biol.*, vol. 45, no. 6, pp. 1465–1475, Jun. 2000.
 - [19] E. Konofagou, T. Harrigan, and S. Solomon, “Assessment of regional myocardial strain using cardiac elastography: Distinguishing infarcted from non-infarcted myocardium,” in *2001 IEEE Ultrasonics Symposium*, Atlanta, GA, 2001, pp. 1589–1592.
 - [20] J.-L. Gennisson, S. Catheline, S. Chaffaï, and M. Fink, “Transient elastography in anisotropic medium: application to the measurement of slow

- and fast shear wave speeds in muscles,” *J. Acoust. Soc. Am.*, vol. 114, no. 1, pp. 536–541, Jul. 2003.
- [21] S. W. Shore, P. E. Barbone, A. A. Oberai, and E. F. Morgan, “Transversely isotropic elasticity imaging of cancellous bone,” *J. Biomech. Eng.*, vol. 133, no. 6, Jun. 2013. [Online]. Available: <https://doi.org/10.1115/1.4004231> [Accessed: Jul. 15, 2017].
 - [22] M. R. Ford, W. J. Dupps, A. M. Rollins, A. S. Roy, and Z. Hu, “Method for optical coherence elastography of the cornea” *J. Biomed. Opt.*, vol. 16, no. 1, Jan. 2011. [Online]. Available: <https://doi.org/10.1117/1.3526701> [Accessed: Jul. 15, 2017].
 - [23] T. Iskratsch, H. Wolfenson, and M. P. Sheetz, “Appreciating force and shape – the rise of mechanotransduction in cell biology,” *Nat. Rev. Mol. Cell Biol.*, vol. 15, no. 12, pp. 825–833, Oct. 2014.
 - [24] F. Kai, H. Laklai, and V. M. Weaver, “Force matters: biomechanical regulation of cell invasion and migration in disease,” *Trends Cell Biol.*, vol. 26, no. 7, pp. 486–497, Jul. 2016.
 - [25] T. Lecuit, P.-F. Lenne, and E. Munro, “Force generation, transmission, and integration during cell and tissue morphogenesis,” *Annu. Rev. Cell Dev. Biol.*, vol. 27, pp. 157–184, Nov. 2011.
 - [26] S. V. Plotnikov and C. M. Waterman, “Guiding cell migration by tugging,” *Curr. Opin. Cell Biol.*, vol. 25, no. 5, pp. 619–626, Oct. 2013.
 - [27] B. M. Baker, B. Trappmann, W. Y. Wang, M. S. Sakar, I. L. Kim, V. B. Shenoy *et al.*, “Cell-mediated fibre recruitment drives extracellular matrix mechanosensing in engineered fibrillar microenvironments,” *Nat. Mater.*, vol. 14, no. 12, pp. 1262–1268, Dec. 2015.
 - [28] S. Khetan, M. Guvendiren, W. R. Legant, D. M. Cohen, C. S. Chen, and J. A. Burdick, “Degradation-mediated cellular traction directs stem cell fate in covalently crosslinked three-dimensional hydrogels,” *Nat. Mater.*, vol. 12, no. 5, pp. 458–465, May 2013.
 - [29] T. Mammoto and D. E. Ingber, “Mechanical control of tissue and organ development,” *Development*, vol. 137, no. 9, pp. 1407–1420, Apr. 2010.
 - [30] O. Campàs, T. Mammoto, S. Hasso, R. A. Sperling, D. O’Connell, A. G. Bischof *et al.*, “Quantifying cell-generated mechanical forces within living embryonic tissues,” *Nat. Methods*, vol. 11, no. 2, pp. 183–189, Feb. 2014.
 - [31] A. J. Ewald, A. Brenot, M. Duong, B. S. Chan, and Z. Werb, “Collective epithelial migration and cell rearrangements drive mammary branching morphogenesis,” *Dev. Cell*, vol. 14, no. 4, pp. 570–581, Apr. 2008.

- [32] P. P. Provenzano, D. R. Inman, K. W. Eliceiri, J. G. Knittel, L. Yan, C. T. Rueden *et al.*, “Collagen density promotes mammary tumor initiation and progression,” *BMC Med.*, vol. 6, no. 1, Apr. 2008. [Online]. Available: <https://doi.org/10.1186/1741-7015-6-11> [Accessed: Jul. 15, 2017].
- [33] L. Kass, J. T. Erler, M. Dembo, and V. M. Weaver, “Mammary epithelial cell: influence of extracellular matrix composition and organization during development and tumorigenesis,” *Int. J. Biochem. Cell Biol.*, vol. 39, no. 11, pp. 1987–1994, Nov. 2007.
- [34] K. R. Levental, H. Yu, L. Kass, J. N. Lakins, M. Egeblad, J. T. Erler *et al.*, “Matrix crosslinking forces tumor progression by enhancing integrin signaling,” *Cell*, vol. 139, no. 5, pp. 891–906, Nov. 2009.
- [35] J. Ophir, I. Cespedes, H. Ponnekanti, Y. Yazdi, and X. Li, “Elastography: a quantitative method for imaging the elasticity of biological tissues,” *Ultrason Imaging*, vol. 13, no. 2, pp. 111–134, Apr. 1991.
- [36] L. Gao, K. Parker, R. Lerner, and S. Levinson, “Imaging of the elastic properties of tissuea review,” *Ultrasound Med. Biol.*, vol. 22, no. 8, pp. 959–977, Apr. 1996.
- [37] J. Ophir, S. Alam, B. Garra, F. Kallel, E. Konofagou, T. Krouskop *et al.*, “Elastography: ultrasonic estimation and imaging of the elastic properties of tissues,” *Proc. Inst. Mech. Eng. H*, vol. 213, no. 3, pp. 203–233, Mar. 1999.
- [38] K. J. Parker, L. S. Taylor, S. Gracewski, and D. J. Rubens, “A unified view of imaging the elastic properties of tissue,” *J. Acoust. Soc. Am.*, vol. 117, no. 5, pp. 2705–2712, May. 2005.
- [39] P. E. Barbone and A. A. Oberai, “A review of the mathematical and computational foundations of biomechanical imaging,” in *Computational Modeling in Biomechanics*, S. De, F. Guilak, R. K. M. Mofrad, Eds., Dordrecht, Netherlands: Springer, 2010, pp. 375–408.
- [40] M. Doyley, “Model-based elastography: a survey of approaches to the inverse elasticity problem,” *Phys. Med. Biol.*, vol. 57, no. 3, pp. R35–R73, Feb. 2012.
- [41] Y. K. Mariappan, K. J. Glaser, and R. L. Ehman, “Magnetic resonance elastography: a review,” *Clin. Anat.*, vol. 23, no. 5, pp. 497–511, Jul. 2010.
- [42] V. Egorov and A. P. Sarvazyan, “Mechanical imaging of the breast,” *IEEE Trans. Med. Imaging*, vol. 27, no. 9, pp. 1275–1287, Sep. 2008.
- [43] V. Egorov, T. Kearney, S. B. Pollak, C. Rohatgi, N. Sarvazyan, S. Airapetian *et al.*, “Differentiation of benign and malignant breast lesions by mechanical imaging,” *Breast Cancer Res. Treat.*, vol. 118, no. 1, pp. 67–80, Nov. 2009.

- [44] V. Egorov, S. Tsyuryupa, S. Kanilo, M. Kogit, and A. Sarvazyan, “Soft tissue elastometer,” *Med. Eng. Phys.*, vol. 30, no. 2, pp. 206–212, Mar. 2008.
- [45] Y. Mei, R. Fulmer, V. Raja, S. Wang, and S. Goenezen, “Estimating the non-homogeneous elastic modulus distribution from surface deformations,” *Int. J. Solids Struct.*, vol. 83, pp. 73–80, Apr. 2016.
- [46] L. G. Olson and R. D. Throne, “An inverse problem approach to stiffness mapping for early detection of breast cancer,” *Inverse Probl. Sci. Eng.*, vol. 21, no. 2, pp. 314–338, Mar. 2013.
- [47] J. Jiang and T. Hall, “A parallelizable real-time motion tracking algorithm with applications to ultrasonic strain imaging,” *Phys. Med. Biol.*, vol. 52, no. 13, pp. 3773–3790, Jul. 2007.
- [48] H. Rivaz, E. Boctor, P. Foroughi, R. Zellars, G. Fichtinger, and G. Hager, “Ultrasound elastography: a dynamic programming approach,” *IEEE Trans. Med. Imaging*, vol. 27, no. 10, pp. 1373–1377, Oct. 2008.
- [49] J. Jiang and T. J. Hall, “A generalized speckle tracking algorithm for ultrasonic strain imaging using dynamic programming,” *Ultrasound Med. Biol.*, vol. 35, no. 11, pp. 1863–1879, Nov. 2009.
- [50] L. Chen, G. M. Treece, J. E. Lindop, A. H. Gee, and R. W. Prager, “A quality-guided displacement tracking algorithm for ultrasonic elasticity imaging,” *Med. Image Anal.*, vol. 13, no. 2, pp. 286–296, Apr. 2009.
- [51] J. Luo and E. E. Konofagou, “A fast normalized cross-correlation calculation method for motion estimation,” *IEEE Trans. Ultrason. Ferroelectr. Freq. Control*, vol. 57, no. 6, pp. 1347–1357, Jun. 2010.
- [52] H. Rivaz, E. M. Boctor, M. A. Choti, and G. D. Hager, “Real-time regularized ultrasound elastography,” *IEEE Trans. Med. Imaging*, vol. 30, no. 4, pp. 928–945, Apr. 2011.
- [53] B. F. Kennedy, K. M. Kennedy, and D. D. Sampson, “A review of optical coherence elastography: fundamentals, techniques and prospects,” *IEEE J. Sel. Top. Quantum Electron.*, vol. 20, no. 2, pp. 272–288, Mar. 2014.
- [54] K. V. Larin and D. D. Sampson, “Optical coherence elastography–OCT at work in tissue biomechanics,” *Biomed. Opt. Express*, vol. 8, no. 2, pp. 1172–1202, Jan. 2017.
- [55] E. S. Burnside, T. J. Hall, A. M. Sommer, G. K. Hesley, G. A. Sisney, W. E. Svensson *et al.*, “Differentiating benign from malignant solid breast masses with us strain imaging,” *Radiology*, vol. 245, no. 2, pp. 401–410, Nov. 2007.

- [56] B. F. Kennedy, S. H. Koh, R. A. McLaughlin, K. M. Kennedy, P. R. Munro, and D. D. Sampson, “Strain estimation in phase-sensitive optical coherence elastography,” *Biomed. Opt. Express*, vol. 3, no. 8, pp. 1865–1879, Aug. 2012.
- [57] B. F. Kennedy, R. A. McLaughlin, K. M. Kennedy, L. Chin, A. Curatolo, A. Tien *et al.*, “Optical coherence micro-elastography: mechanical-contrast imaging of tissue microstructure,” *Biomed. Opt. Express*, vol. 5, no. 7, pp. 2113–2124, Jun. 2014.
- [58] L. Guo, Y. Xu, Z. Xu, and J. Jiang, “A PDE-based regularization algorithm toward reducing speckle tracking noise: A feasibility study for ultrasound breast elastography,” *Ultrason. Imaging*, vol. 37, no. 4, pp. 277–293, Oct. 2015.
- [59] A. P. Sarvazyan, O. V. Rudenko, S. D. Swanson, J. B. Fowlkes, and S. Y. Emelianov, “Shear wave elasticity imaging: a new ultrasonic technology of medical diagnostics,” *Ultrasound Med. Biol.*, vol. 24, no. 9, pp. 1419–1435, Nov. 1998.
- [60] S. Wang, J. Li, R. K. Manapuram, F. M. Menodiado, D. R. Ingram, M. D. Twa *et al.*, “Noncontact measurement of elasticity for the detection of soft-tissue tumors using phase-sensitive optical coherence tomography combined with a focused air-puff system,” *Opt. Lett.*, vol. 37, no. 24, pp. 5184–5186, Dec. 2012.
- [61] C. Li, Z. Huang, and R. K. Wang, “Elastic properties of soft tissue-mimicking phantoms assessed by combined use of laser ultrasonics and low coherence interferometry,” *Opt. Express*, vol. 19, no. 11, pp. 10153–10163, May 2011.
- [62] C. Li, G. Guan, Z. Huang, M. Johnstone, and R. Wang, “Noncontact all-optical measurement of corneal elasticity,” *Opt. Lett.*, vol. 37, no. 10, pp. 1625–1627, May 2012.
- [63] P. McCracken, A. Manduca, J. P. Felmlee, and R. L. Ehman, “Transient mr elastography: modeling traumatic brain injury,” in *International Conference on Medical Image Computing and Computer-Assisted Intervention*, Rennes, France, 2004, pp. 1081–1082.
- [64] K. Parker, S. Huang, R. Musulin, and R. Lerner, “Tissue response to mechanical vibrations for “sonoelasticity imaging”,” *Ultrasound Med. Biol.*, vol. 16, no. 3, pp. 241–246, 1990.
- [65] A. L. Oldenburg, G. Wu, D. Spivak, F. Tsui, A. S. Wolberg, and T. H. Fischer, “Imaging and elastometry of blood clots using magnetomotive optical coherence tomography and labeled platelets,” *IEEE J. Sel. Top. Quantum Electron.*, vol. 18, no. 3, pp. 1100–1109, Jul. 2012.

- [66] R. Muthupillai, D. Lomas, P. Rossman, J. F. Greenleaf, A. Manduca, and R. L. Ehman, “Magnetic resonance elastography by direct visualization of propagating acoustic strain waves,” *Science*, vol. 269, no. 5232, pp. 1854–1857, Sep. 1995.
- [67] J. Fowlkes, S. Emelianov, J. Pipe, A. Skovoroda, P. Carson, R. Adler *et al.*, “Magnetic-resonance imaging techniques for detection of elasticity variation,” *Med. Phys.*, vol. 22, no. 11, pp. 1771–1778, Nov. 1995.
- [68] K. M. Kennedy, L. Chin, R. A. McLaughlin, B. Latham, C. M. Saunders, D. D. Sampson *et al.*, “Quantitative micro-elastography: imaging of tissue elasticity using compression optical coherence elastography,” *Sci. Rep.*, vol. 5, Oct. 2015. [Online]. Available: <https://doi.org/10.1038/srep15538> [Accessed: Jul. 15, 2017].
- [69] L. Dong, P. Wijesinghe, J. T. Dantuono, D. D. Sampson, P. R. T. Munro, B. F. Kennedy *et al.*, “Quantitative compression optical coherence elastography as an inverse elasticity problem,” *IEEE J. Sel. Top. Quantum Electron.*, vol. 22, no. 3, pp. 277–287, May–Jun. 2016.
- [70] T. van Leeuwen and F. J. Herrmann, “3D frequency-domain seismic inversion with controlled sloppiness,” *SIAM J. Sci. Comput.*, vol. 36, no. 5, pp. S192–S217, Oct. 2014.
- [71] M. Stoll and A. Wathen, “All-at-once solution of time-dependent stokes control,” *J. Comput. Phys.*, vol. 232, no. 1, pp. 498–515, Jan. 2013.
- [72] A. Griewank and A. Walther, “Algorithm 799: Revolve: An implementation of checkpointing for the reverse or adjoint mode of computational differentiation,” *ACM Trans. Math. Softw.*, vol. 26, no. 1, pp. 19–45, Mar. 2000.
- [73] M. Bayat, S. Ghosh, A. Alizad, W. Aquino, and M. Fatemi, “A generalized reconstruction framework for transient elastography,” *J. Acoust. Soc. Am.*, vol. 139, no. 4, pp. 2028–2028, Apr. 2016.
- [74] M. Bonnet and W. Aquino, “Three-dimensional transient elastodynamic inversion using an error in constitutive relation functional,” *Inverse Probl.*, vol. 31, no. 3, Feb. 2015. [Online]. Available: <http://stacks.iop.org/0266-5611/31/i=3/a=035010> [Accessed: Jul. 15, 2017].
- [75] A. T. Barker and M. Stoll, “Domain decomposition in time for pde-constrained optimization,” *Comput. Phys. Commun.*, vol. 197, pp. 136–143, Dec. 2015.
- [76] M. Stoll, “Fast iterative solvers for time dependent pde-constrained optimization problems,” Ph.D. dissertation, Max Planck Inst. Magdeburg,

Otto-von-Guericke Univ. Magdeburg, Magdeburg, Saxony-Anhalt, Germany, 2016.

- [77] J. Virieux and S. Operto, “An overview of full-waveform inversion in exploration geophysics,” *Geophysics*, vol. 74, no. 6, pp. WCC1–WCC26, Nov. 2009.
- [78] M. A. Aguiló, W. Aquino, J. C. Brigham, and M. Fatemi, “An inverse problem approach for elasticity imaging through vibroacoustics,” *IEEE Trans. Med. Imaging*, vol. 29, no. 4, pp. 1012–1021, Apr. 2010.
- [79] R. Sinkus, J. Lorenzen, D. Schrader, M. Lorenzen, M. Dargatz, and D. Holz, “High-resolution tensor mr elastography for breast tumour detection,” *Phys. Med. Biol.*, vol. 45, no. 6, pp. 1649–1664, Jun. 2000.
- [80] R. Sinkus, M. Tanter, T. Xydeas, S. Catheline, J. Bercoff, and M. Fink, “Viscoelastic shear properties of in vivo breast lesions measured by MR elastography,” *Magn. Reson. Imaging*, vol. 23, no. 2, pp. 159–165, Feb. 2005.
- [81] T. E. Oliphant, A. Manduca, R. L. Ehman, and J. F. Greenleaf, “Complex-valued stiffness reconstruction for magnetic resonance elastography by algebraic inversion of the differential equation,” *Magn. Reson. Med.*, vol. 45, no. 2, pp. 299–310, Feb. 2001.
- [82] J. McLaughlin, D. Renzi, J.-R. Yoon, R. L. Ehman, and A. Manduca, “Variance controlled shear stiffness images for MRE data,” in *3rd IEEE International Symposium on Biomedical Imaging: Nano to Macro*, Arlington, VA, 2006, pp. 960–963.
- [83] J. R. McLaughlin, N. Zhang, and A. Manduca, “Calculating tissue shear modulus and pressure by 2D log-elastographic methods,” *Inverse Probl.*, vol. 26, no. 8, Jun. 2010. [Online]. Available: <http://stacks.iop.org/0266-5611/26/i=8/a=085007> [Accessed: Jul. 15, 2017].
- [84] K. Lin, J. R. McLaughlin, A. Thomas, K. Parker, B. Castaneda, and D. J. Rubens, “Two-dimensional shear wave speed and crawling wave speed recoveries from in vitro prostate data,” *J. Acoust. Soc. Am.*, vol. 130, no. 1, pp. 585–598, Jul. 2011.
- [85] Y. Zhang, A. A. Oberai, P. E. Barbone, and I. Harari, “Solution of the time-harmonic viscoelastic inverse problem with interior data in two dimensions,” *Int. J. Numer. Meth. Eng.*, vol. 92, no. 13, pp. 1100–1116, Dec. 2012.
- [86] Y. Zhang, P. E. Barbone, I. Harari, and A. A. Oberai, “Uniqueness of the interior plane strain time-harmonic viscoelastic inverse problem,” *J. Mech. Phys. Solids*, vol. 92, pp. 345–355, Jul. 2016.

- [87] A. Skovoroda, S. Emelianov, and M. O'Donnell, "Tissue elasticity reconstruction based on ultrasonic displacement and strain images," *IEEE Trans. Ultrason. Ferroelectr. Freq. Control*, vol. 42, no. 4, pp. 747–765, Jul. 1995.
- [88] C. Sumi, "Spatially variant regularization for tissue strain measurement and shear modulus reconstruction," *J. Med. Ultrason.*, vol. 34, no. 3, pp. 125–131, Sep. 2007.
- [89] M. Doyley, P. Meaney, and J. Bamber, "Evaluation of an iterative reconstruction method for quantitative elastography," *Phys. Med. Biol.*, vol. 45, no. 6, pp. 1521–1540, 2000.
- [90] J. Jiang, T. Varghese, C. L. Brace, E. L. Madsen, T. J. Hall, S. Bharat *et al.*, "Young's modulus reconstruction for radio-frequency ablation electrode-induced displacement fields: a feasibility study," *IEEE Trans. Med. Imaging*, vol. 28, no. 8, pp. 1325–1334, Aug. 2009.
- [91] A. A. Oberai, N. H. Gokhale, M. M. Doyley, and J. C. Bamber, "Evaluation of the adjoint equation based algorithm for elasticity imaging," *Phys. Med. Biol.*, vol. 49, no. 13, pp. 2955–2974, Jul. 2004.
- [92] A. A. Oberai, N. H. Gokhale, S. Goenezen, P. E. Barbone, T. J. Hall, A. M. Sommer *et al.*, "Linear and nonlinear elasticity imaging of soft tissue in vivo: demonstration of feasibility," *Phys. Med. Biol.*, vol. 54, no. 5, pp. 1191–1207, 2009.
- [93] J. Bishop, A. Samani, J. Sciarretta, and D. B. Plewes, "Two-dimensional MR elastography with linear inversion reconstruction: methodology and noise analysis," *Phys. Med. Biol.*, vol. 45, no. 8, pp. 2081–2091, Aug. 2000.
- [94] K. Raghavan and A. E. Yagle, "Forward and inverse problems in elasticity imaging of soft tissues," *IEEE Trans. Nucl. Sci.*, vol. 41, no. 4, pp. 1639–1648, Aug. 1994.
- [95] P. E. Barbone, C. E. Rivas, I. Harari, U. Albocher, A. A. Oberai, and Y. Zhang, "Adjoint-weighted variational formulation for the direct solution of inverse problems of general linear elasticity with full interior data," *Int. J. Numer. Meth. Eng.*, vol. 81, no. 13, pp. 1713–1736, Mar. 2010.
- [96] M. I. Miga, "A new approach to elastography using mutual information and finite elements," *Phys. Med. Biol.*, vol. 48, no. 4, pp. 467–480, Feb. 2003.
- [97] Y. Zhang, L. O. Hall, D. B. Goldgof, and S. Sarkar, "A constrained genetic approach for computing material property of elastic objects," *IEEE Trans. Evolut. Comput.*, vol. 10, no. 3, pp. 341–357, Jun. 2006.

- [98] A. A. Oberai, N. H. Gokhale, and G. R. Feijóo, “Solution of inverse problems in elasticity imaging using the adjoint method,” *Inverse Probl.*, vol. 19, no. 2, pp. 297–313, Feb. 2003.
- [99] L. Dong and A. A. Oberai, “Recovery of cellular traction in three-dimensional nonlinear hyperelastic matrices,” *Comput. Methods Appl. Mech. Eng.*, vol. 314, pp. 296–313, Feb. 2017.
- [100] Y. Le Cun, “A theoretical framework for back-propagation,” in *Proc. 1988 Connectionist Models Summer School*, Burlington, MA: Morgan Kaufmann, pp. 21–28.
- [101] A. McNamara, A. Treuille, Z. Popović, and J. Stam, “Fluid control using the adjoint method,” *ACM Trans. Graph.*, vol. 23, no. 3, pp. 449–456, Aug. 2004.
- [102] M. Nemec, M. Aftosmis, and M. Wintzer, “Adjoint-based adaptive mesh refinement for complex geometries,” in *46th AIAA Aerospace Sciences Meeting and Exhibit*, Reno, NV, Jan. 2008, pp. 725.1–725.23.
- [103] J. Worthen, G. Stadler, N. Petra, M. Gurnis, and O. Ghattas, “Towards adjoint-based inversion for rheological parameters in nonlinear viscous mantle flow,” *Phys. Earth Planet. Inter.*, vol. 234, pp. 23–34, Sep. 2014.
- [104] A. Jameson, “Aerodynamic shape optimization using the adjoint method,” Feb. 2003. [Online]. Available: <http://aero-comlab.stanford.edu/Papers/jameson.vki03.pdf> [Accessed: Jun. 15, 2017].
- [105] J. E. Hicken, “Efficient algorithms for future aircraft design: Contributions to aerodynamic shape optimization,” Ph.D. dissertation, Dept. Aero. Sci. Eng., Univ. Toronto, Toronto, ON, Canada, 2009.
- [106] K. A. James and H. Waisman, “Topology optimization of viscoelastic structures using a time-dependent adjoint method,” *Comput. Methods Appl. Mech. Eng.*, vol. 285, pp. 166–187, Mar. 2015.
- [107] A. Gholami, A. Mang, and G. Biros, “An inverse problem formulation for parameter estimation of a reaction–diffusion model of low grade gliomas,” *J. Math. Biol.*, vol. 72, no. 1–2, pp. 409–433, Jan. 2016.
- [108] P. E. Barbone and A. A. Oberai, “Elastic modulus imaging: some exact solutions of the compressible elastography inverse problem,” *Phys. Med. Biol.*, vol. 52, no. 6, pp. 1577–1593, Mar. 2007.
- [109] N. H. Gokhale, P. E. Barbone, and A. A. Oberai, “Solution of the nonlinear elasticity imaging inverse problem: the compressible case,” *Inverse Probl.*, vol. 24, no. 4, Jun. 2008. [Online]. Available: <http://stacks.iop.org/0266-5611/24/i=4/a=045010> [Accessed: Jul. 15, 2017].

- [110] S. Goenezen, P. Barbone, and A. A. Oberai, “Solution of the nonlinear elasticity imaging inverse problem: The incompressible case,” *Comput. Methods Appl. Mech. Eng.*, vol. 200, no. 13, pp. 1406–1420, Mar. 2011.
- [111] M. Tyagi, S. Goenezen, P. E. Barbone, and A. A. Oberai, “Algorithms for quantitative quasi-static elasticity imaging using force data,” *Int. J. Numer. Method Biomed. Eng.*, vol. 30, no. 12, pp. 1421–1436, Dec. 2014.
- [112] E. P. Canović, D. T. Seidl, S. R. Polio, A. A. Oberai, P. E. Barbone, D. Stamenović *et al.*, “Biomechanical imaging of cell stiffness and prestress with subcellular resolution,” *Biomech. Model. Mechanobiol.*, vol. 13, no. 3, pp. 665–678, Jun. 2014.
- [113] M. S. Richards, P. E. Barbone, and A. A. Oberai, “Quantitative three-dimensional elasticity imaging from quasi-static deformation: a phantom study,” *Phys. Med. Biol.*, vol. 54, no. 3, pp. 757–779, Feb. 2009.
- [114] T. J Hall, P. E Barboneg, A. A Oberai, J. Jiang, J.-F. Dord, S. Goenezen *et al.*, “Recent results in nonlinear strain and modulus imaging,” *Curr. Med. Imaging Rev.*, vol. 7, no. 4, pp. 313–327, Nov. 2011.
- [115] T. J. Hall, A. A. Oberai, P. E. Barbone, A. M. Sommer, N. H. Gokhale, S. Goenezen *et al.*, “Elastic nonlinearity imaging,” in *Annual International Conference of the IEEE Engineering in Medicine and Biology Society*, Minneapolis, MN, 2009, pp. 1967–1970.
- [116] O. Sahni, J. Müller, K. E. Jansen, M. S. Shephard, and C. A. Taylor, “Efficient anisotropic adaptive discretization of the cardiovascular system,” *Comput. Methods Appl. Mech. Eng.*, vol. 195, no. 41, pp. 5634–5655, Aug. 2006.
- [117] J. Müller, O. Sahni, X. Li, K. Jansen, M. Shephard, and C. Taylor, “Anisotropic adaptive finite element method for modelling blood flow,” *Comput. Methods Biomed. Eng.*, vol. 8, no. 5, pp. 295–305, Oct. 2005.
- [118] R. Teyssier, “Cosmological hydrodynamics with adaptive mesh refinement-a new high resolution code called ramses,” *Astron. Astrophys.*, vol. 385, no. 1, pp. 337–364, Apr. 2002.
- [119] G. Stadler, M. Gurnis, C. Burstedde, L. C. Wilcox, L. Alisic, and O. Ghattas, “The dynamics of plate tectonics and mantle flow: From local to global scales,” *Science*, vol. 329, no. 5995, pp. 1033–1038, Aug. 2010.
- [120] C. Jablonowski, “Adaptive grids in weather and climate modeling,” Ph.D. dissertation, Dept. Clim. Space Sci. Eng., Univ. Michigan, Ann Arbor, MI, 2004.

- [121] F. Zhang, “Parallel adaptive infrastructure for magnetically confined fusion plasma simulations,” Ph.D. dissertation, Dept. Mech. Nucl. Aero. Eng., Rensselaer Polytechnic Inst., Troy, NY, 2015.
- [122] A. Arnold, S. Reichling, O. T. Bruhns, and J. Mosler, “Efficient computation of the elastography inverse problem by combining variational mesh adaption and a clustering technique,” *Phys. Med. Biol.*, vol. 55, no. 7, pp. 2035–2056, Apr. 2010.
- [123] A. Arnold, O. T. Bruhns, and J. Mosler, “An efficient algorithm for the inverse problem in elasticity imaging by means of variational r -adaption,” *Phys. Med. Biol.*, vol. 56, no. 14, pp. 4239–4265, Jul. 2011.
- [124] O. Goksel, H. Eskandari, and S. E. Salcudean, “Mesh adaptation for improving elasticity reconstruction using the FEM inverse problem,” *IEEE Trans. Med. Imaging*, vol. 32, no. 2, pp. 408–418, Feb 2013.
- [125] T. F. Chan and T. P. Mathew, “Domain decomposition algorithms,” *Acta Numerica*, vol. 3, pp. 61143, Jan. 1994.
- [126] E. Van Houten, K. Paulsen, M. Miga, F. Kennedy, and J. Weaver, “An overlapping subzone technique for mr-based elastic property reconstruction,” *Magn. Reson. Med.*, vol. 42, no. 4, pp. 779–786, Oct. 1999.
- [127] A. K. Harris, P. Wild, and D. Stopak, “Silicone rubber substrata: a new wrinkle in the study of cell locomotion,” *Science*, vol. 208, no. 4440, pp. 177–179, Apr. 1980.
- [128] H. P. Ehrlich and J. B. Rajaratnam, “Cell locomotion forces versus cell contraction forces for collagen lattice contraction: an in vitro model of wound contraction,” *Tissue Cell*, vol. 22, no. 4, pp. 407–417, Aug. 1990.
- [129] W. H. Zimmermann, C. Fink, D. Kralisch, U. Remmers, J. Weil, and T. Eschenhagen, “Three-dimensional engineered heart tissue from neonatal rat cardiac myocytes,” *Biotechnol. Bioeng.*, vol. 68, no. 1, pp. 106–114, Apr. 2000.
- [130] H. Vandburgh, J. Shansky, F. Benesch-Lee, V. Barbata, J. Reid, L. Thorrez *et al.*, “Drug-screening platform based on the contractility of tissue-engineered muscle,” *Muscle Nerve*, vol. 37, no. 4, pp. 438–447, Apr. 2008.
- [131] A. Hansen, A. Eder, M. Bönstrup, M. Flato, M. Mewe, S. Schaaf *et al.*, “Development of a drug screening platform based on engineered heart tissue,” *Circ. Res.*, vol. 107, no. 1, pp. 35–44, Jul. 2010.

- [132] T. Boudou, W. R. Legant, A. Mu, M. A. Borochin, N. Thavandiran, M. Radisic *et al.*, “A microfabricated platform to measure and manipulate the mechanics of engineered cardiac microtissues,” *Tissue Eng. Part A*, vol. 18, no. 9–10, pp. 910–919, May. 2011.
- [133] J. L. Tan, J. Tien, D. M. Pirone, D. S. Gray, K. Bhadriraju, and C. S. Chen, “Cells lying on a bed of microneedles: an approach to isolate mechanical force,” *Proc. Natl. Acad. Sci. U.S.A.*, vol. 100, no. 4, pp. 1484–1489, Feb. 2003.
- [134] J. Fu, Y.-K. Wang, M. T. Yang, R. A. Desai, X. Yu, Z. Liu *et al.*, “Mechanical regulation of cell function with geometrically modulated elastomeric substrates,” *Nat. Meth.*, vol. 7, no. 9, pp. 733–736, 2010.
- [135] L. Trichet, J. Le Digabel, R. J. Hawkins, S. R. K. Vedula, M. Gupta, C. Ribrault *et al.*, “Evidence of a large-scale mechanosensing mechanism for cellular adaptation to substrate stiffness,” *Proc. Natl. Acad. Sci. U.S.A.*, vol. 109, no. 18, pp. 6933–6938, May 2012.
- [136] O. Du Roure, A. Saez, A. Buguin, R. H. Austin, P. Chavrier, P. Siberzan *et al.*, “Force mapping in epithelial cell migration,” *Proc. Natl. Acad. Sci. U.S.A.*, vol. 102, no. 7, pp. 2390–2395, Feb. 2005.
- [137] S. Ghassemi, G. Meacci, S. Liu, A. A. Gondarenko, A. Mathur, P. Roca-Cusachs *et al.*, “Cells test substrate rigidity by local contractions on submicrometer pillars,” *Proc. Natl. Acad. Sci. U.S.A.*, vol. 109, no. 14, pp. 5328–5333, Apr. 2012.
- [138] J. Lee, M. Leonard, T. Oliver, A. Ishihara, and K. Jacobson, “Traction forces generated by locomoting keratocytes.” *J. Cell Biol.*, vol. 127, no. 6, pp. 1957–1964, Dec. 1994.
- [139] N. Q. Balaban, U. S. Schwarz, D. Rivelin, P. Goichberg, G. Tzur, I. Sabanay *et al.*, “Force and focal adhesion assembly: a close relationship studied using elastic micropatterned substrates,” *Nat. Cell Biol.*, vol. 3, no. 5, pp. 466–472, May 2001.
- [140] J. P. Butler, I. M. Tolić-Nørrelykke, B. Fabry, and J. J. Fredberg, “Traction fields, moments, and strain energy that cells exert on their surroundings,” *Am. J. Physiol. Cell Physiol.*, vol. 282, no. 3, pp. C595–C605, Mar. 2002.
- [141] N. Wang, I. M. Tolić-Nørrelykke, J. Chen, S. M. Mijailovich, J. P. Butler, J. J. Fredberg *et al.*, “Cell prestress. I. stiffness and prestress are closely associated in adherent contractile cells,” *Am. J. Physiol. Cell Physiol.*, vol. 282, no. 3, pp. C606–C616, Mar. 2002.

- [142] S. A. Maskarinec, C. Franck, D. A. Tirrell, and G. Ravichandran, “Quantifying cellular traction forces in three dimensions,” *Proc. Natl. Acad. Sci. U.S.A.*, vol. 106, no. 52, pp. 22108–22113, Dec. 2009.
- [143] C. Franck, S. A. Maskarinec, D. A. Tirrell, and G. Ravichandran, “Three-dimensional traction force microscopy: a new tool for quantifying cell-matrix interactions,” *PLoS One*, vol. 6, no. 3, Mar. 2011. [Online]. Available: <https://doi.org/10.1371/journal.pone.0017833> [Accessed: Jul. 15, 2017].
- [144] W. R. Legant, J. S. Miller, B. L. Blakely, D. M. Cohen, G. M. Genin, and C. S. Chen, “Measurement of mechanical tractions exerted by cells within three-dimensional matrices,” *Nat. Methods*, vol. 7, no. 12, pp. 969–971, Dec. 2010.
- [145] W. J. Polacheck and C. S. Chen, “Measuring cell-generated forces: a guide to the available tools,” *Nat. Methods*, vol. 13, no. 5, pp. 415–423, Apr. 2016.
- [146] R. W. Style, R. Boltynskiy, G. K. German, C. Hyland, C. W. MacMinn, A. F. Mertz *et al.*, “Traction force microscopy in physics and biology,” *Soft Matter*, vol. 10, no. 23, pp. 4047–4055, Jun. 2014.
- [147] B. Pan, K. Qian, H. Xie, and A. Asundi, “Two-dimensional digital image correlation for in-plane displacement and strain measurement: a review,” *Meas. Sci. Technol.*, vol. 20, no. 6, Apr. 2009. [Online]. Available: <http://stacks.iop.org/0957-0233/20/i=6/a=062001> [Accessed: Jul. 15, 2017].
- [148] C. Franck, S. Hong, S. Maskarinec, D. Tirrell, and G. Ravichandran, “Three-dimensional full-field measurements of large deformations in soft materials using confocal microscopy and digital volume correlation,” *Exp. Mech.*, vol. 47, no. 3, pp. 427–438, Jun. 2007.
- [149] B. Bay, “Methods and applications of digital volume correlation,” *J. Strain Anal. Eng. Des.*, vol. 43, no. 8, pp. 745–760, Aug. 2008.
- [150] W. R. Legant, C. K. Choi, J. S. Miller, L. Shao, L. Gao, E. Betzig *et al.*, “Multidimensional traction force microscopy reveals out-of-plane rotational moments about focal adhesions,” *Proc. Natl. Acad. Sci. U.S.A.*, vol. 110, no. 3, pp. 881–886, Jan. 2013.
- [151] S. S. Hur, Y. Zhao, Y.-S. Li, E. Botvinick, and S. Chien, “Live cells exert 3-dimensional traction forces on their substrata,” *Cell. Mol. Bioeng.*, vol. 2, no. 3, pp. 425–436, Sep. 2009.
- [152] H. Delanoë-Ayari, J. Rieu, and M. Sano, “4D traction force microscopy reveals asymmetric cortical forces in migrating dictyostelium cells,” *Phys. Rev. Lett.*, vol. 105, no. 24, Dec. 2010. [Online]. Available: <https://doi.org/10.1103/PhysRevLett.105.248103> [Accessed: Jul. 15, 2017].

- [153] T. M. Koch, S. Münster, N. Bonakdar, J. P. Butler, and B. Fabry, “3D traction forces in cancer cell invasion,” *PLoS One*, vol. 7, no. 3. Mar. 2012. [Online]. Available: <https://doi.org/10.1371/journal.pone.0033476> [Accessed: Jul. 15, 2017].
- [154] N. Gjorevski and C. M. Nelson, “Mapping of mechanical strains and stresses around quiescent engineered three-dimensional epithelial tissues,” *Biophys. J.*, vol. 103, no. 1, pp. 152–162, Jul. 2012.
- [155] J. Toyjanova, E. Bar-Kochba, C. López-Fagundo, J. Reichner, D. Hoffman-Kim, and C. Franck, “High resolution, large deformation 3D traction force microscopy,” *PLoS One*, vol. 9, no. 4, Apr. 2014. [Online]. Available: <https://doi.org/10.1371/journal.pone.0090976> [Accessed: Jul. 15, 2017].
- [156] R. H. Byrd, P. Lu, J. Nocedal, and C. Zhu, “A limited memory algorithm for bound constrained optimization,” *SIAM J. Sci. Comput.*, vol. 16, no. 5, pp. 1190–1208, Sept. 1995.
- [157] U. S. Schwarz, N. Q. Balaban, D. Riveline, A. Bershadsky, B. Geiger, and S. Safran, “Calculation of forces at focal adhesions from elastic substrate data: the effect of localized force and the need for regularization,” *Biophys. J.*, vol. 83, no. 3, pp. 1380–1394, Sept. 2002.
- [158] L. D. Landau, A. Kosevich, L. P. Pitaevskii, and E. M. Lifshitz, *Theory of Elasticity*, 3rd ed. Oxford, UK: Butterworth, 2012.
- [159] T. Boudou, J. Ohayon, C. Picart, R. I. Pettigrew, and P. Tracqui, “Nonlinear elastic properties of polyacrylamide gels: implications for quantification of cellular forces,” *Biorheology*, vol. 46, no. 3, pp. 191–205, Jun. 2009.
- [160] J. W. Stone, P. N. Sisco, E. C. Goldsmith, S. C. Baxter, and C. J. Murphy, “Using gold nanorods to probe cell-induced collagen deformation,” *Nano Lett.*, vol. 7, no. 1, pp. 116–119, Jan. 2007.
- [161] D. Discher, C. Dong, J. J. Fredberg, F. Guilak, D. Ingber, P. Janmey *et al.*, “Biomechanics: cell research and applications for the next decade,” *Ann. Biomed. Eng.*, vol. 37, no. 5, pp. 847–859, May 2009.
- [162] G. Y. Lee and C. T. Lim, “Biomechanics approaches to studying human diseases,” *Trends Biotechnol.*, vol. 25, no. 3, pp. 111–118, Mar. 2007.
- [163] P. A. Janmey and C. A. McCulloch, “Cell mechanics: integrating cell responses to mechanical stimuli,” *Annu. Rev. Biomed. Eng.*, vol. 9, pp. 1–34, Aug. 2007.

- [164] R. G. Wells, “The role of matrix stiffness in hepatic stellate cell activation and liver fibrosis,” *Clin. Gastroenterol. Hepatol.*, vol. 39, no. 4, pp. S158–S161, Apr. 2005.
- [165] P. Friedl and S. Alexander, “Cancer invasion and the microenvironment: plasticity and reciprocity,” *Cell*, vol. 147, no. 5, pp. 992–1009, Nov. 2011.
- [166] C. T. Mierke, “Endothelial cell’s biomechanical properties are regulated by invasive cancer cells,” *Mol. Biosyst.*, vol. 8, no. 6, pp. 1639–1649, Apr. 2012.
- [167] P. Wellman, R. D. Howe, E. Dalton, and K. A. Kern, “Breast tissue stiffness in compression is correlated to histological diagnosis,” 1999. [Online]. Available: <https://biorobotics.harvard.edu/pubs/1999/mechprops.pdf> [Accessed: Jun. 15, 2017].
- [168] T. Liu, O. A. Babaniyi, T. J. Hall, P. E. Barbone, and A. A. Oberai, “Noninvasive in-vivo quantification of mechanical heterogeneity of invasive breast carcinomas,” *PLoS One*, vol. 10, no. 7, Jul. 2015. [Online]. Available: <https://doi.org/10.1371/journal.pone.0130258> [Accessed: Jul. 15, 2017].
- [169] D. Ingber, “Mechanobiology and diseases of mechanotransduction,” *Ann. Med.*, vol. 35, no. 8, pp. 564–577, Jan. 2003.
- [170] K. J. Parker, M. M. Doyley, and D. J. Rubens, “Imaging the elastic properties of tissue: the 20 year perspective,” *Phys. Med. Biol.*, vol. 56, no. 1, pp. R1–R29, Jan. 2011.
- [171] J. F. Greenleaf, M. Fatemi, and M. Insana, “Selected methods for imaging elastic properties of biological tissues,” *Annu. Rev. Biomed. Eng.*, vol. 5, no. 1, pp. 57–78, Apr. 2003.
- [172] J. Braun, J. Guo, R. Lützkendorf, J. Stadler, S. Papazoglou, S. Hirsch *et al.*, “High-resolution mechanical imaging of the human brain by three-dimensional multifrequency magnetic resonance elastography at 7T,” *Neuroimage*, vol. 90, pp. 308–314, Apr. 2014.
- [173] L. Sandrin, B. Fourquet, J.-M. Hasquenoph, S. Yon, C. Fournier, F. Mal *et al.*, “Transient elastography: a new noninvasive method for assessment of hepatic fibrosis,” *Ultrasound Med. Biol.*, vol. 29, no. 12, pp. 1705–1713, Dec. 2003.
- [174] S. Wang and K. V. Larin, “Optical coherence elastography for tissue characterization: a review,” *J. Biophotonics*, vol. 8, no. 4, pp. 279–302, Apr. 2015.
- [175] B. F. Kennedy, R. A. McLaughlin, K. M. Kennedy, L. Chin, P. Wijesinghe, A. Curatolo *et al.*, “Investigation of optical coherence microelastography as a

- method to visualize cancers in human breast tissue,” *Cancer Res.*, vol. 75, no. 16, pp. 3236–3245, Aug. 2015.
- [176] S. Wang and K. V. Larin, “Shear wave imaging optical coherence tomography (SWI-OCT) for ocular tissue biomechanics,” *Opt. Lett.*, vol. 39, no. 1, pp. 41–44, Jan. 2014.
- [177] W. Qi, R. Li, T. Ma, J. Li, K. K. Shung, Q. Zhou *et al.*, “Resonant acoustic radiation force optical coherence elastography,” *Appl. Phys. Lett.*, vol. 103, no. 10, Sep. 2013. [Online]. Available: <http://dx.doi.org/10.1063/1.4820252> [Accessed: Jul. 15, 2017].
- [178] G. van Soest, F. Mastik, N. de Jong, and A. F. van der Steen, “Robust intravascular optical coherence elastography by line correlations,” *Phys. Med. Biol.*, vol. 52, no. 9, pp. 2445–2458, May 2007.
- [179] A. H. Chau, R. C. Chan, M. Shishkov, B. MacNeill, N. Iftimia, G. J. Tearney *et al.*, “Mechanical analysis of atherosclerotic plaques based on optical coherence tomography,” *Ann. Biomed. Eng.*, vol. 32, no. 11, pp. 1494–1503, Nov. 2004.
- [180] A. Nahas, M. Bauer, S. Roux, and A. C. Boccara, “3D static elastography at the micrometer scale using full field OCT,” *Biomed. Opt. Express*, vol. 4, no. 10, pp. 2138–2149, Sep. 2013.
- [181] C. Li, G. Guan, X. Cheng, Z. Huang, and R. K. Wang, “Quantitative elastography provided by surface acoustic waves measured by phase-sensitive optical coherence tomography,” *Opt. Lett.*, vol. 37, no. 4, pp. 722–724, Feb. 2012.
- [182] R. K. Manapuram, S. Aglyamov, F. Menodiado, M. Mashiatulla, S. Wang, S. Baranov *et al.*, “Estimation of shear wave velocity in gelatin phantoms utilizing phs-ssoct,” *Laser Phys.*, vol. 22, no. 9, pp. 1439–1444, Sep. 2012.
- [183] P. Wijesinghe, R. A. McLaughlin, D. D. Sampson, and B. F. Kennedy, “Parametric imaging of viscoelasticity using optical coherence elastography,” *Phys. Med. Biol.*, vol. 60, no. 6, pp. 2293–2307, Mar. 2015.
- [184] V. Crecea, A. Ahmad, and S. A. Boppart, “Magnetomotive optical coherence elastography for microrheology of biological tissues,” *J. Biomed. Opt.*, vol. 18, no. 12, Dec. 2013. [Online]. Available: <http://dx.doi.org/10.1117/1.JBO.18.12.121504> [Accessed: Jul. 20, 2017].
- [185] S. G. Adie, X. Liang, B. F. Kennedy, R. John, D. D. Sampson, and S. A. Boppart, “Spectroscopic optical coherence elastography,” *Opt. Express*, vol. 18, no. 25, pp. 25519–25534, Dec. 2010.

- [186] A. S. Khalil, B. E. Bouma, and M. R. K. Mofrad, “A combined fem/genetic algorithm for vascular soft tissue elasticity estimation,” *Cardiovasc. Eng.*, vol. 6, no. 3, pp. 93–102, Sep. 2006.
- [187] A. S. Khalil, R. C. Chan, A. H. Chau, B. E. Bouma, and M. R. K. Mofrad, “Tissue elasticity estimation with optical coherence elastography: Toward mechanical characterization of in vivo soft tissue,” *Ann. Biomed. Eng.*, vol. 33, no. 11, pp. 1631–1639, Nov. 2005.
- [188] F. A. Duck, *Physical Properties of Tissues: A Comprehensive Reference Book*. Cambridge, MA, USA: Academic Press, 1990.
- [189] Y.-C. Fung, *Biomechanics: Mechanical Properties of Living Tissues*, 2nd ed. New York, NY, USA: Springer, 1993.
- [190] F. Kallel, J. Ophir, K. Magee, and T. Krouskop, “Elastographic imaging of low-contrast elastic modulus distributions in tissue,” *Ultrasound Med. Biol.*, vol. 24, no. 3, pp. 409–425, Mar. 1998.
- [191] K. D. Mohan and A. L. Oldenburg, “Elastography of soft materials and tissues by holographic imaging of surface acoustic waves,” *Opt. Express*, vol. 20, no. 17, pp. 18887–18897, Aug. 2012.
- [192] M. Razani, A. Mariampillai, C. Sun, T. W. Luk, V. X. Yang, and M. C. Kolios, “Feasibility of optical coherence elastography measurements of shear wave propagation in homogeneous tissue equivalent phantoms,” *Biomed. Opt. Express*, vol. 3, no. 5, pp. 972–980, May 2012.
- [193] V. Crecea, A. L. Oldenburg, X. Liang, T. S. Ralston, and S. A. Boppart, “Magnetomotive nanoparticle transducers for optical rheology of viscoelastic materials,” *Opt. Express*, vol. 17, no. 25, pp. 23114–23122, Dec. 2009.
- [194] A. L. Oldenburg and S. A. Boppart, “Resonant acoustic spectroscopy of soft tissues using embedded magnetomotive nanotransducers and optical coherence tomography,” *Phys. Med. Biol.*, vol. 55, no. 4, pp. 1189–1201, Feb. 2010.
- [195] S. Chikayoshi, A. Suzuki, and K. Nakayama, “Phantom experiment on estimation of shear modulus distribution in soft tissue from ultrasonic measurement of displacement vector field,” *IEICE Trans. Fund. Electr.*, vol. 78, no. 12, pp. 1655–1664, Dec. 1995.
- [196] U. Albocher, A. A. Oberai, P. E. Barbone, and I. Harari, “Adjoint-weighted equation for inverse problems of incompressible plane-stress elasticity,” *Comput. Methods Appl. Mech. Eng.*, vol. 198, no. 30, pp. 2412–2420, Jun. 2009.

- [197] M. Burger, B. Kaltenbacher, and A. Neubauer, “Iterative solution methods,” in *Handbook of Mathematical Methods in Imaging*, O. Scherzer, Ed. New York, NY: Springer, 2011.
- [198] F. Kallel and M. Bertrand, “Tissue elasticity reconstruction using linear perturbation method,” *IEEE Trans. Med. Imaging*, vol. 15, no. 3, pp. 299–313, Jun. 1996.
- [199] R. K. Wang, S. Kirkpatrick, and M. Hinds, “Phase-sensitive optical coherence elastography for mapping tissue microstrains in real time,” *Appl. Phys. Lett.*, vol. 90, no. 16, Apr. 2007. [Online]. Available: <http://dx.doi.org/10.1063/1.2724920> [Accessed: Jul. 15, 2017].
- [200] P. E. Barbone and J. C. Bamber, “Quantitative elasticity imaging: What can and cannot be inferred from strain images,” *Phys. Med. Biol.*, vol. 47, no. 12, pp. 2147–2164, Jun. 2002.
- [201] P. E. Barbone and N. H. Gokhale, “Elastic modulus imaging: On the uniqueness and nonuniqueness of the elastography inverse problem in two dimensions,” *Inverse Probl.*, vol. 20, no. 1, pp. 283–296, Jan. 2004.
- [202] U. Albocher, P. E. Barbone, A. A. Oberai, and I. Harari, “Uniqueness of inverse problems of isotropic incompressible three-dimensional elasticity,” *J. Mech. Phys. Solids*, vol. 73, pp. 55–68, Dec. 2014.
- [203] L. I. Rudin, S. Osher, and E. Fatemi, “Nonlinear total variation based noise removal algorithms,” *Physica D*, vol. 60, no. 1–4, pp. 259–268, Nov. 1992.
- [204] C. Zhu, R. H. Byrd, P. Lu, and J. Nocedal, “Algorithm 778: L-BFGS-B: Fortran subroutines for large-scale bound-constrained optimization,” *ACM Trans. Math. Softw.*, vol. 23, no. 4, pp. 550–560, Dec. 1997.
- [205] G. Lamouche, B. F. Kennedy, K. M. Kennedy, C.-E. Bisailon, A. Curatolo, G. Campbell *et al.*, “Review of tissue simulating phantoms with controllable optical, mechanical and structural properties for use in optical coherence tomography,” *Biomed. Opt. Express*, vol. 3, no. 6, pp. 1381–1398, Jun. 2012.
- [206] L. Chin, A. Curatolo, B. F. Kennedy, B. J. Doyle, P. R. Munro, R. A. McLaughlin *et al.*, “Analysis of image formation in optical coherence elastography using a multiphysics approach,” *Biomed. Opt. Express*, vol. 5, no. 9, pp. 2913–2930, Sep. 2014.
- [207] A. Tarantola, *Inverse Problem Theory and Methods for Model Parameter Estimation*. Philadelphia, PA, USA: SIAM, 2005.
- [208] R. A. McLaughlin, P. B. Noble, and D. D. Sampson, “Optical coherence tomography in respiratory science and medicine: From airways to alveoli,” *Physiology*, vol. 29, no. 5, pp. 369–380, Sep. 2014.

- [209] V. A. Morozov, “Regularization of incorrectly posed problems and the choice of regularization parameter,” *USSR Comput. Math. Math. Phys.*, vol. 6, no. 1, pp. 242–251, Jan. 1966.
- [210] J. M. Schmitt, “OCT elastography: Imaging microscopic deformation and strain of tissue,” *Opt. Express*, vol. 3, no. 6, pp. 199–211, Sep. 1998.
- [211] J. Fu, F. Pierron, and P. D. Ruiz, “Elastic stiffness characterization using three-dimensional full-field deformation obtained with optical coherence tomography and digital volume correlation,” *J. Biomed. Opt.*, vol. 18, no. 12, Dec. 2013. [Online]. Available: <http://dx.doi.org/10.1117/1.JBO.18.121512> [Accessed: Jul. 20, 2017].
- [212] J. T. Iivarinen, R. K. Korhonen, P. Julkunen, and J. S. Jurvelin, “Experimental and computational analysis of soft tissue stiffness in forearm using a manual indentation device,” *Med. Eng. Phys.*, vol. 33, no. 10, pp. 1245–1253, Dec. 2011.
- [213] J. Clark, J. Cheng, and K. Leung, “Mechanical properties of normal skin and hypertrophic scars,” *Burns*, vol. 22, no. 6, pp. 443–446, Sep. 1996.
- [214] B. Kali, J. de Rigal, F. Léonard, J. Lévêque, O. Riche, Y. Le Corre *et al.*, “In vivo study of scleroderma by non-invasive techniques,” *Br. J. Dermatol.*, vol. 122, no. 6, pp. 785–791, Jun. 1990.
- [215] C. Escoffier, J. de Rigal, A. Rochefort, R. Vasselet, J.-L. Lévêque, and P. G. Agache, “Age-related mechanical properties of human skin: An in vivo study,” *J. Invest. Dermatol.*, vol. 93, no. 3, pp. 353–357, Sep. 1989.
- [216] S. Es'haghian, K. M. Kennedy, P. Gong, Q. Li, L. Chin, P. Wijesinghe *et al.*, “In vivo volumetric quantitative micro-elastography of human skin,” *Biomed. Opt. Express*, vol. 8, no. 5, pp. 2458–2471, May 2017.
- [217] A. J. Engler, S. Sen, H. L. Sweeney, and D. E. Discher, “Matrix elasticity directs stem cell lineage specification,” *Cell*, vol. 126, no. 4, pp. 677–689, Aug. 2006.
- [218] P. Friedl and K. Wolf, “Tumour-cell invasion and migration: Diversity and escape mechanisms,” *Nat. Rev. Cancer*, vol. 3, no. 5, pp. 362–374, May 2003.
- [219] D. A. Lauffenburger and A. F. Horwitz, “Cell migration: A physically integrated molecular process,” *Cell*, vol. 84, no. 3, pp. 359–369, Feb. 1996.
- [220] C. G. Galbraith and M. P. Sheetz, “A micromachined device provides a new bend on fibroblast traction forces,” *Proc. Natl. Acad. Sci. U.S.A.*, vol. 94, no. 17, pp. 9114–9118, Aug. 1997.

- [221] M. Dembo and Y.-L. Wang, “Stresses at the cell-to-substrate interface during locomotion of fibroblasts,” *Biophys. J.*, vol. 76, no. 4, pp. 2307–2316, Apr. 1999.
- [222] Z. Yang, J.-S. Lin, J. Chen, and J. H. Wang, “Determining substrate displacement and cell traction fields a new approach,” *J. Theor. Biol.*, vol. 242, no. 3, pp. 607–616, Oct. 2006.
- [223] G. Vitale, L. Preziosi, and D. Ambrosi, “A numerical method for the inverse problem of cell traction in 3D,” *Inverse Probl.*, vol. 28, no. 9, Aug. 2012. [Online]. Available: <http://stacks.iop.org/0266-5611/28/i=9/a=095013> [Accessed: Jul. 15, 2017].
- [224] M. E. Gurtin, *An Introduction to Continuum Mechanics*. Cambridge, MA, USA: Academic Press, 1982.
- [225] M. E. Gurtin, E. Fried, and L. Anand, *The Mechanics and Thermodynamics of Continua*. Cambridge, UK: Cambridge University Press, 2010.
- [226] Y.-C. Fung, *A First Course in Continuum Mechanics*, 3rd ed. London, UK: Pearson, 1993.
- [227] T. Z. Pavan, E. L. Madsen, G. R. Frank, A. A. O. Carneiro, and T. J. Hall, “Nonlinear elastic behavior of phantom materials for elastography,” *Phys. Med. Biol.*, vol. 55, no. 9, pp. 2679–2792, May 2010.
- [228] C. Storm, J. J. Pastore, F. C. MacKintosh, T. C. Lubensky, and P. A. Janmey, “Nonlinear elasticity in biological gels,” *Nature*, vol. 435, no. 7039, pp. 191–194, May 2005.
- [229] J. Palacio, A. Jorge-Peñas, A. Muñoz-Barrutia, C. Ortiz-de Solorzano, E. de Juan-Pardo, and J. M. García-Aznar, “Numerical estimation of 3D mechanical forces exerted by cells on non-linear materials,” *J. Biomech.*, vol. 46, no. 1, pp. 50–55, Jan. 2013.
- [230] M. S. Hall, R. Long, X. Feng, Y. Huang, C.-Y. Hui, and M. Wu, “Toward single cell traction microscopy within 3D collagen matrices,” *Exp. Cell Res.*, vol. 319, no. 16, pp. 2396–2408, Oct. 2013.
- [231] S. S. Ng, C. Li, and V. Chan, “Experimental and numerical determination of cellular traction force on polymeric hydrogels,” *Interface Focus*, vol. 1, no. 5, pp. 777–791, Oct. 2011.
- [232] T. J. Hall, P. Barbone, A. A. Oberai, J. Jiang, J. F. Dord, S. Goenezen *et al.*, “Recent results in nonlinear strain and modulus imaging,” *Curr. Med. Imaging Rev.*, vol. 7, no. 4, pp. 313–327, Nov. 2011.

- [233] M. Gockenbach, B. Jadamba, and A. Khan, “Equation error approach for elliptic inverse problems with an application to the identification of lamé parameters,” *Inverse Probl. Sci. Eng.*, vol. 16, no. 3, pp. 349–367, Apr. 2008.
- [234] D. Schnur and N. Zabaras, “Finite element solution of two-dimensional inverse elastic problems using spatial smoothing,” *Int. J. Numer. Meth. Eng.*, vol. 30, no. 1, pp. 57–75, Jul. 1990.
- [235] L. M. Bezerra and S. Saigal, “Inverse boundary traction reconstruction with the BEM,” *Int. J. Solids Struct.*, vol. 32, no. 10, pp. 1417–1431, May 1995.
- [236] K. Kamiyama, K. Vlack, T. Mizota, H. Kajimoto, N. Kawakami, and S. Tachi, “Vision-based sensor for real-time measuring of surface traction fields,” *IEEE Comput. Graph. Appl.*, vol. 25, no. 1, pp. 68–75, Jan. 2005.
- [237] P. J. Blatz, B. M. Chu, and H. Wayland, “On the mechanical behavior of elastic animal tissue,” *Trans. Soc. Rheol.*, vol. 13, no. 1, pp. 83–102, Mar. 1969.
- [238] D. Veronda and R. Westmann, “Mechanical characterization of skinfinite deformations,” *J. Biomech.*, vol. 3, no. 1, pp. 111–124, Jan. 1970.
- [239] Y.-C. Fung, “Elasticity of soft tissues in simple elongation,” *Am. J. Physiol.*, vol. 213, no. 6, pp. 1532–1544, Dec. 1967.
- [240] O. Klaas, A. Maniatty, and M. S. Shephard, “A stabilized mixed finite element method for finite elasticity: Formulation for linear displacement and pressure interpolation,” *Comput. Methods Appl. Mech. Eng.*, vol. 180, no. 1–2, pp. 65–79, Nov. 1999.
- [241] A. M. Maniatty, Y. Liu, O. Klaas, and M. S. Shephard, “Higher order stabilized finite element method for hyperelastic finite deformation,” *Comput. Methods Appl. Mech. Eng.*, vol. 191, no. 13–14, pp. 1491–1503, Jan. 2002.
- [242] D. A. Tortorelli, “Sensitivity analysis for non-linear constrained elastostatic systems,” *Int. J. Numer. Meth. Eng.*, vol. 33, no. 8, pp. 1643–1660, Jun. 1992.
- [243] A. Sei and W. W. Symes, “Gradient calculation of the traveltime cost function without ray tracing,” in *65th Annual International Meeting of Society of Exploration Geophysicists*, Houston, TX, 1994, pp. 1351–1354.
- [244] O. Dorn, H. Bertete-Aguirre, J. Berryman, and G. Papanicolaou, “A nonlinear inversion method for 3D electromagnetic imaging using adjoint fields,” *Inverse Probl.*, vol. 15, no. 6, pp. 1523–1558, Dec. 1999.

- [245] G. R. Feij  o, A. A. Oberai, and P. M. Pinsky, “An application of shape optimization in the solution of inverse acoustic scattering problems,” *Inverse Probl.*, vol. 20, no. 1, pp. 199–228, Feb. 2004.
- [246] A. N. Tikhonov, V. I. Arsenin, and F. John, *Solutions of Ill-posed Problems*. Washington, D.C., USA: Winston, 1977.
- [247] C. R. Vogel, *Computational Methods for Inverse Problems*. Philadelphia, PA, USA: SIAM, 2002.
- [248] P. C. Hansen, “Analysis of discrete ill-posed problems by means of the L-curve,” *SIAM Rev.*, vol. 34, no. 4, pp. 561–580, Oct. 1992.
- [249] C. A. Schneider, W. S. Rasband, and K. W. Eliceiri, “NIH image to ImageJ: 25 years of image analysis,” *Nat. Methods*, vol. 9, no. 7, pp. 671–675, Jul. 2012.
- [250] J. H. Wang and J.-S. Lin, “Cell traction force and measurement methods,” *Biomech. Model. Mechanobiol.*, vol. 6, no. 6, pp. 361–371, Nov. 2007.
- [251] M. J. Paszek, N. Zahir, K. R. Johnson, J. N. Lakins, G. I. Rozenberg, A. Gefen *et al.*, “Tensional homeostasis and the malignant phenotype,” *Cancer Cell*, vol. 8, no. 3, pp. 241–254, Sep. 2005.
- [252] D. E. Discher, P. Janmey, and Y.-L. Wang, “Tissue cells feel and respond to the stiffness of their substrate,” *Science*, vol. 310, no. 5751, pp. 1139–1143, Nov. 2005.
- [253] P. C. Kerstein, I. Nichol, H. Robert, and T. M. Gomez, “Mechanochemical regulation of growth cone motility,” *Front. Cell. Neurosci.*, vol. 9, Jul. 2015. [Online]. Available: <https://doi.org/10.3389/fncel.2015.00244> [Accessed: Jul. 15, 2017].
- [254] J. Jiang, Z.-H. Zhang, X.-B. Yuan, and M.-M. Poo, “Spatiotemporal dynamics of traction forces show three contraction centers in migratory neurons,” *J. Cell Biol.*, vol. 209, no. 5, pp. 759–774, Jun. 2015.
- [255] Q. Fang and D. A. Boas, “Tetrahedral mesh generation from volumetric binary and grayscale images,” in *2009 IEEE International Symposium on Biomedical Imaging: From Nano to Macro*, Boston, MA, 2009, pp. 1142–1145.
- [256] J. Donea, A. Huerta, J.-P. Ponthot, and A. Rodr  guez-Ferran, “Arbitrary Lagrangian-Eulerian methods,” in *Encyclopedia of Computational Mechanics*, E. Stein, R. D. Borst, and T. J. R. Hughes, Eds. Hoboken, NJ, USA: Wiley, 2004, vol. 1, ch. 14, pp. 413–437.

- [257] N.-S. Lee and K.-J. Bathe, “Error indicators and adaptive remeshing in large deformation finite element analysis,” *Finite Elem. Anal. Des.*, vol. 16, no. 2, pp. 99–139, May 1994.
- [258] S. Govindjee and P. A. Mihalic, “Computational methods for inverse finite elastostatics,” *Comput. Methods Appl. Mech. Eng.*, vol. 136, no. 1–2, pp. 47–57, Sep. 1996.
- [259] S. Govindjee and P. A. Mihalic, “Computational methods for inverse deformations in quasi-incompressible finite elasticity,” *Int. J. Numer. Meth. Eng.*, vol. 43, no. 5, pp. 821–838, Nov. 1998.
- [260] L. Zhang, S. P. Lake, V. H. Barocas, M. S. Shephard, and R. C. Picu, “Cross-linked fiber network embedded in an elastic matrix,” *Soft Matter*, vol. 9, no. 28, pp. 6398–6405, Jul. 2013.
- [261] D. T. Seidl, “A computational framework for elliptic inverse problems with uncertain boundary conditions,” Ph.D. dissertation, Dept. Mech. Eng., Boston Univ., Boston, MA, 2015.
- [262] A. Logg, K.-A. Mardal, and G. Wells, *Automated Solution of Differential Equations by the Finite Element Method: The FEniCS book*. New York, NY, USA: Springer, 2012.